Terahertz-Induced Dynamics in Strongly Correlated and Magnetic Materials

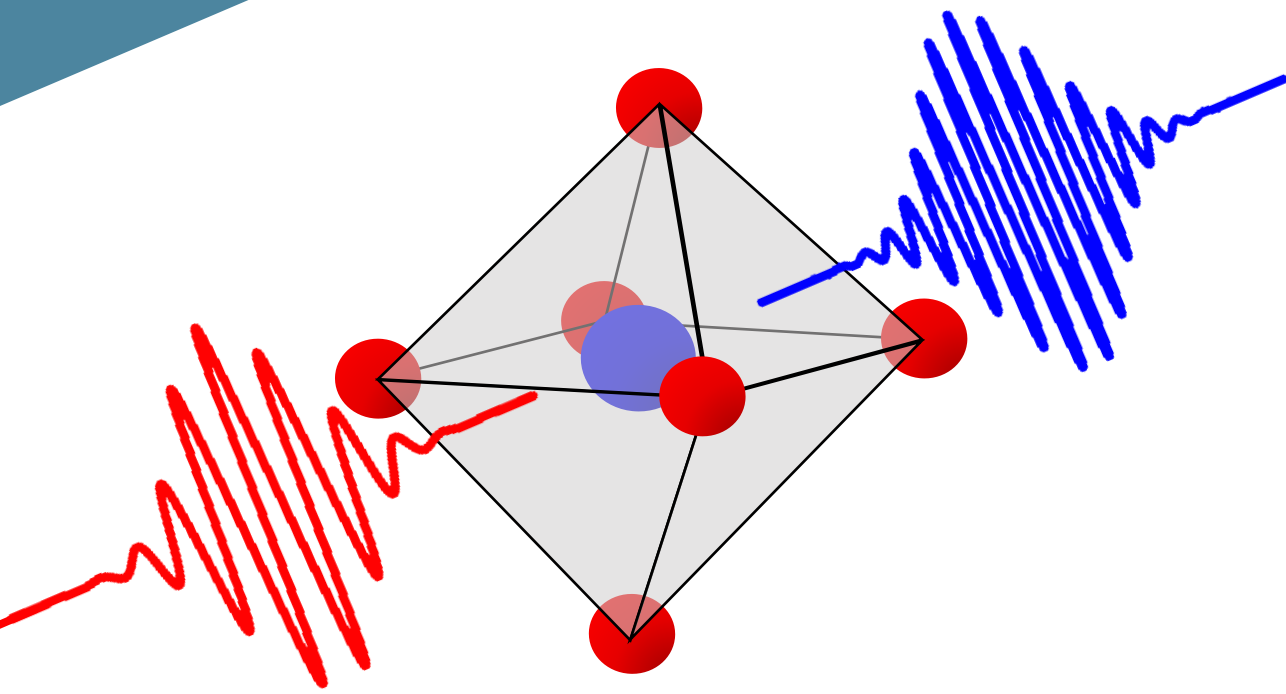

2024

Chris Reinhoffer

UNIVERSITÄT ZU KÖLN

Terahertz-Induced Dynamics in Strongly Correlated and Magnetic Materials

Inaugural-Dissertation
zur
Erlangung des Doktorgrades
der Mathematisch-Naturwissenschaftlichen Fakultät
der Universität zu Köln

vorgelegt von
Chris Niels Reinhoffer
geboren in Goch, Deutschland

Köln
Juni 2024

Gutachter:	Prof. Dr. Ir. P.H.M. van Loosdrecht
Gutachter:	Prof. Dr. S. Johnson
Vorsitzender der Prüfungskommission:	Prof. Dr. S. Trebst
Tag der Mündlichen Prüfung:	13. September 2024

"In physics, you don't have to go around making trouble for yourself - nature does it for you."

Frank Wilczek

Contents

Introduction

Research interest in the terahertz (THz) frequency range surged in the second half of the 20th century, driven by its potential to investigate new material properties. With the invention of oxygen and nitrogen liquifiers in 1883 and helium liquifiers in 1908, scientists were able to explore low-temperature and low-energy phenomena. THz spectroscopy, with its inherent sensitivity to the meV energy range ($1\ \text{THz} \mathrel{\hat{=}} 4.1\ \text{meV}$), is uniquely positioned to explore low energy phenomena. This sensitivity allows for the study of phenomena such as the binding energy of Cooper pairs, magnetic excitations, charge density waves, or more general low energy electron dynamics in strongly correlated materials. Achieving THz frequencies is inherently difficult: microwave generation is limited to under 100 GHz, and optical infrared spectroscopy struggles with frequencies below 10 THz, resulting in the so called THz-gap. Before the advent of modern THz generators, researchers used backward-wave oscillators to reach frequencies from a few GHz up to 1 THz [1–3]. Although effective for studies like measuring the magnetic excitations in rare-earth orthoferrites [3], these early methods were surpassed by more advanced techniques developed later, following the development of ultrafast laser sources in 1966 [4, 5].

In 1988 and 1989 Ch. Fattinger and D. Grischkowsky demonstrated the possibility of generating and detecting freely propagating THz pulses on subpicosecond timescales [6, 7] based on observations made by Auston et al. in 1984 [8]. The power of this approach was demonstrated a year later with the broadband, i.e., 0.1 to 2 THz, investigation of doped silicon [9]. Further development improved the accessible frequency range up to 4 THz [10], enabling the investigation of low energy phenomena laying in the energy range

between 0.4 and 16 meV. However, this approach was limited in the time resolution and detector response function. These problems were addressed by Q. Wu and X.-C. Zhang in 1995 were they demonstrated free-space electro-optic sampling of THz beams using crystals instead of antennas [11].

The development of freely propagating THz pulses on subpicosecond timescales opened the possibility for a usecase in ultrafast optics applications. One of the first results was an optical pump THz-probe study of silicon performed by Jürgen Zielbauer and Martin Wegener [12]. With the investigation of various phenomena using THz pulses as a probe, there was growing interest in using THz pulses as a pump to potentially achieve coherent control of many of these low-energy phenomena. For tabletop experiments this advancement came in 2002 when Hebling et al. developed the by now well known tilted-wave-front optical rectification technique [13]. With this new method, THz pulses with peak electric fields up to $1\,\mathrm{MV\,cm^{-1}}$ [14] became usable in pump probe experiments to access and drive low energy excitations directly, paving the way for new experimental approaches.

Recently, the field of ultrafast THz spectroscopy expanded to the investigation of THz driven nonlinear phenomena [15–18]. The high field strength achievable nowadays can drive systems so far out of equilibrium that the first order perturbation description is not accurate anymore. By using harmonic generation scientists were able to investigate the Higgs mode in superconductors [15, 16] and the charge carrier dynamics in Dirac matter [17]. By using 2D THz pump spectroscopy it was possible to investigate the nonlinear energy flow between lattice and magnetic subsystems [18].

These advancements in ultrafast THz spectroscopy will be used in this thesis to investigate quantum phenomena at low temperatures. A particular focus is on the THz harmonic generation in the strongly correlated transition metal oxide (Sr,Ca)RuO_3 and the BCS superconductor MgB_2. Furthermore, the magnetization dynamics under strong THz drive in the ferrimagnet $(Gd,Bi)_3Fe_5O_{12}$ are studied.

(Sr,Ca)RuO_3 (Chapter 2) is a strongly correlated metal in where the structural, electronic and magnetic properties all depend on each other. While

$SrRuO_3$ is a ferromagnetic Fermi-liquid, whereas $CaRuO_3$ lacks a confirmed magnetically ordered ground state and shows non-Fermi-liquid behavior. This indicates a quantum phase transition taking place between $SrRuO_3$ and $CaRuO_3$ [19–21]. The main driving mechanism behind the phase transition is the stronger octahedral distortion in $CaRuO_3$, which results in increased electronic correlation and suppresses the magnetic order [22]. Despite extensive efforts, the low-temperature optical conducting properties are still not fully understood. The first far-infrared spectroscopic measurements were performed in 1998 [23], and as recently as 2021 [24], there are still works offering different interpretations to understand the optical response. This thesis extends these investigations to the nonlinear response of (Sr,Ca)RuO_3 in the THz frequency range, aiming to reveal the microscopic origin of the low-temperature optical conducting properties.

MgB_2 (Chapter 3) is the BCS type superconductor with the highest known transition temperature at ambient conditions, which is 39 K [25]. The collective ground state that forms in a superconducting condensate has two fundamental excitations. These excitations are a change in amplitude, commonly referred to as the Higgs mode, and a change in phase, commonly referred to as the Nambu-Goldstone mode [16]. The Higgs mode lacks electric charge, magnetic moment, and other quantum numbers, making it inaccessible to linear probes [16]. However, in recent years THz harmonic generation spectroscopy has been established as a good probe of the nonlinear properties of superconductors [15, 16, 26, 27]. By changing the temperature of the superconductor, the frequency of the Higgs mode can be tuned to be in resonance with the THz excitation frequency, leading to a strong increase in THz third harmonic generation [15, 16]. In this thesis, third harmonic generation is used to investigate the nonlinear response of MgB_2 in an external magnetic field.

$(Gd,Bi)_3Fe_5O_{12}$ (Chapter 4) is an insulating ferrimagnet with magnetic properties determined by the interactions among three individual sublattices. There are two iron sublattices that strongly interact and align antiferromagnetically. Due to their different magnetic moments, they form a joint iron sublattice with a non-zero magnetization [28–30]. The gadolinium sublattice

couples antiferromagnetically to the joint iron sublattice, giving rise to an exchange mode whose frequency depends on the magnetization difference between the sublattices [28–30]. The difference in temperature dependence between the gadolinium and joint iron sublattices offers a high degree of control and tunability of the exchange mode [28–30]. In this thesis, this high degree of control is utilized to tune the exchange mode into resonance with cavity modes created by the sample interface, leading to an enhanced response.

References

1. Kompfner, R. & Williams, N. T. Backward-Wave Tubes. *Proceedings of the IRE* **41,** 1602–1611 (1953).
2. Cohen, L. Backward-wave oscillators for the 50- to 300-GHz frequency range. *IEEE Transactions on Electron Devices* **15,** 403–404 (1968).
3. Kozlov, G. *et al.* Submillimeter backward-wave oscillator spectroscopy of the rare-earth orthoferrites. *IEEE Transactions on Magnetics* **29,** 3443–3445 (1993).
4. DeMaria, A. J., Stetser, D. A. & Heynau, H. SELF MODE-LOCKING OF LASERS WITH SATURABLE ABSORBERS. *Applied Physics Letters* **8,** 174–176 (1966).
5. *Femtosecond Laser Pulses* (ed Claude Rullière) 2nd ed. (Springer New York, New York, 2004). XVI, 426. ISBN: 978-0-387-01769-3.
6. Fattinger, C. & Grischkowsky, D. Point source terahertz optics. *Applied Physics Letters* **53,** 1480–1482 (1988).
7. Fattinger, C. & Grischkowsky, D. Terahertz beams. *Applied Physics Letters* **54,** 490–492 (1989).
8. Auston, D. H. *et al.* Cherenkov Radiation from Femtosecond Optical Pulses in Electro-Optic Media. *Physical Review Letters* **53,** 1555–1558 (1984).
9. Van Exter, M. & Grischkowsky, D. Optical and electronic properties of doped silicon from 0.1 to 2 THz. *Applied Physics Letters* **56,** 1694–1696 (1990).

10. Katzenellenbogen, N. & Grischkowsky, D. Electrical characterization to 4 THz of N- and P-type GaAs using THz time-domain spectroscopy. *Applied Physics Letters* **61,** 840–842 (1992).

11. Wu, Q. & Zhang, X. Free-space electro-optic sampling of terahertz beams. *Applied Physics Letters* **67,** 3523–3525 (1995).

12. Zielbauer, J. & Wegener, M. Ultrafast optical pump THz-probe spectroscopy on silicon. *Applied Physics Letters* **68,** 1223–1225 (1996).

13. Hebling, J. *et al.* Velocity matching by pulse front tilting for large-area THz-pulse generation. *Optics Express* **10,** 1161–1166 (2002).

14. Hirori, H. *et al.* Single-cycle terahertz pulses with amplitudes exceeding 1 MV/cm generated by optical rectification in $LiNbO_3$. *Applied Physics Letters* **98,** 091106 (2011).

15. Kovalev, S. *et al.* Band-selective third-harmonic generation in superconducting MgB_2 : Possible evidence for the Higgs amplitude mode in the dirty limit. *Physical Review B* **104,** L140505 (2021).

16. Shimano, R. & Tsuji, N. Higgs Mode in Superconductors. *Annual Review of Condensed Matter Physics* **11,** 103–124 (2020).

17. Kovalev, S. *et al.* Non-perturbative terahertz high-harmonic generation in the three-dimensional Dirac semimetal Cd_3As_2. *Nature Communications* **11,** 2451 (2020).

18. Blank, T. *et al.* Empowering Control of Antiferromagnets by THz-Induced Spin Coherence. *Physical Review Letters* **131,** 096701 (2023).

19. Mazin, I. I. & Singh, D. J. Electronic structure and magnetism in Ru-based perovskites. *Physical Review B* **56,** 2556–2571 (1997).

20. Schneider, M., Moshnyaga, V. & Gegenwart, P. Ferromagnetic quantum phase transition in $Sr_{1-x}Ca_xRuO_3$ thin films. *physica status solidi (b)* **247,** 577–579 (2010).

21. Khalifah, P. *et al.* Evolution of transport and magnetic properties near the ferromagnetic quantum critical point in the series $Ca_xSr_{1-x}RuO_3$. *Physical Review B* **70,** 134426 (2004).

22. Dang, H. T. *et al.* Electronic correlations, magnetism, and Hund's rule coupling in the ruthenium perovskites $SrRuO_3$ and $CaRuO_3$. *Physical Review B* **91,** 195149 (2015).

23. Kostic, P. *et al.* Non-Fermi-Liquid Behavior of SrRuO_3: Evidence from Infrared Conductivity. *Physical Review Letters* **81,** 2498–2501 (Sept. 21, 1998).

24. Wang, Y. *et al.* Separated transport relaxation scales and interband scattering in thin films of $SrRuO_3$, $CaRuO_3$, and Sr_2RuO_4. *Physical Review B* **103,** 205109 (2021).

25. Eisterer, M. Magnetic properties and critical currents of MgB_2. *Superconductor Science and Technology* **20,** R47 (2007).

26. Schwarz, L. *et al.* Classification and characterization of nonequilibrium Higgs modes in unconventional superconductors. *Nature Communications* **11,** 287 (Jan. 15, 2020).

27. Giorgianni, F. *et al.* Leggett mode controlled by light pulses. *Nature Physics* **15,** 341–346 (2019).

28. *Handbook of Ferromagnetic Materials* (ed E.P Wohlfarth) 1st ed. (North-Holland Publishing Company, 1980). 592 pp. ISBN: 978-0-444-85312-7.

29. Wang, L.-W. *et al.* First-principles study of magnon-phonon interactions in gadolinium iron garnet. *Physical Review B* **101,** 165137 (2020).

30. Ng, I. *et al.* Survey of Temperature Dependence of the Damping Parameter in the Ferrimagnet $Gd_3Fe_5O_{12}$. *IEEE Transactions on Magnetics* **58,** 1–6 (2022).

1 Methods

In this thesis, a variety of measurement techniques are used to investigate the equilibrium and non-equilibrium properties of different materials. The main focus of this work lays on the optical properties of materials within the THz frequency range; therefore, understanding the principles behind THz generation and detection is important. First, the concept of nonlinear polarization and the resulting nonlinear wave equation will be introduced. After which, the generation of THz radiation via optical rectification with tabletop laser sources is discussed. Additionally, undulators are explained as an alternative source of THz radiation. Furthermore, the THz detection process, both coherent and non-coherent methods, are shown. Lastly, there is a discussion on the various measurement schemes using THz radiation employed in this work.

1.1 Generation and Detection of Terahertz Radiation

The coherent generation and detection of THz radiation, due to the limitations of electronics and optics, is not straightforward. Both processes are based on nonlinear optical effects requiring high power short laser pulses to be efficient. To understand these nonlinear processes, it is essential to consider the underlying physical principles.

1.1.1 Nonlinear Polarization

The foundation for all descriptions for the interaction of electromagnetic fields with matter are the Maxwell equations [1–3]

$$\nabla \cdot \mathbf{D} = \rho, \tag{1.1}$$

$$\nabla \cdot \mathbf{B} = 0, \tag{1.2}$$

$$\nabla \times \mathbf{E} = -\frac{\partial \mathbf{B}}{\partial t}, \tag{1.3}$$

$$\nabla \times \mathbf{H} = \frac{\partial \mathbf{D}}{\partial t} + \mathbf{J}. \tag{1.4}$$

Here, ρ, $\mathbf{J}$, and $\nabla = \left(\frac{\partial}{\partial x}, \frac{\partial}{\partial y}, \frac{\partial}{\partial z}\right)^{\mathrm{T}}$ are the charge density, the electric current density, and the nabla operator, respectively. $\mathbf{D}$, $\mathbf{B}$, $\mathbf{E}$, and $\mathbf{H}$ are the electric- and magnetic flux densities, and the electric- and magnetic- field strength, respectively. These fields are connected via the constitutive relations [1–3]:

$$\mathbf{D} = \epsilon_0 \mathbf{E} + \mathbf{P}, \tag{1.5}$$

$$\mathbf{H} = \frac{1}{\mu_0}\mathbf{B} - \mathbf{M}, \tag{1.6}$$

where **P**, **M** are the polarization and magnetization of a given material in an electric or magnetic field, ϵ_0 and μ_0 are the vacuum permittivity and permeability. In vacuum, without materials or charges present, the Maxwell equations lead to the well known wave equation [2]

$$\nabla^2 \mathbf{E} - \frac{1}{c_0^2} \frac{\partial^2}{\partial t^2} \mathbf{E} = 0, \tag{1.7}$$

with c_0 the speed of light in vacuum.

When a material is present an applied electric field induces a polarization **P** inside of the material. This polarization can depend arbitrarily complicated on the electric field **E** however, in most cases a perturbative description is sufficient [2, 3], e.g.,

$$\mathbf{P} = \epsilon_0 \left(\chi^{(1)} \mathbf{E} + \chi^{(2)} \mathbf{E}^2 + \chi^{(3)} \mathbf{E}^3 ... \right). \tag{1.8}$$

Here, $\chi^{(1)}$ is the linear electric susceptibility defined as $\chi^{(1)} = \epsilon_r - 1$ with ϵ_r the relative permittivity tensor describing the material's dielectric properties [4]. Taking a polarizable material into account, Eq. 1.7 changes to

$$\nabla^2 \mathbf{E} - \frac{1}{c_0^2} \frac{\partial^2}{\partial t^2} \mathbf{E} = \frac{1}{\epsilon_0 c_0^2} \frac{\partial^2 \mathbf{P}}{\partial t^2}. \tag{1.9}$$

In this equation, $\frac{\partial^2 \mathbf{P}}{\partial t^2}$ acts as a driving term for the electric field [2]. The polarization **P** can be divided into a linear $\mathbf{P}^{(1)} \propto \mathbf{E}$ and a non-linear $\mathbf{P}^{\mathrm{NL}}$ contribution. Furthermore, to account for dispersion, the fields can be decomposed into their frequency components as follows:

$$\mathbf{E} = \sum_n \mathbf{E}_n e^{-i\omega_n t}, \tag{1.10}$$

thus transforming Eq. 1.9 into frequency domain and yielding [2]:

$$\nabla^2 \mathbf{E}_n(\mathbf{r}) + \frac{\omega_n^2}{c_0^2} \epsilon^{(1)}(\omega_n) \cdot \mathbf{E}_n(\mathbf{r}) = -\frac{\omega_n^2}{\epsilon_0 c_0^2} \mathbf{P}_n^{\mathrm{NL}}(\mathbf{r}). \tag{1.11}$$

This equation is known as the Helmholtz equation and will act as a basis for further discussion on the terahertz generation in the next section.

1.1.2 Terahertz Generation

Nowadays, multiple methods exist to generate THz radiation for experiments. In this thesis, two main methods for generation were used: Laser-based tabletop sources utilizing optical rectification in the co-linear and tilted-wave-front geometries and accelerator-based undulator sources.

Optical Rectification

The main method used to generate THz radiation in a tabletop setup is based on optical rectification. It can be imagined as difference frequency generation (DFG) between two photons of a short light pulse. Figure. 1.1 shows an illustration of the DFG process in which two photons from a broad near infrared pulse interact inside a nonlinear crystal.

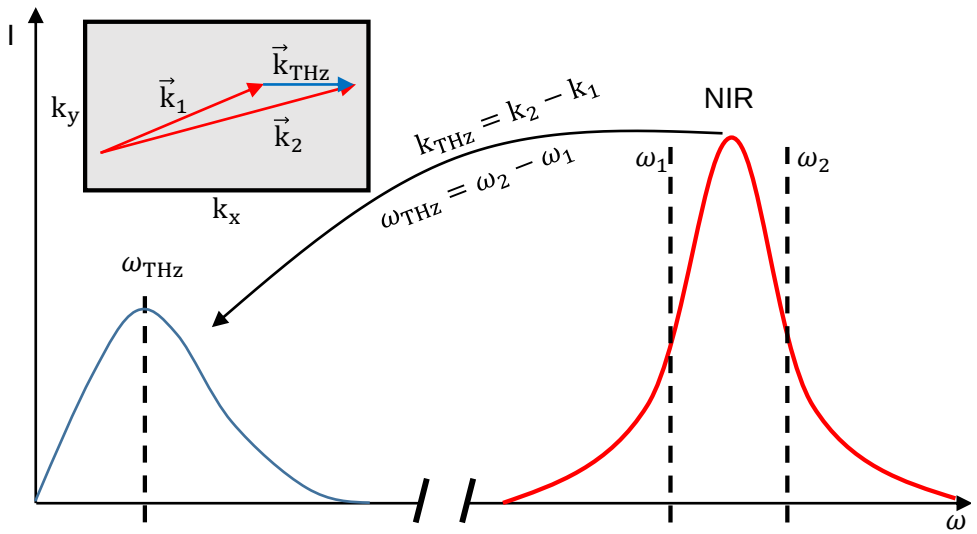

Figure 1.1: Illustration for the difference frequency generation process. Two photons of a near infrared pulse (NIR) generate a photon at THz frequencies.

For this process to occur, the nonlinear crystal must have broken inversion symmetry, meaning a nonzero $\chi^{(2)}$ is required [3]. The emergence of DFG in such a system can be understood by calculating the second-order nonlinear polarization $\mathbf{P}^{(2)}$, using two oscillating electric fields, $\mathbf{E}_1(t)$ and $\mathbf{E}_2(t)$, with different center frequencies ω_1 and ω_2 applied:

$$\mathbf{P}^{(2)} = \epsilon_0 \chi^{(2)} \mathbf{E}_1(t) \mathbf{E}_2(t) \tag{1.12}$$

Assuming the electric fields are sinusoidal, with $\mathbf{E}_x(t) = \mathbf{E}_0 \sin(\omega_x t)$ Eq. 1.12 becomes:

$$\mathbf{P}^{(2)} = \epsilon_0 \chi^{(2)} \left(\frac{1}{2} \mathbf{E}_0^2 \left[\cos((\omega_2 - \omega_1)t) - \cos((\omega_1 + \omega_2)t) \right] \right). \tag{1.13}$$

Two frequency mixing terms emerge, one with the sum (SFG) $(\omega_1 + \omega_2)$ and one with the difference (DFG) $(\omega_2 - \omega_1)$ of both frequencies [3]. The DFG process generates a photon with the energy and momentum relation

$$\omega_{THz} = \omega_2 - \omega_1, \tag{1.14}$$

$$\mathbf{k}_{THz} = \mathbf{k}_2 - \mathbf{k}_1. \tag{1.15}$$

Here ω_x is the frequency and $\mathbf{k}_x$ the momentum of the corresponding photon.

The coupled equations that describe the difference frequency process and satisfying for each frequency component Eq. 1.11 in a loss-less medium are [2]

$$\frac{dE_1}{dz} = \frac{2id_{\text{eff}}\omega_1^2}{k_1 c^2} E_2 E_{THz}^* e^{i\Delta kz}, \tag{1.16}$$

$$\frac{dE_{THz}}{dz} = \frac{2id_{\text{eff}}\omega_{THz}^2}{k_{THz} c^2} E_2 E_1^* e^{i\Delta kz}, \tag{1.17}$$

where E_1 and E_2 are the complex amplitudes generating the DFG, E_2 is assumed to be constant within the crystal, E_{THz} the complex amplitude of the generated light, d_{eff} is the effective element of the $\chi^{(2)}$ tensor, z the position

inside the crystal and

$$\Delta k = k_2 - k_1 - k_{\mathrm{THz}} \tag{1.18}$$

the so called phase mismatch between the 3 waves. It is immediately visible, that the amplitude change dE_{THz}/dz is an oscillating function with the position in the crystal z, and the period $1/2\Delta k$. Therefore, to efficiently generate the THz amplitude, i.e., have the sign of dE_{THz}/dz be constant, the product of the crystal thickness d and Δk needs to be smaller then π to be within a halve cycle oscillation of $e^{i\Delta kz}$ [2]. To understand why reducing Δk towards zero is called phase matching it is instructive to use $k = \frac{n\omega}{c_0}$ and calculate:

$$\frac{n_{\mathrm{THz}}\omega_{\mathrm{THz}}}{c_0} = k_2 - k_1, \tag{1.19}$$

$$\frac{n_{\mathrm{THz}}}{c_0} = \frac{k_2 - k_1}{\omega_{\mathrm{THz}}}. \tag{1.20}$$

The left side is equivalent to the inverse of the phase velocity of the THz pulse $v_{ph.}$ and for sufficient small ω_{THz}, the right side can be expressed as a differential $\frac{dk}{d\omega}$. This being the inverse of the group velocity of the NIR pulse leads to the relation

$$v_{\mathrm{ph.}}^{\mathrm{THz}} = \frac{d\omega}{dk}, \tag{1.21}$$

showing that reducing the phase mismatch means matching the phase velocity of the THz pulse to the group velocity of the generating pulse.

While for some crystals the crystal thickness is easily tunable, there are limits to the practicality of ultra thin crystals. Moreover, a reduced crystal thickness shortens the time for the DFG process to take place reducing the amount of generated THz radiation. Therefore, it is imperative to choose a material and geometry where Δk is as small as possible.

Collinear phase matching The general concept behind collinear DFG is straightforward. A near infrared pulse is either focused into or passes collimated through a $\chi^{(2)}$ crystal. While passing through the crystal, THz radiation is emitted at every point following Huygens-principle as elementary waves [5, 6], therefore the THz wave forms as a cone. Based on the generation pulse and THz energy a maximum thickness satisfying $\Delta kz < \pi/2$ for this configuration can be estimated. Using a pulse centered at 800 nm $\equiv$ 374.7 THz generating a photon with the frequency of 1 THz inside ZnTe yields $z <= 0.0067\,\mathrm{m} = 6.7\,\mathrm{mm}$. However, this calculation is to simple, as it assumes that the only frequency generated is 1 THz, which is an oversimplification.

As illustrated in Figure 1.1, a broad pulse is generated. Therefore, for each generated frequency and generating frequency pair one has to consider the phase matching condition. Further complicated by the fact that materials have dispersion, changing the phase mismatch $\Delta\mathbf{k}$ between the THz and NIR frequencies. Finally, optical active phonons in the THz frequency range have a large influence on the dispersive and absorptive properties, limiting the crystal thickness in most cases to sub 1 mm [3]. The typical peak field strength that can be generated using this generation geometry is $< 10\,\mathrm{kV/cm}$ with nonlinear crystals [3]. However, of note is the recent developments of organic crystals for THz generation achieving field strength of up to 3 MV/cm [7]. The values for the nonlinear crystals used throughout this thesis are shown in table 1.1.

Tilted-Wave-Front Generation Increasing the efficiency of THz generation and achieving peak fields strong enough for THz pulses to become useful as an excitation pulse in ultrafast optics applications requires a more elaborate generation geometry than co-linear generation. Figure 1.2 (a) shows the general concept behind the so called tilted-wave-front generation technique first introduced by Hebling *et al.* in 2002 [5]. The wave-front of the generating NIR pulse is tilted with respect to the propagation direction z. This results in the projected group velocity $v_g \cos\gamma$ along the propagation direction of the

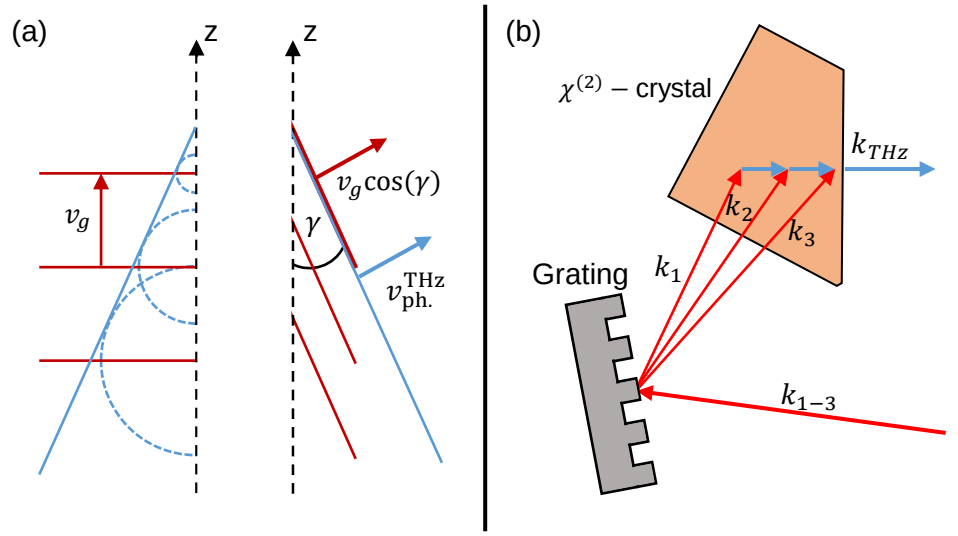

Figure 1.2: Tilted-Wave-Front generation geometry. (a) A NIR wave (red) propagating along z direction. Left side THz radiation (blue) is emitted as circular waves forming a cone of emission. Right side with its wave-front tilted by γ reducing the group velocity v_g projected on the THz emission cone, matching its phase velocity $v_{\mathrm{ph}^{\mathrm{THz}}}$. (b) Collimated light shines on a grating, creating a spacial momentum distribution inside the $\chi^{(2)}-$crystal resulting in large area where the phase matching condition is fulfilled.

cone of THz emission being reduced, therefore matching the phase velocity of the THz pulse.

One way to realize the tilted-wave-front geometry is shown in Fig.1.2(b). Here a grating is used to tilt the wave front. It can be thought of as creating a spatial distribution of the wave vectors of the generating pulse inside the nonlinear crystal. As shown in Figure 1.2 (b), the resulting THz pulse does not travel collinear with the generating pulse in this geometry. By carefully choosing the angle of incidence on the grating, field strength up to 1 MV/cm have been achieved [5, 8].

Another important aspect not depicted in Figure 1.2 (b) is the lens/mirror

system that images and magnifies the spot on the grating into the nonlinear crystal. Furthermore, optical elements introduce chromatic and spherical aberrations, distorting the wave-front and reducing the generation efficiency [8]. In this thesis, a two lens system is used, but other configurations can be considered depending on the specifics of the generating pulse and grating used [8].

Accelerator Based Generation

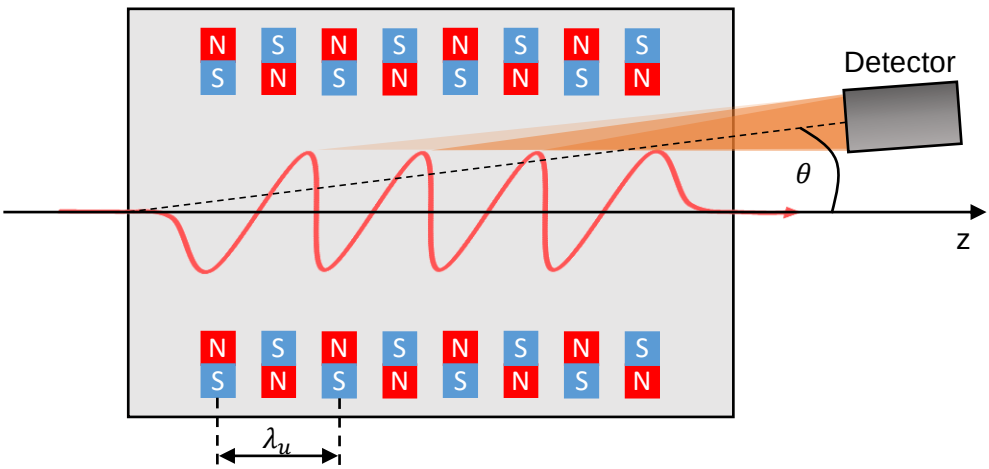

Figure 1.3: Schematic illustration of the function of an undulator. An highly relativistic electron beam (red) passes the undulator along z. The magnetic field (shown as small dipole magnets with N north and S south pole) is perpendicular to the electron velocity and forces the electron path to oscillate with the undulator wavelength λ_u. The accelerated electrons emit electromagnetic radiation in a cone which can be detected or used for experiments.

Another source of strong THz pulses are facility-based accelerator sources [9, 10]. At these facilities, electrons are accelerated to highly relativistic speeds before being sent through an undulator, that can generate electromagnetic radiation [11]. Figure 1.3 shows a schematic of the process of generation inside an undulator. The undulator is comprised out of an alternating configuration

of magnets. The distance between two magnets with the same orientation is called the undulator wavelength λ_u [9, 11]. An electron that enters the undulator from the left side with the velocity v_z is forced onto an oscillating path due to the Lorentz force and while the electrons are accelerated they emit electromagnetic radiation [4, 11]. Since the electrons acceleration period is repeated N_u-times the emitted electromagnetic wave interfere with each other. Wavelength that interfere constructively can be described by the so called undulator equation:

$$\lambda(\theta) = \frac{\lambda_u}{2\gamma^2}\left(1 + \frac{K^2}{2} + (\theta\gamma)^2\right), \tag{1.22}$$

with θ being the angle of detection relative to the undulator axis, $\gamma = 1/\sqrt{1 - \left(\frac{v_z}{c_0}\right)^2}$ being the Lorentz factor and

$$K = \frac{eB\lambda_u}{2\pi m_e c_0} \tag{1.23}$$

the undulator strength parameter with e, B, and m_e being the electron charge, the applied magnetic flux and the electron rest mass, respectively. By tuning the parameters λ_u and B of the undulator and changing the electron velocity v_z one can achieve a wide range of electromagnetic radiation from THz to X-ray radiation [9–11].

1.1.3 Terahertz Detection

In this section, the methods used in this thesis for detecting THz radiation is discussed. First, the function of a bolometer, used for determining the power of a THz pulse, is examined. Second, electro-optic sampling (EOS), which allows the detection of the amplitude and phase of the electric field components of the THz pulse in one measurement, is described.

Bolometer

A bolometer is a detector used for measuring the power of electromagnetic radiation. This process can be seen as a reverse black body radiation process. Here, radiation is focused onto a black body which heats up. The black body is coupled to a controlled heat bath and the temperature of the black body is measured with a resistor. After a new thermal equilibrium is established the incoming power can be estimated by measuring the temperature differential between the heat bath and the black body. Since different frequencies have different absorption coefficients, a bolometer must always be calibrated for the frequency it is going to be used for.

Electro-Optic Sampling

Electro-optic sampling is used to measure the amplitude and phase information of electromagnetic radiation within one measurement. It is based on the Pockels effect which describes the change in refractive index n_0 when an electric field E is applied [3]:

$$\Delta n = n_0^3 d_{\text{eff}} E, \tag{1.24}$$

with d_{eff} being the effective electro-optic tensor element found in Table 1.1, meaning the crystal used for electro-optic sampling needs to have a broken inversion symmetry in the same way the generation crystal does [3]. Since the electric field has a direction, the change in refractive index can be positive or negative, enabling the EOS crystal to be used as a tunable waveplate.

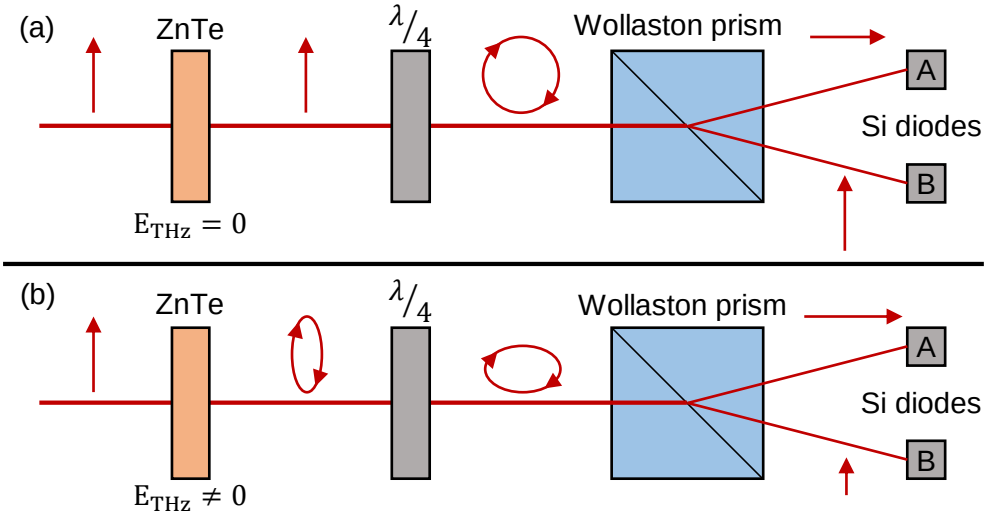

Figure 1.4: Illustration of the function of electro-optic sampling. (a) Linearly polarized light passes through a nonlinear ZnTe crystal with no external electric field applied. The λ / 4-waveplate transforms the linear plorization into circular with equal contribution of horizontal and vertical components. These are split by a Wollaston prism and then detected by Si diodes. (b) An electric field applied at the ZnTe crystal changes the polarization state of the linearly polarized light passing through, resulting in a change of detected intensities at the Si diodes.

Figure 1.4 shows a schematic illustration of the function of electro-optic sampling. In Figure 1.4(a), linearly polarized light passes through a ZnTe crystal with no external field applied. Therefore, after the crystal, the light does not change its polarization state. After passing through a λ / 4-waveplate, the light becomes circularly polarized. This polarization is split by a Wollaston prism in its vertical and horizontal components, which are detected by a pair of Si diodes. Since the intensities of both components are identical, $\Delta I = I_A - I_B = 0$. In Figure 1.4(b) an external field is applied, inducing a birefringence in ZnTe. The resulting polarization after transmission trough the crystal is elliptical and, depending on the applied electric field direction, has a different chirality. This change in ellipticity alters the polarization after the λ / 4-waveplate, making it non-circular. Therefore, the intensities of the horizontal and vertical components after the Wollaston prism differ, resulting

in $\Delta I \neq 0$. The difference in the detected intensity then is proportional to the applied THz electric field [3]:

$$\frac{\Delta I}{I} = \frac{\omega_{800\,\mathrm{nm}} n_0^3}{c_0} d_{\mathrm{eff}} z E_{\mathrm{THz}} \tag{1.25}$$

with z being the thickness of the crystal, $\omega_{800\,\mathrm{nm}}$ the frequency of light at 800 nm.

Crystal	**Spectral Range (THz)**	**Nonlinear Coefficients (pm/V)**	**Near-IR Group Index**	**THz Refractive index**
ZnTe	0.1-3	4	3.24	3.17
GaP	0.1-7	1	3.55	3.32

Table 1.1: Properties of nonlinear crystals used in this thesis [3].

1.2 Measurement Schemes

In this section, the different measurement schemes used in this thesis are explored. First, the THz time-domain spectroscopy setup used to characterize the samples are detailed. Furthermore, the data treatment for THz time-domain data and how to extract the optical properties is discussed. Second, the THz pump-optical probe setup used in Chapter 4 is described. Finally, the THz harmonic generation setup used in Chapter 2 is outlined.

1.2.1 Terahertz Time-Domain Spectroscopy

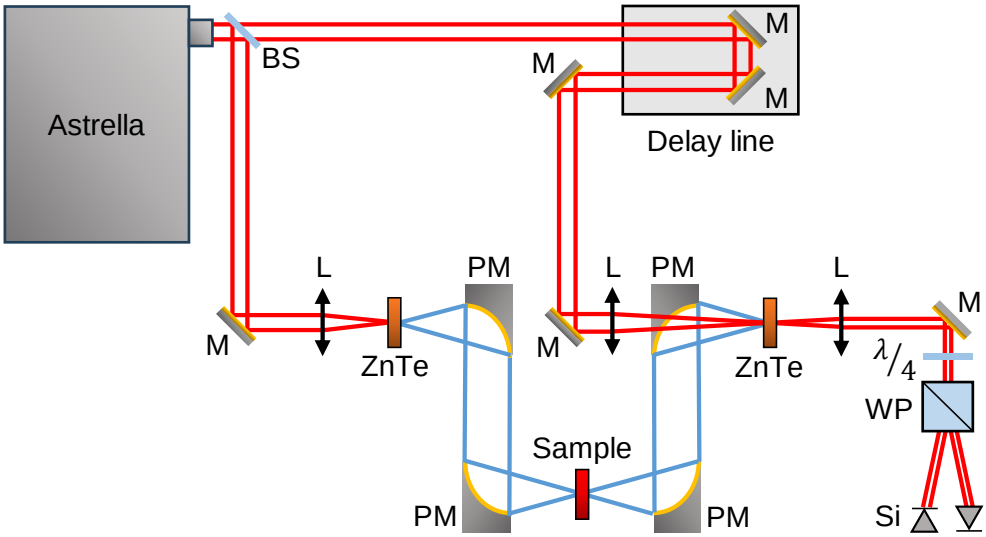

Figure 1.5: Schematic view of the THz time-domain spectroscopy setup. An Astrella (Ti:Sapphire) laser generates 800 nm pulses at a repetition rate of 1 kHz (red beam path) used for generation and detection of THz pulses (blue beam path). Abbreviations shown: (BS) beamsplitter, (M) mirror, (L) lens, (PM) parabolic mirror, (λ / 4) quarter-wave-plate, (WP) Wollaston prim, and (Si) denotes the pair of Silicon diodes.

Terahertz time-domain spectroscopy (THz-TDS) is a commonly used technique for investigating the optical conductivity of samples. THz-TDS has two primary components: The generation and detection of THz radiation [12–15]. Figure 1.5 illustrates the experimental setup for measuring THz-TDS used in

this thesis. Initially, broadband terahertz radiation is generated through co-linear DFG. Subsequently, the emitted THz radiation is collected by a parabolic mirror and focused onto the sample. The sample is placed on a cold finger within a continuous flow cryostat to enable temperature control. To minimize reflective losses, the cryostat windows are made of Polymethylpentene (TPX). After passing through the sample, the THz radiation is collected by another parabolic mirror and then focused onto a 1 mm thick ZnTe crystal for electro-optic sampling. To eliminate absorption by water in the air, the entire THz generation and detection system must be either purged with dry Nitrogen gas or maintained under vacuum.

Analysis of Terahertz Time-Domain Spectra

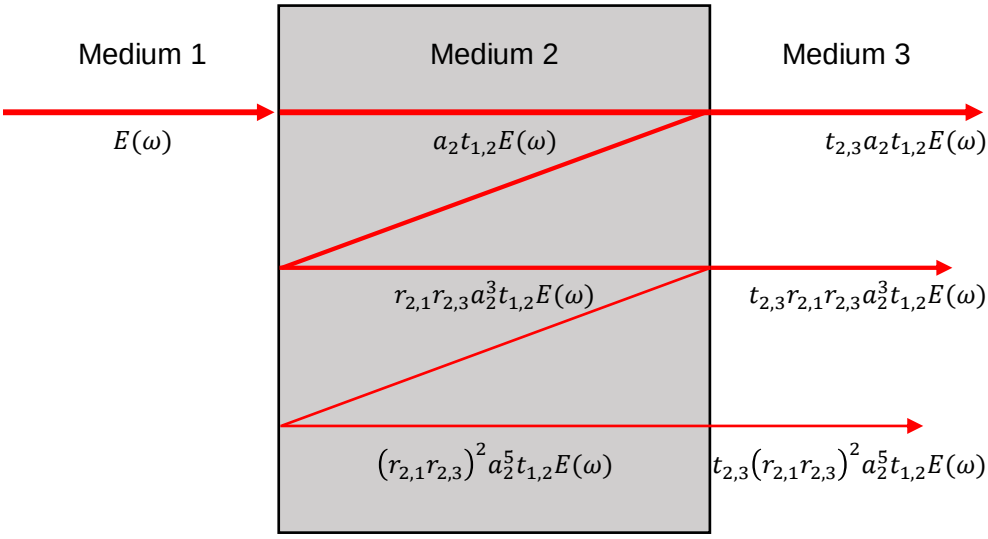

Figure 1.6: Illustration showing how the transmission function is build up with Fresnel coefficients.

Electro-optic detection, as a coherent detection method, allows for the simultaneous measurement of phase and amplitude of the transmitted THz radiation. This capability enables the extraction of the complex transmittance function $\hat{t}(\omega)$, which encodes the material properties in the complex

dielectric function [3]. To model the complex transmittance of our sample, one can imagine the sample as an optically thick slab, as depicted in Figure 1.6. Assuming the electric field before the sample is denoted as $E_0(\omega)$, the transmitted field can be described using Fresnel coefficients [4, 16]:

$$\hat{E}_t(\omega) = t_{2,3} a_2 t_{1,2} \hat{E}_0(\omega), \tag{1.26}$$

where $t_{1,2}$, a_2, and $t_{2,3}$ represent the transmission coefficient at the first interface, absorption coefficient in the medium, and transmission coefficient at the second interface, respectively. Assuming a simple case in which media 1 and 3 are vacuum and medium 2 has the complex refractive index $\hat{n}(\omega)$, one can write [3]:

$$\hat{E}_t(\omega) = \frac{4\hat{n}(\omega)}{(\hat{n}(\omega)+1)^2} e^{i\frac{\omega d}{c}(\hat{n}(\omega)-1)} \hat{E}_0(\omega), \tag{1.27}$$

thus yielding:

$$\hat{t}(\omega) = \frac{\hat{E}_t(\omega)}{\hat{E}_0(\omega)} = \frac{4\hat{n}(\omega)}{(\hat{n}(\omega)+1)^2} e^{i\frac{\omega d}{c}(\hat{n}(\omega)-1)}. \tag{1.28}$$

When the sample is sufficiently thick, internal reflections can be disregarded by truncating the time window before the arrival of reflections. However, this approach has limitations. Considering a typical THz pulse duration of 5 ps and a typical refractive index of 3, if the sample thickness is less than 250 µm, the reflections within the sample arrive within the same time window as the first pulse and must be accounted for in the complex transmittance formula. The calculations follow the same methodology as in Equation 1.28. Additional terms (see Fig. 1.6), that consider the reflections at the sample interface and the absorption occurring during internal reflection have to be introduced. For the general case where the first and second media are vacuum,

the complex transmittance is given by [14, 16]:

$$\hat{t}(\omega) = \frac{4\hat{n}(\omega)}{(\hat{n}(\omega)+1)^2} e^{i\frac{\omega d}{c}(\hat{n}(\omega)-1)} \sum_{i=0}^{k} \left(\left(\frac{\hat{n}-1}{\hat{n}+1} \right)^2 e^{2i\frac{\omega d}{c}\hat{n}(\omega)} \right)^k, \tag{1.29}$$

with the sum taking k-number of reflections into account. To investigate metallic thin films using this geometry, the conductive thin film limit has to be considered. Using Equation 1.29 as a starting point one can do a non-trivial Taylor expansion to arrive at the so called Tinkhams formula [12–14, 17]

$$\hat{t}(\omega) = \frac{1+\hat{n}(\omega)}{1+\hat{n}(\omega)+Z_0\hat{\sigma}_0(\omega)d} \tag{1.30}$$

with $\hat{n}$, $Z_0 = 377\ \Omega$, $\hat{\sigma}_0$, and d being the complex refractive index of the substrate, the permittivity of free space, the complex optical conductivity of the thin film, and the thickness of the thin film respectively [12, 13].

Having discussed how to describe the complex transmission function, the next step is to extract the optical parameters. For Equation 1.30 this can be done analytically by solving for $\hat{\sigma}_0$, but Equations 1.28 and 1.29 are not analytically solvable. To find a value for $\hat{n}$ numerically the common approach [3] is to subtract the measured complex transmittance function from the model function and search for a value of $\hat{n}(\omega)$ where the difference between both functions becomes zero:

$$0 = \hat{t}_{\text{model}}(\hat{n}(\omega)) - \hat{t}_{\text{measured}}(\omega). \tag{1.31}$$

To figure out complex number zeros, an iterative method is used, where the Newton method is the most straightforward choice [3]. The present functions show oscillatory behavior demanding close attention to the initial parameters. When it comes to making an educated guess for the real part of the refractive index, one can use that it describes the speed of light inside the material. Therefore, a practical approach involves extracting the difference in position of the transmission peak and reference peak in the time domain

spectrum. Factoring in the sample thickness allows for the estimation [4, 16]:

$$\Delta t = \frac{d(n-1)}{c} \rightarrow n = \frac{\Delta t \cdot c}{d} + 1. \tag{1.32}$$

As for the imaginary part of the refractive index, it can be estimated by examining the reduced peak amplitude of the transmitted signal and assuming that the real part of $\hat{n}$ is the sole reason for reflection resulting in

$$E_t = E_0 \cdot \frac{4n}{(n+1)^2} e^{-\kappa \frac{\omega}{c} d}, \tag{1.33}$$

as non complex estimation of the transmitted signal [4, 16]. Hence it can be estimated:

$$\kappa = -\frac{c}{\omega d} \ln\left(\frac{(n+1)^2}{4n^2} \cdot \frac{E_t}{E_0}\right). \tag{1.34}$$

Starting with the initial estimate $\hat{n}_{\text{esti.}} = n + i\kappa$, one can calculate the measured $\hat{n}$ for the first frequency point. Subsequently, for each frequency point, the previously calculated value of $\hat{n}$ is used as the new initial estimate. This iterative process progresses through the entire frequency range, thereby enabling the extraction of optical properties across the THz spectrum [3].

1.2.2 Terahertz Pump-Optical Probe

Figure 1.7 shows a schematic view of the terahertz pump-optical probe (TPOP) setup used in chapter 4. The laser used in this experiment is an Astrella system (Coherent). It produces pulses centered at 800 nm, with 6.3 mJ per pulse and a repetition rate of 1 kHz. After the pump and probe beam path are separated using a beamsplitter, it is helpful to describe each beam path individually. The probe beam is reflected multiple times using mirrors (not shown) to compensate for the beam path length difference with the pump path. After which, the probe is focused onto the sample through a borehole in a parabolic mirror to be collinear with the pump beam. The sample is mounted in a continuous flow cryostat for temperature control between 4.2 K

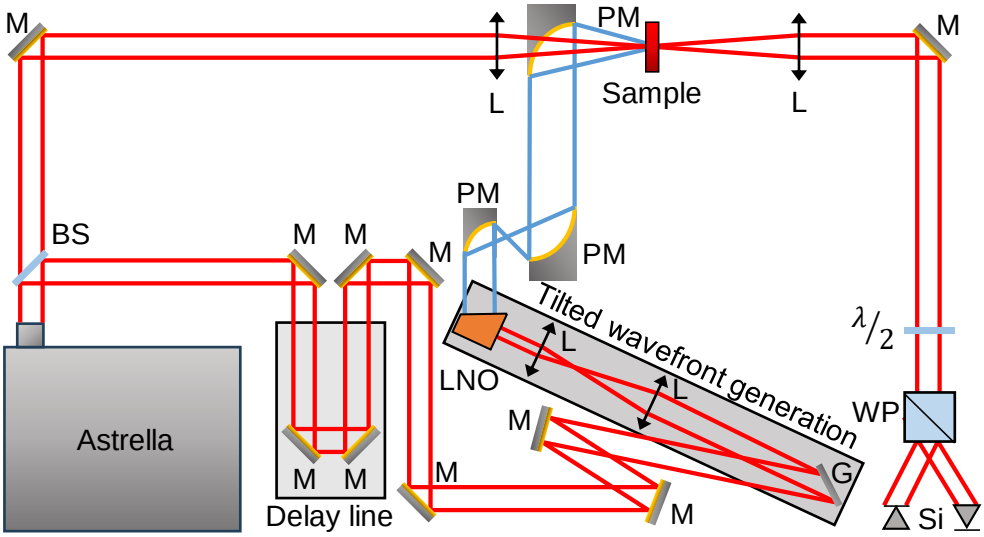

Figure 1.7: Schematic view of the THz pump-optical probe setup. An Astrella (Ti:Sapphire) laser generates 800 nm pulses at a repetition rate of 1 kHz (red beam path) used for generation of the THz pulses (blue beam path) and as a probe. Abbreviations shown: (BS) beamsplitter, (M) mirror, (L) lens, (PM) parabolic mirror, (G) grating, (LNO) $LiNbO_3$ crystal, (λ / 2) halve-wave-plate, (WP) Wollaston prim, and (Si) denotes the pair of Silicon diodes.

and 350 K. At the sample position it is possible to apply an external magnetic field of $\mu_0 H = 150$ mT in or out of plane of the sample. After transmitting through the sample, the probe pulse is collected by a lens and brought to the detection section. In the case of this thesis, THz-induced rotation is detected, therefore the probe beam passes through a λ / 2-plate and afterward through a Wollaston prism. The cross-polarized beams are detected by a pair of balanced Si photo-diodes. However, this can be easily changed to measure THz-induced change in ellipticity by swapping the λ / 2-plate for a λ / 4-plate or THz-induced second harmonic generation by introducing a 400 nm bandpass filter before the diodes.

The pump beam first passes through a motorized delay line to be able to tune the arrival time at the sample position. After which, it is brought into the tilted-wave-front generation stage. The general principle is described in section 1.1.2. Here the -1st order refracted beam and a two lens system to

image the grating into a $LiNbO_3$ crystal are used. The crystal is connected to a copper block that is water cooled to increase the efficiency of the DFG process [18]. The generated THz beam is modulated with a chopper for lock-in detection and afterwards re-sized using a telescope of two parabolic mirrors. After which, it passes two linear polarizers for polarization control and then is focused onto the sample using another parabolic mirror.

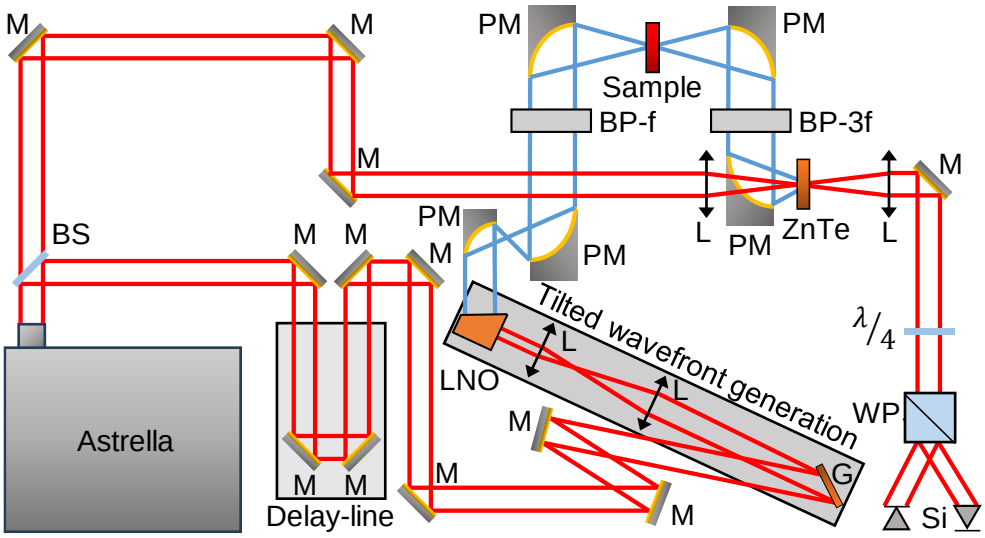

Figure 1.8: Schematic of the third harmonic generation measurement setup. An Astrella (Ti:Sapphire) laser generates 800 nm pulses at a repetition rate of 1 kHz (red beam path) used for generation of the THz pulses (blue beam path) and detection of the generated harmonic. Abbreviations shown: (BS) beamsplitter, (M) mirror, (L) lens, (PM) parabolic mirror, (G) grating, (LNO) $LiNbO_3$ crystal, (λ / 4) quarter-wave-plate, (BP) band pass filter, (WP) Wollaston prim, and (Si) denotes the pair of Silicon diodes.

1.2.3 Terahertz Harmonic Generation

Figure 1.8 shows a schematic view of the terahertz harmonic generation setup used in chapter 2. The harmonic generation measurements in chapter 3 were performed in the Helmholtz Zentrum Dresden Rossendorf; therefore, the THz pulse there was generated by an undulator, not via tilted-wave-front

generation, but the general measurement principle still holds. Similar to section 1.2.2, the beams are separated by a beamsplitter and mostly follow the same beam path. The difference in the pump beam path is that, before being focused on the sample, the broadband THz pulse passes through a bandpass filter centered at frequency f. After which, it is focused on the sample, transmits through the sample and is collimated by a parabolic mirror. Then, it passes through a second bandpass filter at $x \cdot f$, where x is the x-th harmonic that was selected to study. Afterwards, it is focused into a ZnTe crystal for EOS detection. The probe pulse in this experimental configuration is used as a sampling pulse for the EOS detection of the THz electric field.

References

1. Maxwell, J. C. VIII. A dynamical theory of the electromagnetic field. *Philosophical Transactions of the Royal Society of London* **155,** 459–512 (1864).
2. Boyd, R. W. *Nonlinear Optics* 4th ed. ISBN: 978-0-12-811003-4 (Elsevier Science & Techn., 2020).
3. Prasankumar, R. P. & Taylor, A. J. *Optical Techniques for Solid-State Materials Characterization* 1st ed. ISBN: 978-0-367-57692-9 (CRC Press, 2020).
4. Gross, R. & Marx, A. in *Festkörperphysik* (De Gruyter Oldenbourg, 2022). ISBN: 978-3-11-078239-4.
5. Hebling, J. *et al.* Velocity matching by pulse front tilting for large-area THz-pulse generation. *Optics Express* **10,** 1161–1166 (2002).
6. Auston, D. H. *et al.* Cherenkov Radiation from Femtosecond Optical Pulses in Electro-Optic Media. *Physical Review Letters* **53,** 1555–1558 (1984).
7. Rader, C. *et al.* A New Standard in High-Field Terahertz Generation: the Organic Nonlinear Optical Crystal PNPA. *ACS Photonics* **9,** 3720–3726 (2022).
8. Kunitski, M. *et al.* Optimization of single-cycle terahertz generation in $LiNbO_3$ for sub-50 femtosecond pump pulses. *Optics Express* **21,** 6826–6836 (2013).
9. Tanikawa, T. *et al.* A superradiant THz undulator source for XFELs. *Journal of Instrumentation* **14,** P05024 (2019).
10. Neil, G. R. Accelerator Sources for THz Science: A Review. *Journal of Infrared, Millimeter, and Terahertz Waves* **35,** 5–16 (2014).

11. Pellegrini, C., Marinelli, A. & Reiche, S. The physics of x-ray free-electron lasers. *Reviews of Modern Physics* **88,** 015006 (2016).

12. Glover, R. E. & Tinkham, M. Conductivity of Superconducting Films for Photon Energies between 0.3 and $40kT_c$. *Physical Review* **108,** 243–256 (1957).

13. Walther, M. *et al.* Terahertz conductivity of thin gold films at the metal-insulator percolation transition. *Physical Review B* **76,** 125408 (2007).

14. Neu, J. & Schmuttenmaer, C. A. Tutorial: An introduction to terahertz time domain spectroscopy (THz-TDS). *Journal of Applied Physics* **124,** 231101 (2018).

15. Lloyd-Hughes, J. & Jeon, T.-I. A Review of the Terahertz Conductivity of Bulk and Nano-Materials. *Journal of Infrared, Millimeter, and Terahertz Waves* **33,** 871–925 (2012).

16. Hecht, E. *Optics, Global Edition* 5th ed. ISBN: 978-1-292-09696-4 (Pearson, 2016).

17. Meged, M. S. *et al.* Modified Tinkham's Equation for Exact Computation of a Thin Film Terahertz Complex Conductivity. *Journal of Infrared, Millimeter, and Terahertz Waves* **44,** 503–515 (2023).

18. Carbajo, S. *et al.* Efficient narrowband terahertz generation in cryogenically cooled periodically poled lithium niobate. *Optics Letters* **40,** 5762–5765 (Dec. 15, 2015).

2 Third Harmonic Generation and Quantum Critical Systems

2.1 Introduction

The main content of this chapter is the publication "Reinhoffer et al. Strong Terahertz Third-Harmonic Generation by Kinetic Heavy Quasiparticles in $CaRuO_3$. *Physical Review Letters* **132** 196501 (2024)" [1], focusing on the strong THz third-harmonic generation (THG) in $CaRuO_3$. Additionally, further investigation of the nonlinear response in different chemical compositions of the series $Sr_{1-x}Ca_xRuO_3$ are presented. As a basis for understanding these results, this section will cover the physical properties of $Sr_{1-x}Ca_xRuO_3$ and the previous work done in understanding the electronic ground state. Furthermore, the assumptions underlying the Boltzmann transport model, which is used to simulate the nonlinear response of $CaRuO_3$, are discussed.

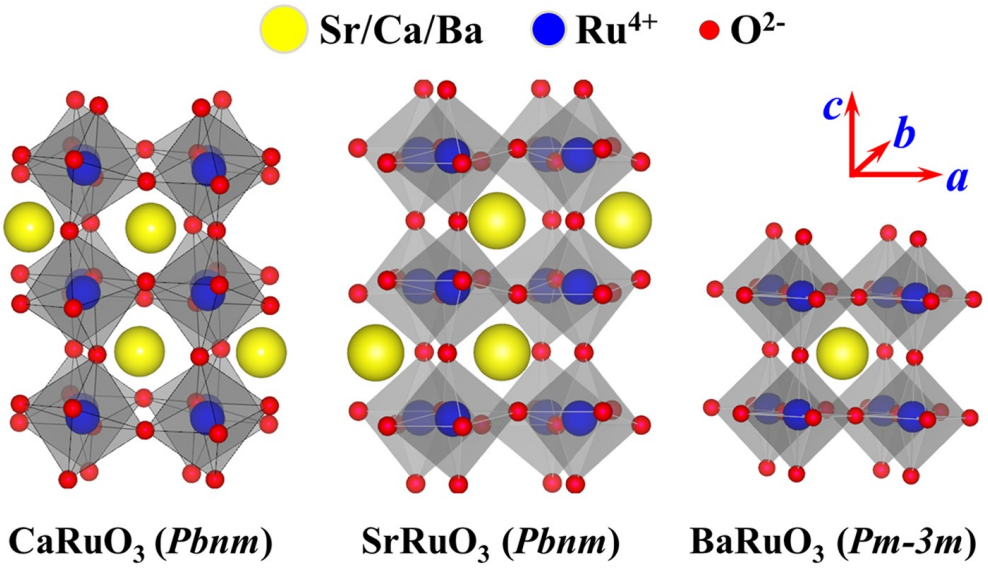

Figure 2.1: Comparison of crystal structures of $CaRuO_3$ (left), $SrRuO_3$ (middle), and $BaRuO_3$ (right). The tilt of the octahedra in $CaRuO_3$ and $SrRuO_3$ result in an orthorhombic crystal structure, compared to the cubic $BaRuO_3$. Furthermore, the distortion of the octahedra is relatively larger in $CaRuO_3$ then in $SrRuO_3$. Picture from Y. Wang *et al.* High stability of electro-transport and magnetism against the A-site cation disorder in $SrRuO_3$. *Sci Rep* **6**, 27840 (2016) under CC 4.0 [2].

2.1.1 $Sr_{1-x}Ca_xRuO_3$

The crystal structure of $Sr_{1-x}Ca_xRuO_3$ makes it a member of the perovskite family. Figure 2.1 illustrates the crystal structures for $CaRuO_3$, $SrRuO_3$ and, for comparison, the cubic perovskite $BaRuO_3$ [2]. The alkaline earth metals strontium and calcium sit in between eight oxygen octahedra with ruthenium at the center. The octahedra are tilted and rotated relative to each other, resulting in the orthorhombic Pbnm structure [2–4]. $CaRuO_3$ has a stronger distortion than $SrRuO_3$ as a result of the smaller ionic radius of Calcium [2]. Although the difference in Ru-O-Ru bond angle between the two compounds is only approximately $\sim 10^\circ$, this small variation leads to a significant difference in their magnetic and electric properties [2, 4].

One of the most pronounced differences is that $SrRuO_3$ is a ferromagnetic metal, whereas no confirmed magnetic ordered ground state exists in

$CaRuO_3$ [5–7]. However, it is widely believed that $CaRuO_3$ is on the verge of magnetic order [8]. This is corroborated by numerous reports on various methods of inducing ferromagnetic order in $CaRuO_3$ [8–10]. Ferromagnetic order has been shown to emerge when applying compressive strain to $CaRuO_3$ via a substrate [8], inducing disorder through partial substitution of Ru with Ti [9], and by introducing hydrogen atoms into the lattice through protonation [10]. In all cases, the main mechanism driving the phase transition is the reduction of the octahedral distortion [10]. Substituting Sr with Ca reduces the magnetic transition temperature from $T_c = 163\,\mathrm{K}$ to 0 K at circa 70 % Ca substitution, indicating a quantum phase transition [6, 7]. In thin films of $Sr_{1-x}Ca_xRuO_3$, the choice of substrate and film thickness can be additional parameters to tune the magnetic properties, such as changing the magnetic easy axis and coercive field strength in $SrRuO_3$ [11].

The relatively stronger octahedral distortion in $CaRuO_3$ compared to $SrRuO_3$, results in enhanced electronic correlations, which influence not only the magnetic properties but the charge transport as well [4]. At low temperatures, the expected temperature dependence of resistivity for most metals is $\rho \propto T^2$, known as Fermi liquid behavior [12, 13]. This dependence is observed for $SrRuO_3$, whereas $CaRuO_3$ deviates from it, with $\rho \propto T^{1.5}$ at temperatures below 10 K, showing non-Fermi liquid behavior [6, 7, 14]. In $Sr_{1-x}Ca_xRuO_3$, the change from Fermi to non-Fermi liquid behavior occurs at $x = 0.7$, the same composition at which the magnetic phase transition is observed, underscoring the strong interplay between structural, electronic, and magnetic properties within this compound family [6, 7]. Recently, the topological nature of the electronic transport in $SrRuO_3$ has emerged as a focal point within the scientific community, opening the way for the exploration of new physical properties in $Sr_{1-x}Ca_xRuO_3$ [15, 16].

Several studies in the THz frequency range on $Sr_{1-x}Ca_xRuO_3$ have aimed to understand the origin and dynamics of the non-Fermi liquid ground state [17–23]. In both $CaRuO_3$ and $SrRuO_3$, studies have found that a narrow zero-frequency peak forms at low temperatures. However, for both compounds, the entire THz spectral range cannot be described by simple Drude theory,

and additionally a Fermi liquid theory-based description fails for $CaRuO_3$ [21]. To describe the THz conductivity in $CaRuO_3$, two different models have been employed: one involving a single conduction band with an energy-dependent scattering rate [20], and the other proposing multiple conduction channels as the origin of the unusual conductivity [23]. A basis for both these interpretations can be found in temperature dependent angle-resolved photo emission spectroscopy measurements on $CaRuO_3$ [24]. Below 80 K, an electron band at the gamma point, characterized by an effective mass of $m^* = 13.5m_e$, becomes coherent. This flat band shows strong electronic correlations and could facilitate low-energy electronic transitions close to the THz spectroscopic window, thereby artificially increasing the observed scattering rate [24]. Furthermore, the presence of multiple bands at the Fermi energy could give rise to multiple conduction channels [23, 24]. These unusual scattering dynamics in the THz frequency range form the basis of the Boltzmann transport model, which is used to phenomenological explain the observed nonlinear response of $CaRuO_3$.

2.1.2 Boltzmann Transport

Describing electron dynamics in electric fields can be done using the time-dependent Boltzmann transport equation [25]:

$$\frac{\partial f(t,\mathbf{p})}{\partial t} = \frac{f_0(\mathbf{p}) - f(t,\mathbf{p})}{\tau} + e\mathbf{E}(t)\cdot\nabla_{\mathbf{p}} f(t,\mathbf{p}), \tag{2.1}$$

with τ being the electron relaxation time, e the electron charge, $\mathbf{E}(t)$ the applied electric field, $\nabla_{\mathbf{p}} = \left(\frac{\partial}{\partial \mathrm{p_x}}, \frac{\partial}{\partial \mathrm{p_y}}, \frac{\partial}{\partial \mathrm{p_z}}\right)^{\mathrm{T}}$ the nabla operator, and $f_0(\mathbf{p})$ the equilibrium electron distribution described by the Fermi-Dirac statistics [4]:

$$f_0(\mathbf{p}) = \frac{1}{e^{\frac{\epsilon(\mathbf{p})-\epsilon_f}{k_B T}} + 1}, \tag{2.2}$$

with $k_B = 1.38\mathrm{x}10^{-23}\ \frac{\mathrm{m^2 kg}}{\mathrm{s^2 K}}$ the Boltzmann constant, T the temperature, ϵ_f the Fermi energy, and $\epsilon(\mathbf{p})$ the electron dispersion. Equation 2.1 has an analytic

solution for $\tau = \text{const.}$ [26] while for the case of $\tau(\mathbf{p})$ there is no analytic solution. Therefore, for a more general solution for arbitrary functions of $\tau(\mathbf{p})$, a numeric approach is chosen. To simplify the simulation, equation 2.1 is reduced to one dimension and rewritten to be solvable using the Euler method:

$$\begin{aligned} f(t+\Delta t, \mathrm{p_x}) = f(t, \mathrm{p_x}) + \Delta t \frac{f(0, \mathrm{p_x}) - f(t, \mathrm{p_x})}{\tau(\mathrm{p_x})} \\ + \Delta t e \mathrm{E_x}(t) \frac{f(t, \mathrm{p_x} + \Delta \mathrm{p_x}) - f(t, \mathrm{p_x})}{\Delta \mathrm{p_x}}, \end{aligned} \tag{2.3}$$

here t and $\mathrm{p_x}$ are now discrete functions with step sizes Δt and $\Delta \mathrm{p_x}$ between elements. The specifics for the used functions $\mathrm{E_x}(t)$ and $\tau(\mathrm{p_x})$ can be found in the publication in section 2.2.4. Here, the focus will be on one particularity of having a non constant $\tau(\mathrm{p_x})$. Taking equation 2.1, solving it for $f_0(\mathrm{p_x})$ and integrating over $\mathrm{p_x}$ gives a function reflecting the number of electrons in the system

$$\int f_0(\mathrm{p_x}) \mathrm{d}\mathrm{p_x} = \int \tau \frac{\partial f(t, \mathrm{p_x})}{\partial t} \mathrm{d}\mathrm{p_x} - \int \tau e \mathbf{E}(t) \cdot \nabla_{\mathrm{p_x}} f(t, \mathrm{p_x}) \mathrm{d}\mathrm{p_x} + \int f(t, \mathrm{p_x}) \mathrm{d}\mathrm{p_x}. \tag{2.4}$$

A problem emerges when τ starts to dependent on $\mathrm{p_x}$; specifically, the integral values on the right side change, which in turn affects the number of electrons. However, in the investigated samples there are no inter band excitation at THz frequencies, therefore the number of electrons in the system is constant. The simplest way to account for this discrepancy between the real experiment and numerical simulation is to renormalize $f(t, \mathbf{p})$ after every time step Δt.

2.2 Strong Terahertz Third-Harmonic Generation by Kinetic Heavy Quasiparticles in $CaRuO_3$

2.2.1 Introduction

Driven by quantum fluctuations associated with the Heisenberg's uncertainty principle [27], a phase transition can occur in the zero temperature limit through tuning of external parameters such as chemical substitution and applied pressure [28, 29]. A variety of novel physical phenomena are observed in the quantum critical metallic systems [27–29]. Whereas in an ordinary metal the electrons can be treated as a weakly interacting liquid of fermions (i.e. Fermi liquid), a metal close to the quantum critical point is more complex which results from competition of different interactions and exhibits various non-Fermi-liquid behaviors [13, 28, 29].

The 4*d* transition-metal oxides are of particular interest in the investigation of exotic quantum phenomena induced by electron correlations [12]. The 4*d* orbitals are characterized by a sizable onsite Coulomb repulsion and at the same time more extended in space than their 3*d* counterparts. Therefore, the 4*d* transition-metal oxides are not necessarily correlation-induced Mott insulators, but can be a strongly correlated metal whose properties cannot be fully described by Fermi-liquid theory [20, 30]. With more than one electron (or hole) in the 4*d* shell, the Hund's coupling between the electrons is important and may even play a dominant role over the effective Coulomb repulsion in determining the magnetic and transport properties [4, 31].

Based on the Ru^{4+} ($4d^4$) ions the perovskite ruthenates $A RuO_3$ (A = Ca or Sr) are representative examples of quantum critical metals. Characterized by a tilt and rotation of each RuO_6 octahedron from the ideal cubic perovskite

This section has been published as a letter in Physical Review Letters [1]. The following is a reformatted version of the original paper as published. Reprinted with permission from Chris Reinhoffer, Sven Esser, Sebastian Esser, Evgeny A. Mashkovich, Semyon Germanskiy, Philipp Gegenwart, Frithjof Anders, Paul H. M. van Loosdrecht, and Zhe Wang *Physical Review Letters* **132** 196501 (2024).

structure, the orthorhombic distortion in $CaRuO_3$ is slightly greater than in $SrRuO_3$. The small structural difference already leads to very different physical properties, since the onsite Coulomb repulsion and the Hund's coupling is only fine balanced which is sensitive to weak perturbation [4]. Whereas $SrRuO_3$ exhibits ferromagnetism at low temperatures, $CaRuO_3$ is located in an adjacent paramagnetic phase and very close to the ferromagnetic quantum critical point [4].

Various unusual metallic properties are observed in $CaRuO_3$. Above 1.5 K the temperature dependence of its dc electrical resistivity deviates clearly from the characteristic quadratic dependence for a Fermi liquid [6, 7, 14, 32]. The optical conductivity of $CaRuO_3$ does not simply follow the Drude model [6, 19, 21, 23, 33]. Above about 0.6 THz, the frequency dependent optical conductivity cannot be described by a Fermi liquid theory [20, 30]. Below 100 K angle-resolved photoemission spectroscopy revealed a well-defined heavy quasiparticle band with an enhanced effective mass of $13.5m_e$ [24], clearly indicating the effects of strong correlations in $CaRuO_3$ [4, 22, 34].

An established approach to characterize a quantum critical system is based on the featured divergent behavior of its thermodynamic quantities, such as thermal expansion, specific heat, or Grüneisen ratio, which exhibit universal scaling with zero temperature being approached [35]. Also the dynamical response functions, e.g. optical conductivity, can follow a universal dependence on frequency, which is characteristic for a quantum critical point, see e.g. [36–39]. However, beyond the thermal equilibrium these quantities may not be well defined. In contrast, nonlinear transport properties have been predicted to be very sensitive to quantum phase transition and can exhibit characteristics for a quantum critical system [40–45]. For instance, close to a magnetic quantum critical point of a metallic system the current density scales nonlinearly with the applied electric field strength [44]; In an insulating quantum critical system of the one-dimensional Hubbard model, very efficient high-harmonic radiation can be generated due to optically induced interband transition [45]. Motivated by these theoretical studies, in this work we investigate the ultrafast nonlinear transport behavior of the proximate

quantum critical metallic system $CaRuO_3$ by using time-resolved terahertz (THz) third-harmonic generation (THG) spectroscopy.

Comparing with the short electrical current pulses of microseconds which lead primarily to Joule heating effects in the sample [46], the THz pulses with much shorter pulse duration probe directly the sub-picosecond (ps) nonlinear transport properties without considerable heating issues. The nonlinear current related to the THz field driven kinetics of the quasiparticles is studied by measurement of THz THG. The third-harmonic radiation is observed in the frequency range where the dynamical response of the system is beyond a description by the Fermi-liquid theory [20, 30]. In contrast to the mechanism involving interband transitions [45, 47] which requires higher-energy pump pulses e.g. mid-infrared [48], in our experiment only the bands in the vicinity (a few meV) of the Fermi surface are essentially responsible for the THz harmonic generation. Our results show that third-order nonlinear THz susceptibility in $CaRuO_3$ is resolvable below 80 K and increases evidently with decreasing temperature. For different driving frequencies, the normalized temperature-dependence curves overlap very well with each other. The master curve resembles the temperature dependent evolution of the spectral weight of the heavy quasiparticle band [24], pointing to the crucial role of the strong correlations to the observed nonlinear responses.

2.2.2 Experimental Details

High-quality $CaRuO_3$ thin films were grown using metal-organic aerosol deposition technique [20] on 3° miscut (110) oriented $NdGaO_3$. We carried out the THz spectroscopic measurements on a thin film with a residual resistivity ratio (RRR) of 35 and a thickness of 43.7 nm which has been characterized previously [46]. A continuous helium-flow cryostat was installed for measurements at different temperatures. Broadband THz radiation was generated in $LiNbO_3$ using the tilted pulse-front optical rectification technique [49, 50] based on a Ti:sapphire amplified laser (800 nm, 1 kHz, 6 mJ). Narrowband THz driving pulses with centre frequencies of $f = 0.4$, 0.5, and 0.7 THz were prepared by using corresponding bandpass filters with full width at

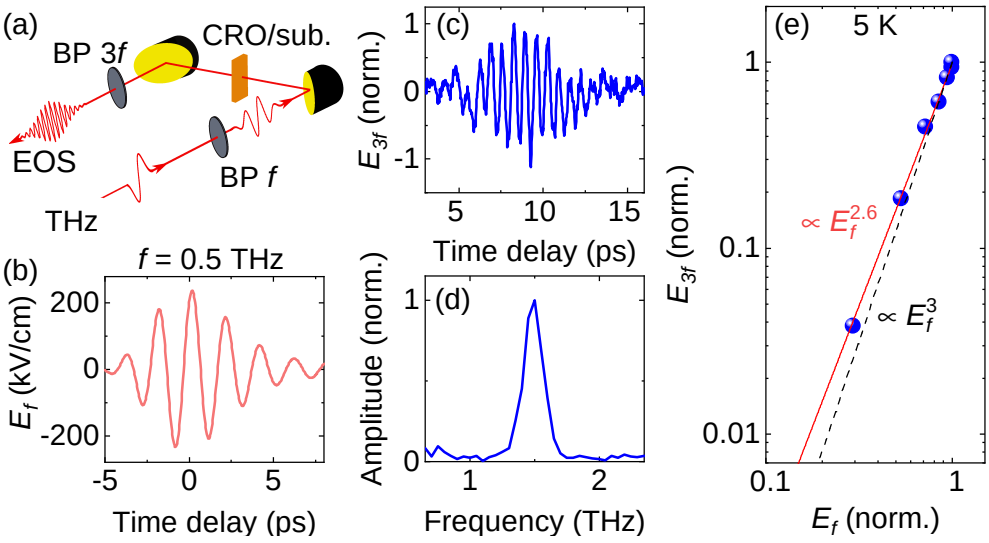

Figure 2.2: (a) Illustration of the THz THG experiment. THG from $CaRuO_3$ thin film is measured in transmission configuration and the THz electric field is detected by electro-optic sampling (EOS). (b) Electric field of the THz pump pulse with a central frequency of $f = 0.5$ THz. (c) THz electric field emitted from $CaRuO_3$ at 5 K measured through a $3f$-bandpass (BP) filter. (d) Spectrum obtained by Fourier transformation of the waveform in panel (c). (e) THG amplitude E_{3f} vs driving field amplitude E_f, which follows a power law dependence of $E_{3f} \propto E_f^{2.6}$ (solid line) only slightly deviated from the perturbative dependence $\propto E_f^3$ (dashed line).

half maximum of $0.2f$ and an out-of-band transmission of < -30 dB [see Fig. 2.2(b) for $f = 0.5$ THz]. The emitted THz electric field was recorded by electro-optical sampling (EOS) [51] [see Fig. 2.2(a) for an illustration]. For the detection of THG another bandpass filter with a centre frequency of $3f$ was placed after the sample to suppress the linear response. For fluence dependent measurements [Fig. 2.2(e)], two wire-grid polarizers were installed in front of the sample.

2.2.3 Results

The crystal structure of $CaRuO_3$ belongs to the centrosymmetric *Pbnm* space group, therefore the even-order nonlinear susceptibilities vanish and we will

focus on the third-harmonic generation. For a driving pulse of $f = 0.5$ THz, the emitted THz electric field from the $CaRuO_3$ thin film at 5 K is shown in Fig. 2.2(c). An evident oscillation of the electric field in time domain corresponding to a frequency of $3f = 1.5$ THz is the third-harmonic generation, which can be directly read from its Fourier transform spectrum [see Fig. 2.2(d)]. Figure 2.2(e) displays fluence dependence of the integrated amplitude E_{3f} of the emitted electric field, which exhibits a power law behavior of $E_{3f} \propto E_f^{2.6}$ slightly deviated from the perturbative dependence of $\propto E_f^3$. At the highest fluence, we can estimate a third-order nonlinear susceptibility via $|\chi^{(3)}| = \frac{E_{3f}}{E_f^3} = 1.4 \times 10^{-17}$ $V^{-2}m^2$.

We further characterize the nonlinear THz response by measuring the THG as a function of temperature. As shown in Fig. 2.3(a), the strongest THG signal is observed at 3.3 K in the time-delay window from 5 to 12.5 ps. This signal decreases gradually with increasing temperature. At 80 K the signal after 7 ps becomes nearly indiscernible, while before 7 ps a weak signal persists until 300 K. At 300 K our fluence dependent measurement shows that this persisting signal follows a linear dependence on the fluence, thus is a transmission of the driving pulse rather than third-harmonic radiation. The enhancement of the signal after 7 ps with decreasing temperature is more clearly seen in the Fourier transform spectra in Fig. 2.3(b). The integrated amplitude of the emitted $3f$ and f components is presented in Fig. 2.3(c) and Fig. 2.3(d), respectively, as a function of temperature. Below 80 K the substantial increase of the third-harmonic radiation [Fig. 2.3(c)] is accompanied with an evident drop of the transmission for the fundamental frequency $f = 0.5$ THz [Fig. 2.3(d)]. The monotonic decrease of transmission at low frequencies reflects an enhanced metallic response with decreasing temperature, which is consistent with the observation of reduced dc resistivity and higher THz reflectivity [14, 20].

For a fixed driving field, the observed temperature dependent transmission indicates that the effective THz field in the thin film varies with temperature, therefore we use the nonlinear susceptibility $|\chi^{(3)}| = \frac{E_{3f}}{E_f^3}$ to characterize the nonlinear dynamical responses of $CaRuO_3$ at different temperatures, also

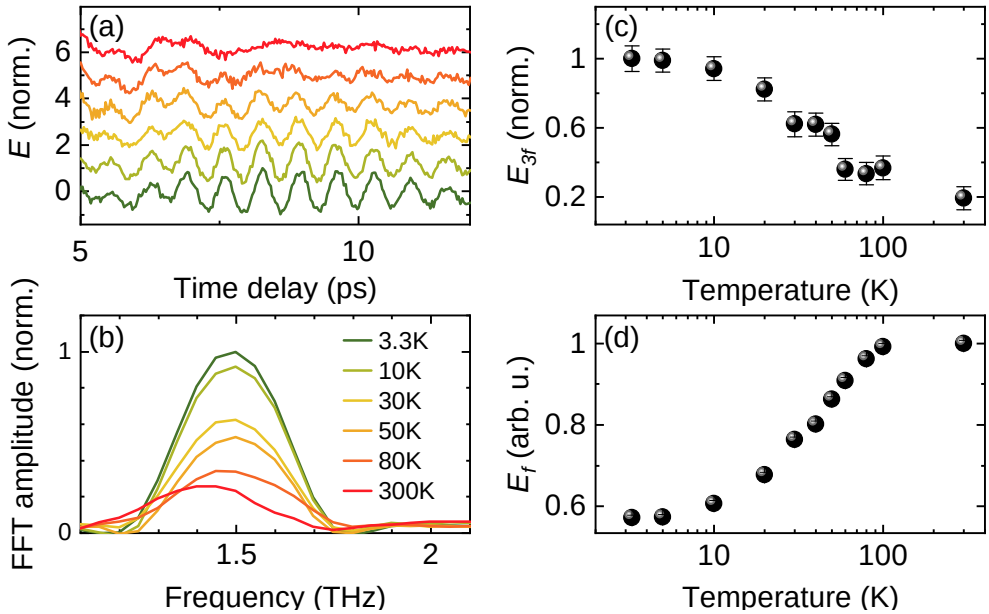

Figure 2.3: (a) THG signal in time domain at different temperatures. (b) Fourier amplitude of the signal in panel (a). (c) THG amplitude E_{3f} and (d) the transmitted amplitude E_f of the fundamental frequency as a function of temperature.

for different THz field strengths and frequencies. Figure 2.4(a) shows the experimentally determined $|\chi^{(3)}|$ as a function of temperature for different driving frequencies of $f = 0.4$, 0.5, and 0.7 THz. While at a fixed temperature the absolute value of $|\chi^{(3)}|$ increases at lower frequencies, for all three frequencies $|\chi^{(3)}|$ monotonically decreases at elevated temperature and vanishes above 80 K. By normalizing $|\chi^{(3)}|$ with respect to the maximum value of each frequency [see Fig. 2.4(b)], the three curves overlap well with each other, exhibiting a frequency-independent temperature dependence of nonlinear response.

This master curve reveals a characteristic temperature scale, below which a well-defined electronlike quasiparticle band is formed right below the Fermi energy, as directly observed by angle-resolved photoemission spectroscopy

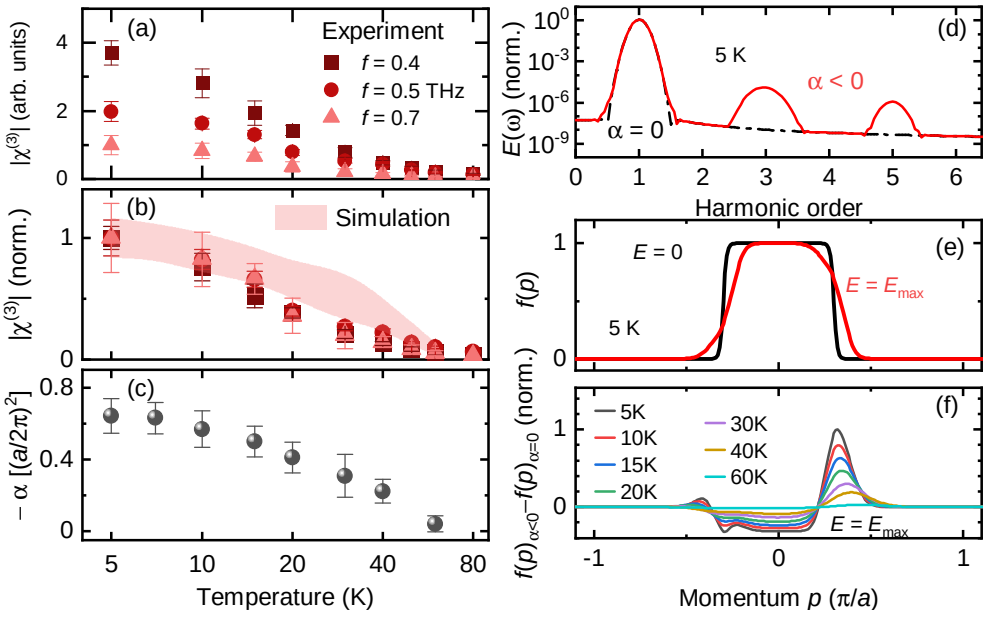

Figure 2.4: (a) Experimentally determined $|\chi^{(3)}| \propto \frac{E_{3f}}{E_f^3}$ as a function of temperature for driving frequencies of 0.4, 0.5, and 0.7 THz. (b) Normalized $|\chi^{(3)}|$ for THz drive frequencies of $f = 0.4$, 0.5, and 0.7 THz follow the same temperature dependence. The shaded area represents the simulated $|\chi^{(3)}|$ where the width reflects the uncertainties of experimentally determined α in (c) [20]. (d) Simulated spectral amplitude of emitted electric field for $\alpha = 0$ and $\alpha < 0$ at 5 K versus harmonic order. (e) Snapshots of charge-carrier distribution $f(p)$ at zero and peak THz electric field $E_{\max}$ at 5 K. (f) Changes of charge-carrier distribution at $E_{\max}$ for different experimental values of α with respect to that of $\alpha = 0$.

[24]. In comparison with density functional theory calculations, this quasiparticle band is strongly renormalized with an effective mass of $13.5m_e$, indicating a strong correlation effect. For the spatially more extended $4d$ orbitals in $CaRuO_3$, the strong correlations result from the Hund's coupling [4, 31], which has been found also to account for a similar temperature dependent evolution of heavy quasiparticles in a related compound Sr_2RuO_4 [52, 53]. The characteristic temperature is much higher than the scale, i.e. $T < 1.5$ K, where a Fermi-liquid type T^2 dependence of electrical resistivity appears [20],

but reflects a coherence-incoherence crossover of the heavy quasiparticles related to the strong correlations [52]. At higher temperatures a good metallic response in optical conductivity is absent as manifested by the disappearance of Drude-like behavior at low frequencies [21].

It has been established that THz high-harmonic radiation can be generated from nonlinear kinetics of relativistic quasiparticles with linear dispersion relation (see e.g. [25, 26, 54]). According to the band-structure calculations [20, 31], some of the bands close to the Fermi surface in $CaRuO_3$ may likely follow a linear dispersion relation, which potentially also leads to THz third-harmonic generation. However, these bands have not been experimentally confirmed so far. Moreover, the harmonic generation associated with a linear dispersion should be well visible already at room temperature. Therefore, our observed enhancement of the third-harmonic generation at low temperatures is unlikely governed by these bands. In contrast, we ascribe the observed nonlinear response to THz field driven kinetics of the experimentally observed heavy quasiparticles in $CaRuO_3$ with an energy-dependent scattering rate.

2.2.4 Theoretical Description

We describe the field driven transport by using the time-dependent Boltzmann equation

$$\left(\frac{\partial}{\partial t}+\frac{1}{\tau}\right) f(t,\mathbf{p}) - e\mathbf{E}(t)\cdot\nabla_{\mathbf{p}} f(t,\mathbf{p}) = \frac{f_0(\mathbf{p})}{\tau}, \tag{2.5}$$

where $f(t,\mathbf{p})$ denotes the time-dependent distribution function at time t and momentum $\mathbf{p}$ for a band that is characterized by a dispersion relation $\epsilon(\mathbf{p})$. $\mathbf{E}(t)$ is the electric field of the THz drive and $f_0(\mathbf{p})$ is the Fermi-Dirac distribution at the equilibrium state. For a parabolic band with an energy-independent relaxation time in a slowly varying electric field, Eq. (2.5) reduces to the Drude model and the corresponding transport behavior follows the Ohm law, i.e. $\mathbf{j}=\sigma\mathbf{E}$. In the relevant frequency range of our experiment, previous studies in the linear response regime have revealed clear deviation

of the transport behavior in $CaRuO_3$ from the description by the Drude model [6, 19, 21, 23, 33], and also predicted energy-dependent relaxation time due to electron-electron correlations [4, 31]. To parametrize the experimentally observed energy-dependent relaxation time in Ref. [20], we assume a linear dependence in our simulation, i.e. $\tau(\mathbf{p}) = \tau_0 \left(1 + \alpha \mathbf{p}^2\right)$ with τ_0 being the energy-independent scattering time and $\alpha < 0$ describing the increased scattering rate at higher energy.

We solve Eq. (2.5) numerically for a heavy electron parabolic band with the experimental parameters [20, 24], i.e. an enhanced quasiparticle mass of $13.5m_e$, a Fermi energy of $E_F = 7$ meV, $\tau_0 = 1$ ps and a THz peak electric field of $E_{\max} = 50$ kV/cm. The experimental values of α at various temperatures are derived from the results of linear THz spectroscopy [20] and given in Fig. 2.4(c). In the simulation a multicycle THz pulse with a Gaussian envelop is adopted, whose central frequency and bandwidth are set in accord with the experimental values. The THz field driven current density is evaluated by $\mathbf{j}(t) = -e \int \frac{d\mathbf{p}^3}{(2\pi\hbar)^3} f(t, \mathbf{p}) \nabla_{\mathbf{p}} \epsilon(\mathbf{p})$, thereby we obtain the time-dependent emitted THz electric field as the time derivative of the current density.

The emitted THz signal contains components of the fundamental frequency and the third harmonic radiation. Through Fourier transformation we derive the third-order nonlinear susceptibility as $|\chi^{(3)}| \propto \frac{E_{3f}}{E_f^3}$ with E_{3f} and E_f being integrated amplitudes in the frequency domain around $3f$ and f, respectively, which as a function of temperature is presented in Fig. 2.4(b). One can see that corresponding to a negligible energy dependence of the relaxation time (i.e. $\alpha \approx 0$) at high temperatures [see Fig. 2.4(c)], the third-order nonlinear susceptibility is essentially zero. This means that a heavier effective mass alone (corresponding to a weaker curvature of the parabolic dispersion) cannot account for the experimentally observed THG. With decreasing temperature, the absolute value of α increases [Fig. 2.4(c)], which leads to an enhancement of the THG [Fig. 2.4(b)]. Therefore, a more evident dependence of the scattering rate on energy is responsible for the enhanced THz nonlinearity.

To further illustrate this effect, in Fig. 2.4(d) we compare the amplitude

of emitted THz field for zero and a negative value of α at 5 K. While for $\alpha = 0$ only radiation of the fundamental frequency is emitted, for $\alpha < 0$ higher-order harmonic generation becomes very evident. Microscopically, the field-driven nonlinear current density is closely related to the deviation of the charge-carrier distribution from the Fermi-Dirac function. The snapshot of the distribution corresponding to the peak THz field (i.e. $E = E_{\max}$) is presented in Fig. 2.4(e) together with the zero-field distribution at 5 K for comparison. Under the drive of the THz field, the distribution is clearly stretched, which cannot be described by a Fermi-Dirac function, featuring the important contribution of the nonthermal states to the nonlinear response.

Even for $\alpha = 0$ the strong THz electric field can drive the system far from thermal equilibrium, therefore it is instructive to quantify the corresponding nonthermal effects due to the energy-dependent scattering. As displayed in Fig. 2.4(f), we evaluate the changes of distribution function at the peak field $E_{\max}$ for α's at different experimental temperatures with respect to that of $\alpha = 0$. The changes are more significant at lower temperatures corresponding to larger absolute values of α [see Fig. 2.4(c)]. As reflected by the positive and negative changes around the Fermi level, the charge carrier distribution is more strongly stretched away from a Fermi-Dirac function with increasing α, which lead to the observed enhancement of THz harmonic generation.

Going beyond the phenomenological model, it is highly compelling to develop a microscopic description of the many-body nonequilibrium dynamics. Since the microscopic properties and linear responses of $CaRuO_3$ in equilibrium state have been very well described in the framework of dynamical mean-field theory (DMFT) [4, 31], to carry out a nonequilibrium DMFT calculation [55] in accord with our experimental settings will provide important microscopic understanding of the nonlinear responses of the quantum many-body nonequilibrium states. Complementary to our terahertz harmonic generation spectroscopy, a time-resolved terahertz pump angle-resolved photoemission-probe spectroscopic investigation should enable a direct comparison with the nonequilibrium DMFT calculations.

2.2.5 Conclusion

To conclude, by driving the strongly correlated metal $CaRuO_3$ with intense terahertz field, we observed third-harmonic radiation below 80 K, in agreement with the temperature dependence of a heavy quasiparticle band emerging close to the Fermi surface. The field-driven kinetics of the heavy quasiparticles is simulated by adopting a Boltzmann transport equation with an energy-dependent scattering rate, which reflects the previously observed non-Drude behavior. The observed third-harmonic generation is not necessarily a unique feature for $CaRuO_3$, but should represent in general a peculiar nonlinear characteristic for nonequilibrium states in strongly correlated metals close to a quantum critical point [40–45, 47, 56, 57]. We anticipate that our work will motivate further studies of the universal characteristic nonlinear responses in quantum critical metals.

2.2.6 Contributions

Zhe Wang conceived the project. Chris Reinhoffer performed the measurement with help of Semyon Germanskiy. The numerical simulation of the Boltzmann transport model were performed by Chris Reinhoffer. The sample was grown and characterized in the group of Paul Gegenwart by Sven Esser and Sebastian Esser. Chris Reinhoffer, Semyon Germanskiy, Evgeny Mashkovich, Paul van Loosdrecht and Zhe Wang discussed the experimental results and analysis. Chris Reinhoffer wrote the main part of the manuscript in close collaboration with Zhe Wang and Evgeny Mashkovich. All mentioned authors helped with refining the final written manuscript.

2.3 Third-Harmonic Generation in $Sr_{1-x}Ca_xRuO_3$

As mentioned in the previous section, the THG in $CaRuO_3$ might not be unique but could be a more general characteristic for strongly correlated metals with quantum phase transitions. To verify this suggestion, the first step is to investigate the nonlinear response to a THz drive in $Sr_{1-x}Ca_xRuO_3$ for different values of x before extending it to different materials. Therefore, in this section the linear and nonlinear response of $Sr_{1-x}Ca_xRuO_3$ in the THz frequency region will be investigated for four samples of varying chemical composition.

For the purpose of this investigation, new samples were grown using the pulsed laser deposition (PLD) technique. Similar to section 2.2, the samples were grown on a 0.5 mm thick, [110]-oriented $NdGaO_3$ substrate. To have a comparison with the previous measurements for samples grown with metal-organic vapor deposition, a 40 nm $CaRuO_3$ film was grown. Furthermore, 20 nm samples of $Sr_{1-x}Ca_xRuO_3$ with $x \in \{0, 0.6, 0.8, 1\}$ were grown. First, the focus will be on the linear and nonlinear response of the batch of 20 nm samples. After which, the nonlinear response of the 20 nm and 40 nm $CaRuO_3$ sample will be investigated and compared.

2.3.1 Terahertz Time-Domain Spectroscopy

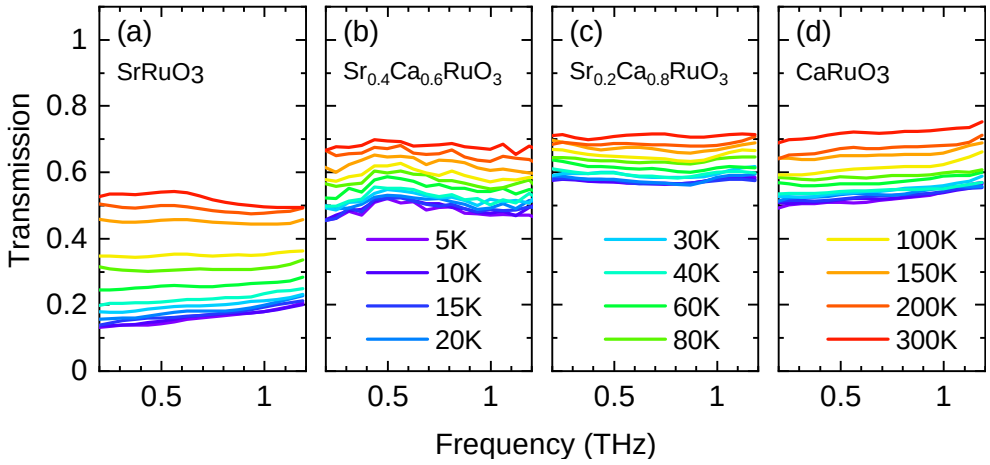

Figure 2.5: Temperature dependent transmission of (a) $SrRuO_3$, (b) $Sr_{0.4}Ca_{0.6}RuO_3$, (c) $Sr_{0.2}Ca_{0.8}RuO_3$, and (d) $CaRuO_3$.

Previous measurements have shown that the conducting properties of $Sr_{1-x}Ca_xRuO_3$, depending on the composition, can be quite different [21]. To characterize the conductivity of the four samples used, temperature dependent terahertz time-domain spectroscopy measurements were performed. Figure 2.5 shows the transmission spectra as a function of temperature for all four 20 nm samples. $SrRuO_3$ shows the strongest temperature dependence, while $Sr_{0.2}Ca_{0.8}RuO_3$ shows the least, with $CaRuO_3$ and $Sr_{0.4}Ca_{0.6}RuO_3$ being in between. The transmission of $SrRuO_3$ decreases from 50 % at 300 K to $\sim$ 18 % at 5 K for 0.5 THz changing from a flat line to having a positive slope between 300 and 5 K, indicating a redistribution of spectral weight from high to low frequency. An explanation for this phenomena would be the formation of a zero frequency Drude peak at low temperatures known to occur in these samples [21]. The strong decrease of the transmission and the formation of a zero frequency peak indicate a metallic sample with few defects resulting in a scattering rate in the THz region.

For $CaRuO_3$ and $Sr_{0.4}Ca_{0.6}RuO_3$ shown in Fig. 2.5 (d) and (b), a similar decrease in transmission, from ~ 70 % at 300 K to ~ 50 % at 5 K at 0.5 THz, is observed. The higher transmission at low temperatures in $CaRuO_3$ compared to $SrRuO_3$ is expected, because the conductivity of the later is three times larger then the former [21]. However, one would expect the low temperature conductivity of $CaRuO_3$ to be larger then $Sr_{0.4}Ca_{0.6}RuO_3$ because the conduction properties in a mixed compound are inherently dominated by the structural disorder in the lattice [21]. The reason for the apparently bad conducting properties in $CaRuO_3$ is that the target used for the PLD growth is stoichiometric but the growth process via PLD can induce Ru deficiencies [58]. The $SrRuO_3$ target has an overabundance of Ru to account for this phenomenon. $Sr_{0.2}Ca_{0.8}RuO_3$ (Fig. 2.5 (c)) shows the weakest temperature dependence of the transmission indicating a low conductivity and high scattering rate similar to $Sr_{0.4}Ca_{0.6}RuO_3$.

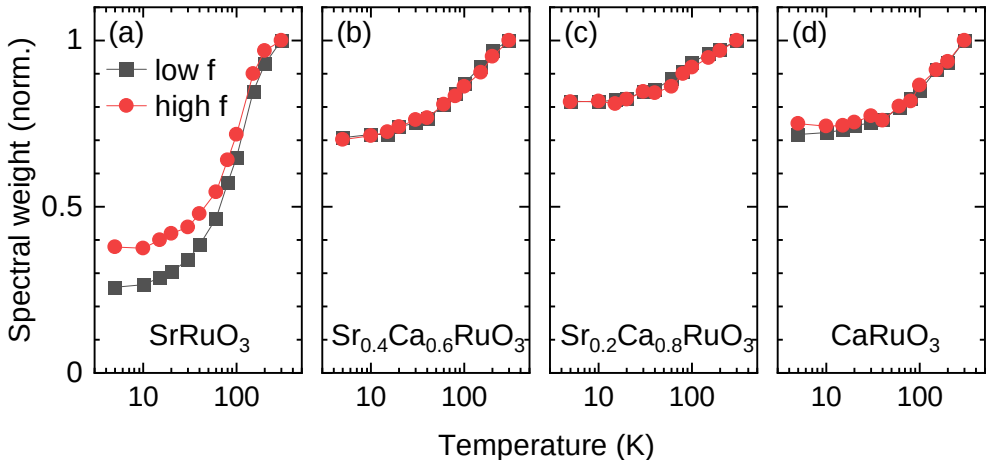

Figure 2.6: Temperature dependence of the integrated spectral weight of (a) $SrRuO_3$, (b) $Sr_{0.4}Ca_{0.6}RuO_3$, (c) $Sr_{0.2}Ca_{0.8}RuO_3$, and (d) $CaRuO_3$. Low f is the integral from 0.2 THz to 0.5 THz and high f is the integral from 0.9 THz to 1.2 THz from Fig. 2.5 (a)-(d).

Observing the formation of the zero frequency Drude peak without having to extract the optical conductivity data can be done by integrating over

different spectral regions in Fig. 2.5. Figure 2.6 (a) - (d) shows the temperature dependence of two different spectral weights, at low frequency (low f) from 0.2 to 0.5 THz and at high frequency (high f) from 0.9 to 1.2 THz, for all four samples. For $SrRuO_3$ there is a clear difference between the low f and high f regions appearing below 100 K indicating a redistribution of spectral weight from high to low frequency. This happens in the same temperature region where the zero frequency peak appears [21]. For both mixed compounds $Sr_{0.4}Ca_{0.6}RuO_3$ and $Sr_{0.2}Ca_{0.8}RuO_3$ the low f and high f spectral weights show no difference over the whole temperature range. The expected behavior for metals with a scattering rate larger then the THz frequency is that they show a flat conductivity, matching our observation and expectation for the mixed compounds [21]. $CaRuO_3$ on the other hand shows a small but visible difference between low f and high f at low temperatures indicating a small spectral weight redistribution. For $CaRuO_3$ thin films a zero frequency peak has been observed [19–21].

2.3.2 Terahertz Third-Harmonic Generation

The next step is the investigation of differences in the nonlinear THz response of $Sr_{1-x}Ca_xRuO_3$ with $x \in \{0, 0.6, 0.8, 1\}$. For that purpose first, the fluence dependence of the THG in the 20 nm samples is compared. After which, the temperature dependence of the emitted THG and the nonlinear susceptibility will be shown. Furthermore, the difference in THG for samples of different thickness is investigated for $CaRuO_3$.

Fluence Dependence

One of the first steps in investigating a nonlinear response is to measure the fluence dependence to find out if the signal is perturbative or non-perturbative in nature. To perform fluence dependence measurements, four components were used. The first is a pair of wire grid polarizers, which control the strength of the THz field while maintaining its initial polarization. The second component is a set of bandpass filters, with a filter at 0.7 THz placed

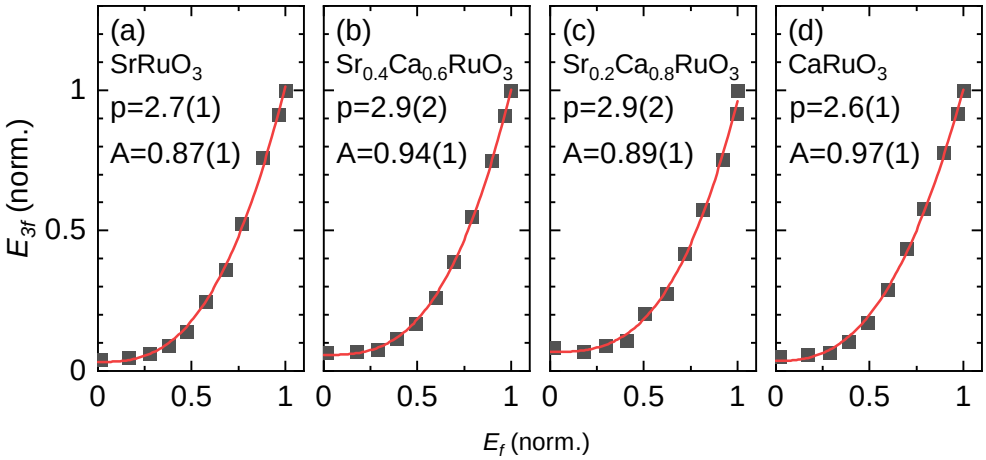

Figure 2.7: Fluence dependence of the third-harmonic generation of (a) $SrRuO_3$, (b) $Sr_{0.4}Ca_{0.6}RuO_3$, (c) $Sr_{0.2}Ca_{0.8}RuO_3$, and (d) $CaRuO_3$. The measurements were performed at 5 K with 0.7 THz as a driving pulse. All curves are fitted with $E_{3f} = AE_f^p + E_0$.

before the sample and another at 2.1 THz placed after the sample. Lastly, an additional wire grid polarizer is positioned behind the sample to ensure that the measured polarization is well defined. For each data point, two measurements are performed: one with only the 0.7 THz filter in place and another with both filters in place. The field E_f is determined from experiments with only the 0.7 THz bandpass filter, integrating over the spectral region from 0.5 to 0.9 THz. To determine E_{3f} both bandpass filters are used, and the integration is over the spectral region from 1.9 to 2.3 THz.

Figures 2.7 (a)-(d) show the fluence dependences of the nonlinear signal at 5 K and 0.7 THz as a driving pulse. For all samples a clear nonlinear dependence of E_{3f} on E_f is observed. To extract this dependence a power law with $E_{3f} = AE_f^p + E_0$ is fitted to the data sets. E_0 represents the value measured at 3f frequency when the polarizers were rotated with 90 ° to each other, and corresponds to the noise floor of the experiment. The power law, instead of a linear combination of a linear and cubic function, was chosen because the temperature dependence (discussed later) excludes a linear contribution. In this case the extracted powers p are 2.7(1), 2.9(2), 2.9(2), and 2.6(1) for $SrRuO_3$,

$Sr_{0.4}Ca_{0.6}RuO_3$, $Sr_{0.2}Ca_{0.8}RuO_3$, and $CaRuO_3$, respectively. Although, within their uncertainties these values overlap with each other, there appears to be a difference between the pure and mixed compounds. $SrRuO_3$ and $CaRuO_3$ deviate from the expected $p = 3$ dependence for a perturbative effect while the mixed compounds could be reasonably explained with $p = 3$.

There are three possible explanations for this phenomena in $SrRuO_3$ and $CaRuO_3$. Firstly, there could be an additional linear contribution coming from leakage of the broadband THz pulse through the first THz bandpass filter at the third harmonic frequency of 2.1 THz. This would explain the apparent deviation from the perturbative regime by reducing the overall power. However, the problem with this interpretation is, that the detected leakage of the fundamental needs to have a similar contribution in every fluence dependence, since the extracted powers are comparable. This is difficult to believe because of the strong difference in the transmission properties observed in Fig 2.5 at the fundamental frequency. Furthermore, the transmission for the fundamental frequency is the highest in the mixed compounds. This would lead to the strongest deviation from perturbative behavior for these samples, which is not observed in these measurements.

Additionally, the temperature-dependent spectra can be compared to investigate the influence of leakage (a more detailed discussion of the temperature dependence is provided in the next section). Based on the overall metallic behavior of the samples shown in Fig. 2.5 and on measurements reported in the literature [20], it can be inferred that the transmission at 2.1 THz should be higher at 300 K than at 5 K. Therefore, if leakage of the pump pulse at 3f frequencies were a significant factor, it would be most prominent in the 300 K measurements. However, as shown in Fig. 2.12 in the appendix, for the three highest temperatures, there is no visible signal in either $SrRuO_3$ or $CaRuO_3$, ruling out this possibility as an explanation. Furthermore, leakage of the fundamental through the second bandpass filter can be excluded because for the E_{3f} measurement it is not in the correct frequency range and for the measurement of E_f the second filter is not in place.

The second possible interpretation would be a saturation effect reducing

the power for the highest fluence and therefore reducing the overall power. This is unlikely again because of the difference in transmission properties drastically changing the effective field inside the sample for the 4 samples. Furthermore, fitting the data until 75 % maximum field strength shows the same power dependence as a fit over the whole data range.

The last possible interpretation is, that the process of third-harmonic generation is non-perturbative and has a characteristic power law dependence of $p = 2.5$. This would align with our previous THG fluence measurements on $CaRuO_3$ shown in Fig. 2.2 (e) showing a power of $p = 2.6$. Notable here is that this measurement was performed with a driving field of 0.5 THz and the THG at 1.5 THz, were a relatively large spectral density of the broadband THz pulse is available, and a residual can be detected at 300 K seen in Fig. 2.3 (b). However, the matching power law to these measurements at 0.7 THz drive is notable and could be a sign of a specific underlying physical process. Similar to the $p = 2.5$ scaling found in the Dirac semi-metal Cd_3As_2 [25], graphite and graphene before saturation [59] possibly signifying the presence of linear dispersion.

Temperature Dependence

The next step is to investigate and compare the temperature dependence of the four different compounds. Figure 2.8 (a) shows E_{3f} as a function of temperature allowing for a comparison of the absolute nonlinear emission. $CaRuO_3$ shows the largest emission of third-harmonic followed by $SrRuO_3$ and $Sr_{0.4}Ca_{0.6}RuO_3$, $Sr_{0.2}Ca_{0.8}RuO_3$ emits the least amount of radiation at 5 K. Overall the temperature dependences behave similar, the THG starts to be observable below 100 K and increases towards lower temperatures, comparable to our measurements in section 2.2. This can be emphasized by the normalized curves shown in Fig. 2.8 (b). Within the accuracy of the measurement all four measurement series overlap with each other, indicating a common physical origin for the nonlinear response.

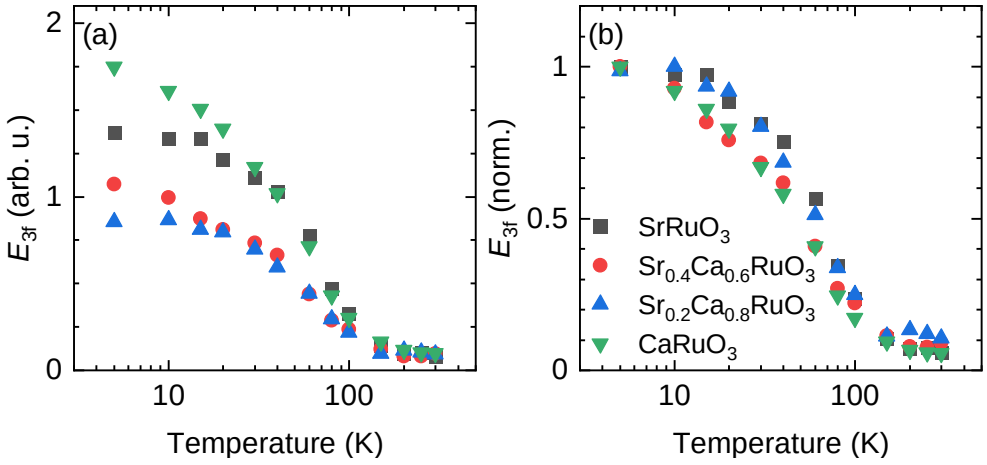

Figure 2.8: Temperature dependence of the emitted third harmonic E_{3f}. (a) E_{3f} for the four 20 nm samples. (b) E_{3f} for the four 20 nm samples normalized to its peak value.

One important consideration is that the emitted third harmonic radiation scales with the effective driving field inside the sample. To minimize the dependence of the measured signal on the sample conductivity, it is beneficial to extract the nonlinear susceptibility $|\chi^{(3)}| \propto E_{3f}/E_f^3$. Figure 2.9 (a) shows $|\chi^{(3)}|$ as a function of temperature for the all 20 nm samples. It is noticeable, that $SrRuO_3$ has a $|\chi^{(3)}|$ an order of magnitude larger then the other samples. This is due to the fact that even though the emitted third harmonic generation is in the same order of magnitude as the other samples (Fig. 2.8 (a)), the effective field inside the sample is smaller, due to the relatively high conductivity of $SrRuO_3$.

To investigate the temperature scaling between the samples it is insightful to normalize $|\chi^{(3)}|$ to its maximum value. Figure 2.9 (b) shows the normalized curves and, similar to Fig. 2.8 (b), within our measurement accuracy all measurements show the same scaling behavior. $|\chi^{(3)}|$ gets large enough to be measured below 100 K and increases continuously to lower temperatures. The increase appears to be exponential in nature with the data points scaling linearly on the logarithmic temperature scale. Therefore, as a phenomenological first step a fit with $|\chi^{(3)}| = Ae^{-(T-T_0)/T_1}$ can be performed.

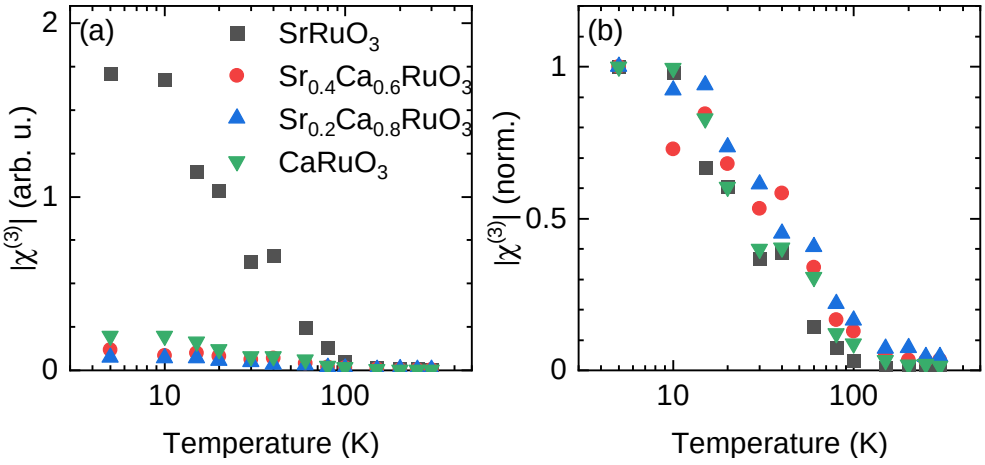

Figure 2.9: Temperature dependence of the nonlinear susceptibility $|\chi^{(3)}|$. (a) $|\chi^{(3)}|$ for the four 20 nm samples. (b) $|\chi^{(3)}|$ for the four 20 nm samples normalized to its peak value.

Setting $A = 1$ and $T_0 = 5$ K results in $T_1 = 41(3)$ K as the single fitting parameter (see Fig. 2.10). In an analogue to pump-probe experiments this would represent a "decay temperature", a characteristic temperature/energy scale of the underlying process. This would correspond to a thermal energy of $\epsilon_{\text{Therm.}} = 41\,\text{K} \cdot k_B = 3.5\,\text{meV}$. Remarkably, this energy is close to the reported energy of the Weyl nodes relative to the Fermi energy in $SrRuO_3$ of 8.5 mV [15] indicating a possible connection between the third-harmonic generation and the presence of linear dispersion. This in combination with the fluence scaling $E_f^{2.6}$ for the pure compounds could be indications that the nonlinear response stems from linear dispersion. Showing that, not only is the transport in $SrRuO_3$ influenced by Weyl fermions, but the whole series $Sr_{1-x}Ca_xRuO_3$ could be influenced by them.

Going into a more detailed analysis of the temperature dependence, the occupation of states close to the Fermi energy can be considered. This is done by using the Fermi-Dirac distribution:

$$F(\epsilon, T) = \frac{1}{e^{\frac{\epsilon-\mu_0}{k_B T}} + 1}, \tag{2.6}$$

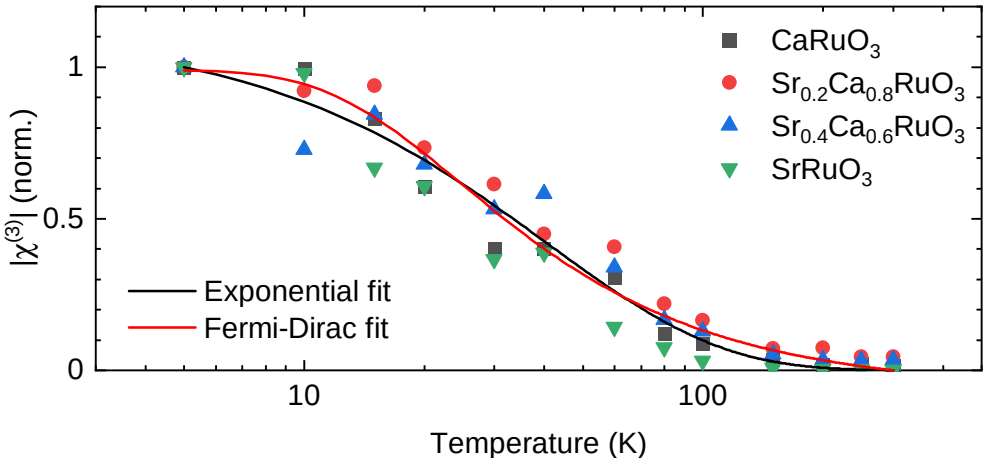

Figure 2.10: Fits of the temperature dependence of $|\chi^{(3)}|$. The exponential and Fermi-Dirac fits are shown as an average of the fits to the individual samples.

with μ_0 the chemical potential, k_B the Boltzmann constant, T the temperature, and ϵ the energy. The interesting observable to consider is the change in occupation at a certain energy and starting temperature T_0 as a function of temperature leading to

$$\Delta F = F(\epsilon, T) - F(\epsilon, T_0). \tag{2.7}$$

Choosing $\mu_0 = 0.5$ meV, $T_0 = 300$ K and normalizing ΔF leaves ϵ the only variable. To fit ΔF to the normalized $|\chi^{(3)}|$ data, an additional scaling factor A_0, with no physical significance, is introduced. Fitting equation 2.7 to $|\chi^{(3)}|$ (see Fig. 2.10) of the four samples gives an average $\epsilon - \mu_0 = -3.3$ meV. This suggests that the state responsible for the third harmonic generation is located 3.3 meV below the Fermi energy, matching the characteristic energy scale extracted with the exponential fit. The two known candidates are the coherent heavy quasiparticles at low temperatures known in $CaRuO_3$ [24] and the Weyl points in $SrRuO_3$ [15].

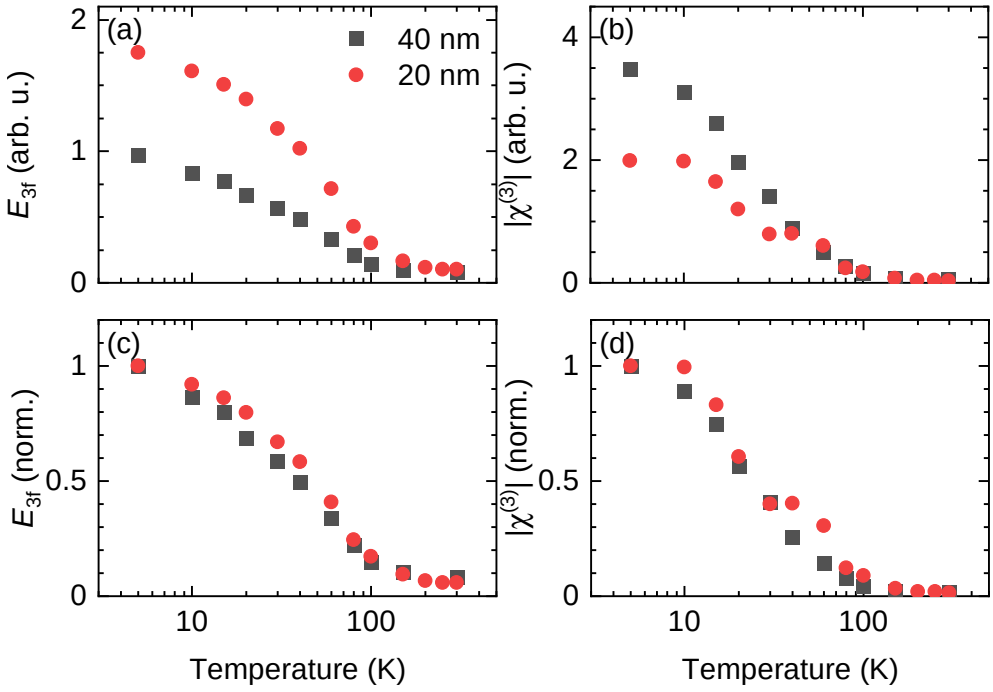

Figure 2.11: Temperature dependence of E_{3f} and $|\chi^{(3)}|$ for two different thicknesses of $CaRuO_3$ thin films.

Thickness Dependence

The last step is to investigate the temperature dependence in samples with different thicknesses. First, this is to exclude the reason for this non-linearity to be heating. Second, if the temperature scaling is characteristic it should not depend on the sample thickness. Figure 2.11 (a) shows the emitted third-harmonic E_{3f} as a function of temperature for two $CaRuO_3$ thin films with thicknesses of 20 nm and 40 nm. For both samples the response starts to be measurable at 100 K, however the nonlinear response of the 20 nm sample shows a stronger increase and is roughly 2 times larger at 5 K. There are two mechanisms at play here, the reduced thickness leading to less absorption of the emitted third harmonic inside the sample, while there is halve as much sample available for generation of radiation. In this case the reduced absorption seems to be the dominating contribution. $|\chi^{(3)}|$ (shown in Fig. 2.11 (b))

as a material parameter should be the same for both samples, however they clearly start to differ below 30 K. The possible reason for this might be sample quality changing the low temperature conducting properties. Furthermore, the influence of strain differs for samples of different thickness, influencing and changing sample properties.

The normalized curves for E_{3f} and $|\chi^{(3)}|$ are shown in Fig. 2.11 (c) and (d). For both curves, within the measurement accuracy, they lay on top of each other. This behavior is expected for two samples of the same material. However, the fact that the 40 nm sample scales similarly to the 20 nm sample suggests that it also follows the characteristic scaling observed in other compounds with a thickness of 20 nm, further indicating a common scaling behavior within this group of compounds.

2.3.3 Conclusion

In summary, the linear and nonlinear THz response of four different chemical compositions of $Sr_{1-x}Ca_xRuO_3$ were investigated. The fluence dependence shows a power law for the third harmonic of $p = 2.6$ deviating from the perturbative expectation in the pure compounds and indicating the underlying mechanism possibly facilitating some sort of characteristic scaling behavior. This is corroborated by the fact that all temperature dependences (independent of the samples conducting properties) show identical scaling. These results show the underlying mechanism of THG in the four compositions to be a common one. The closest equivalent for the observed fluence scaling is found in materials with known linear dispersion [25, 59], which would match the recent discovery of Weyl fermions in $SrRuO_3$ thin films [15]. This could mean all investigated samples show signs of linear dispersion with an extracted energy scale of 3.5 meV matching the predicted position of the Weyl nodes in $SrRuO_3$ [15]. However, the measured temperature dependence of the flat band in $CaRuO_3$ [24] matches our experimental data and therefore making it a possible explanation for the temperature scaling. Furthermore, the Fermi-Dirac fit indicates the energy position

of the state of origin to be close to the Fermi energy, as is the heavy quasiparticle peak in $CaRuO_3$ [24]. This would mean that all investigated samples show strong frequency dependent scattering facilitating the nonlinear response. While for $CaRuO_3$ and $SrRuO_3$ this is a known phenomena in the THz frequency range, for the mixed compounds the disorder induced scattering screens this effect from being observable with conventional linear spectroscopy [18–23]. Unfortunately, there are no nonlinear THz measurements on other flat band/heavy quasiparticle materials leaving no comparison for the fluence dependence. Without a microscopic theory of the low temperature ground state in $Sr_{1-x}Ca_xRuO_3$ or an extensive study incorporating ARPES, magneto-transport, and harmonic generation spectroscopy it is, at the moment, not possible to distinguish between these two possibilities. Furthermore, if the THz third harmonic generation stems from frequency-dependent scattering, additional effects could also be an explanation. [23]. However, this study shows that even in samples with high degree of disorder, THG could be a powerful tool to probe and investigate materials with strong low energy electronic correlations.

2.3.4 Appendix

Temperature Dependence of the Spectra

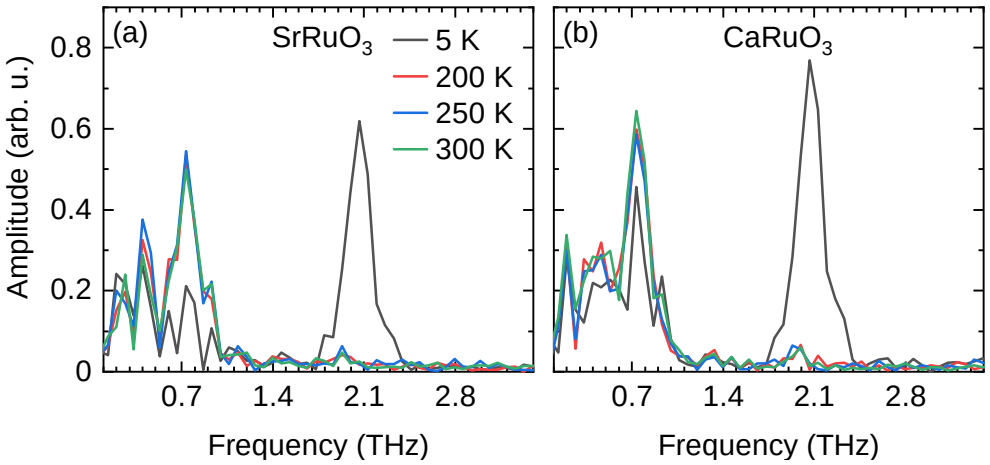

Figure 2.12: Fourier spectra of the nonlinear response for (a) $SrRuO_3$ and (b) $CaRuO_3$ at different temperatures.

Figure 2.12 (a) and (b) show the Fourier spectra measured with the f and 3f filters in place at different temperatures for $SrRuO_3$ and $CaRuO_3$. For $SrRuO_3$ at 5 K, there is a significant signal centered at 2.1 THz, corresponding to the third harmonic generation (THG). However, at the highest temperatures, no signal is visible at this frequency. In the case of $CaRuO_3$, it could be argued that there is a potential signal at 1.9 THz at the highest temperatures, but it is on the order of the noise. Given that the signal-to-noise ratio (SNR) is approximately 1 and that the signal does not change magnitude with temperature (as would be expected for a linear contribution from the residual pump pulse), it is considered to be noise.

The α parameter

Since the simulation and experimental values are ultimately normalized for comparison, the absolute value of α is not critical. What is important is that α in the simulation captures the temperature-dependent scaling of the

frequency-dependent scattering time observed in the linear spectroscopy measurements. To achieve this, certain assumptions can be made. First, as reported by Schneider et al. in Physical Review Letters **112**, 206403 (2014), electrons driven by different frequencies exhibit different scattering times. For electrons in a metal, this implies that they are driven to a distribution around the energy $\epsilon = \epsilon_f + \epsilon_\nu$, where ϵ_f is the Fermi energy and ϵ_ν is the energy of the photon.

For simplicity, let's consider a single electron excited to exactly ϵ. This energy can be related to a momentum p via the electron's dispersion relation, $\epsilon(p)$. If we assume that, within the Boltzmann transport model, the electric field varies slowly enough for the electron to reach this momentum p, we can establish a valid equivalence. However, this is not universally the case, and an exact mapping of the energy of the excited state to the electron's momentum is not required for the model, at least not to encapsulate the temperature dependence. Since the temperature scaling is the crucial factor, the energy dependence of the excited state at each temperature can be mapped to momentum space without needing absolute values. The method used to derive the formula for scattering time in the simulation is explained in the following paragraphs.

To employ the described time-dependent Boltzmann transport model, a formula for $\tau(p)$ and values that encapsulate the strength of the momentum dependence is required. The first step to achieve this involves extracting the frequency dependence as reported by Schneider et al. in PRL **112**, 206403 (2014). For this purpose, two possible plots can be considered: Fig. 4(c), which shows $\sigma_1 \propto \tau$, and Fig. 4(d), which depicts $\rho_1 \propto \Gamma \propto \frac{1}{\tau}$. Each plot has its own advantages and disadvantages. Fig. 4(c) offers the advantage of high point density but is limited by the inclusion of only a few temperatures. Fig. 4(d), on the other hand, has a lower point density but includes the complete temperature range. For this work, the data from Fig. 4(d) was chosen because the extracted parameter is essential for describing the measured temperature dependence.

As a first step, the data from Fig. 4(d) is replotted as $\frac{1}{\rho_1} \propto \tau$ as a function

of frequency ν for all temperatures. Given that this replotting results in only four points per temperature, a linear fit is employed to extract the slope α as a function of frequency:

$$\tau(\nu) = \alpha\nu + \tau_0. \tag{2.8}$$

It should be noted that this description is a simplification of reality. Fig. 4(c) demonstrates that a linear description is not accurate for the lowest temperatures. Within a Fermi-liquid framework, a power law description would provide a more accurate representation [13]. However, introducing the additional fit parameter required by a power law description is questionable due to the limited number of data points available for fitting. Furthermore, the model employed is phenomenological, lacking a microscopic or qualitative description, and is used to qualitatively describe the observed nonlinear response.

In the model, a free electron description with a simple parabolic band is employed, characterized by the dispersion relation [4]:

$$\epsilon(p) = \frac{\hbar^2 p^2}{2m}. \tag{2.9}$$

As discussed before this is based on the simplified assumption that the electric field drives the electrons to the energy corresponding to the energy of the excited state with the driving frequency. With this assumption in mind, one can express $\tau(\nu) = \alpha\nu + \tau_0$ as $\tau(\epsilon) = \alpha\frac{\epsilon}{h} + \tau_0$, where h is Planck's constant, and then substitute the dispersion relation:

$$\tau(p) = \tau_0 \left(\alpha \frac{\hbar^2 p^2}{2m\tau_0} + 1 \right). \tag{2.10}$$

One final consideration is that the units of α and τ_0 are not explicitly defined, since in the extraction process, $\frac{1}{\rho_1} \propto \tau$ was used. Therefore, all constants are

combined into a new term, α', reducing equation 2.10 to:

$$\tau(p) = \tau_0 \left(\alpha' p^2 + 1\right). \tag{2.11}$$

The value of τ_0 is taken from Schneider et al., Physical Review Letters **112**, 206403 (2014). Additionally, α' is proportional to the extracted α from Schneider et al., and the product $\alpha' p^2$ cannot be less than 1, as this would result in a negative scattering time. Since the simulation is performed within the first two Brillouin zones, with $p \in [-2\pi/a, 2\pi/a]$, where a is the lattice constant, we require that $\alpha' < a/2\pi$. The advantage here is that the maximum value of the extracted α is -0.65, and the minimum is -0.04. Therefore, by setting $\alpha' = \alpha \cdot a/2\pi$, all the necessary conditions are satisfied and we do not need to introduce additional scaling to the extracted α.

References

1. Reinhoffer, C. *et al.* Strong Terahertz Third-Harmonic Generation by Kinetic Heavy Quasiparticles in $CaRuO_3$. *Physical Review Letters* **132,** 196501 (2024).
2. Wang, Y. L. *et al.* High stability of electro-transport and magnetism against the A-site cation disorder in $SrRuO_3$. *Scientific Reports* **6,** 27840 (2016).
3. Cuffini, S. L., Guevara, J. A. & Mascarenhas, Y. P. Structural Analysis of Polycrystalline $CaRuO_3$ and $SrRuO_3$ Ceramics from Room Temperature Up to 1273 K. *Materials Science Forum* **228-231,** 789–794 (1996).
4. Dang, H. T. *et al.* Electronic correlations, magnetism, and Hund's rule coupling in the ruthenium perovskites $SrRuO_3$ and $CaRuO_3$. *Physical Review B* **91,** 195149 (2015).
5. Mazin, I. I. & Singh, D. J. Electronic structure and magnetism in Ru-based perovskites. *Physical Review B* **56,** 2556–2571 (1997).
6. Schneider, M., Moshnyaga, V. & Gegenwart, P. Ferromagnetic quantum phase transition in $Sr_{1-x}Ca_xRuO_3$ thin films. *physica status solidi (b)* **247,** 577–579 (2010).
7. Khalifah, P. *et al.* Evolution of transport and magnetic properties near the ferromagnetic quantum critical point in the series $Ca_xSr_{1-x}RuO_3$. *Physical Review B* **70,** 134426 (2004).
8. Tripathi, S. *et al.* Ferromagnetic $CaRuO_3$. *Scientific Reports* **4,** 3877 (2014).
9. He, T. & Cava, R. J. Disorder-induced ferromagnetism in $CaRuO_3$. *Physical Review B* **63,** 172403 (2001).

10. Shen, S. *et al.* Emergent Ferromagnetism with Fermi-Liquid Behavior in Proton Intercalated $CaRuO_3$. *Physical Review X* **11,** 021018 (2021).

11. Koster, G. *et al.* Structure, physical properties, and applications of $SrRuO_3$ thin films. *Reviews of Modern Physics* **84,** 253–298 (2012).

12. Stewart, G. R. Non-Fermi-liquid behavior in d- and f-electron metals. *Reviews of Modern Physics* **73,** 797–855 (2001).

13. Schofield, A. J. Non-Fermi liquids. *Contemporary Physics* **40,** 95–115 (1999).

14. Klein, L. *et al.* Possible non-Fermi-liquid behavior of $CaRuO_3$. *Physical Review B* **60,** 1448–1451 (1999).

15. Takiguchi, K. *et al.* Quantum transport evidence of Weyl fermions in an epitaxial ferromagnetic oxide. *Nature Communications* **11,** 4969 (2020).

16. Kar, U. *et al.* The thickness dependence of quantum oscillations in ferromagnetic Weyl metal $SrRuO_3$. *npj Quantum Materials* **8,** 1–10 (2023).

17. Kostic, P. *et al.* Non-Fermi-Liquid Behavior of $SrRuO_3$: Evidence from Infrared Conductivity. *Physical Review Letters* **81,** 2498–2501 (Sept. 21, 1998).

18. Dodge, J. S. *et al.* Low-Frequency Crossover of the Fractional Power-Law Conductivity in $SrRuO_3$. *Physical Review Letters* **85,** 4932–4935 (2000).

19. Kamal, S. *et al.* Terahertz-frequency carrier dynamics and spectral weight redistribution in the nearly magnetic metal $CaRuO_3$. *Physical Review B* **74,** 165115 (2006).

20. Schneider, M. *et al.* Low-Energy Electronic Properties of Clean $CaRuO_3$: Elusive Landau Quasiparticles. *Physical Review Letters* **112,** 206403 (2014).

21. Geiger, D. *et al.* Terahertz conductivity of $Sr_{1-x}Ca_xRuO_3$. *Physical Review B* **93,** 165131 (2016).

22. Kumar, K. S. *et al.* Terahertz Electrodynamics in Transition Metal Oxides. *Advanced Optical Materials* **8,** 1900958 (2020).

23. Wang, Y. *et al.* Separated transport relaxation scales and interband scattering in thin films of $SrRuO_3$, $CaRuO_3$, and Sr_2RuO_4. *Physical Review B* **103,** 205109 (2021).

24. Liu, Y. *et al.* Revealing the hidden heavy Fermi liquid in $CaRuO_3$. *Physical Review B* **98,** 041110 (2018).

25. Kovalev, S. *et al.* Non-perturbative terahertz high-harmonic generation in the three-dimensional Dirac semimetal Cd_3As_2. *Nature Communications* **11,** 2451 (2020).

26. Germanskiy, S. *et al.* Ellipticity control of terahertz high-harmonic generation in a Dirac semimetal. *Physical Review B* **106,** L081127 (2022).

27. Coleman, P. & Schofield, A. J. Quantum criticality. *Nature* **433,** 226–229 (2005).

28. Löhneysen, H. v. *et al.* Fermi-liquid instabilities at magnetic quantum phase transitions. *Reviews of Modern Physics* **79,** 1015–1075 (2007).

29. Gegenwart, P., Si, Q. & Steglich, F. Quantum criticality in heavy-fermion metals. *Nature Physics* **4,** 186–197 (2008).

30. Berthod, C. *et al.* Non-Drude universal scaling laws for the optical response of local Fermi liquids. *Physical Review B* **87,** 115109 (2013).

31. Dang, H. T. *et al.* Band Structure and Terahertz Optical Conductivity of Transition Metal Oxides: Theory and Application to $CaRuO_3$. *Physical Review Letters* **115,** 107003 (2015).

32. Cao, G. *et al.* Non-Fermi-liquid behavior in single-crystal $CaRuO_3$: Comparison to ferromagnetic $SrRuO_3$. *Solid State Communications* **148,** 305–309 (2008).

33. Lee, Y. S. *et al.* Non-Fermi liquid behavior and scaling of the low-frequency suppression in the optical conductivity spectra of $CaRuO_3$. *Physical Review B* **66,** 041104 (2002).

34. Rondinelli, J. M. *et al.* Electronic properties of bulk and thin film $SrRuO_3$: Search for the metal-insulator transition. *Physical Review B* **78,** 155107 (2008).

35. Zhu, L. *et al.* Universally Diverging Grüneisen Parameter and the Magnetocaloric Effect Close to Quantum Critical Points. *Physical Review Letters* **91,** 066404 (2003).

36. Damle, K. & Sachdev, S. Nonzero-temperature transport near quantum critical points. *Physical Review B* **56,** 8714–8733 (1997).

37. Šmakov, J. & Sørensen, E. Universal Scaling of the Conductivity at the Superfluid-Insulator Phase Transition. *Physical Review Letters* **95,** 180603 (2005).

38. Witczak-Krempa, W. *et al.* Universal transport near a quantum critical Mott transition in two dimensions. *Physical Review B* **86,** 245102 (2012).

39. Lucas, A. *et al.* Dynamical Response near Quantum Critical Points. *Physical Review Letters* **118,** 056601 (2017).

40. Dalidovich, D. & Phillips, P. Nonlinear Transport near a Quantum Phase Transition in Two Dimensions. *Physical Review Letters* **93,** 027004 (2004).

41. Green, A. G. & Sondhi, S. L. Nonlinear Quantum Critical Transport and the Schwinger Mechanism for a Superfluid-Mott-Insulator Transition of Bosons. *Physical Review Letters* **95,** 267001 (2005).

42. Oka, T. & Aoki, H. Ground-State Decay Rate for the Zener Breakdown in Band and Mott Insulators. *Physical Review Letters* **95,** 137601 (2005).

43. Mitra, A. *et al.* Nonequilibrium Quantum Criticality in Open Electronic Systems. *Physical Review Letters* **97,** 236808 (2006).

44. Hogan, P. M. & Green, A. G. Universal nonlinear conductivity close to an itinerant-electron quantum critical point. *Physical Review B* **78,** 195104 (2008).

45. Shao, C. *et al.* High-Harmonic Generation Approaching the Quantum Critical Point of Strongly Correlated Systems. *Physical Review Letters* **128,** 047401 (2022).

46. Esser, S. *et al.* Nonlinear conductivity in $CaRuO_3$ thin films measured by short current pulses. *The European Physical Journal B* **87,** 133 (2014).

47. Murakami, Y. *et al.* Anomalous Temperature Dependence of High- Harmonic Generation in Mott Insulators. *Physical Review Letters* **129,** 157401 (2022).

48. Uchida, K. *et al.* High-Order Harmonic Generation and Its Unconventional Scaling Law in the Mott-Insulating Ca_2RuO_4. *Physical Review Letters* **128,** 127401 (2022).

49. Hirori, H. *et al.* Single-cycle terahertz pulses with amplitudes exceeding 1 MV/cm generated by optical rectification in $LiNbO_3$. *Applied Physics Letters* **98,** 091106 (2011).

50. Hebling, J. *et al.* Velocity matching by pulse front tilting for large-area THz-pulse generation. *Optics Express* **10,** 1161–1166 (2002).

51. Wu, Q. & Zhang, X. Free-space electro-optic sampling of terahertz beams. *Applied Physics Letters* **67,** 3523–3525 (1995).

52. Mravlje, J. *et al.* Coherence-Incoherence Crossover and the Mass- Renormalization Puzzles in Sr_2RuO_4. *Physical Review Letters* **106,** 096401 (2011).

53. Shen, K. M. *et al.* Evolution of the Fermi Surface and Quasiparticle Renormalization through a van Hove Singularity in $Sr_{2-y}La_yRuO_4$. *Physical Review Letters* **99,** 187001 (2007).

54. Dantas, R. M. A. *et al.* Nonperturbative topological current in Weyl and Dirac semimetals in laser fields. *Physical Review B* **103,** L201105 (2021).

55. Aoki, H. *et al.* Nonequilibrium dynamical mean-field theory and its applications. *field theory* **86** (2014).

56. Prochaska, L. *et al.* Singular charge fluctuations at a magnetic quantum critical point. *Science* **367,** 285–288 (2020).

57. Yang, C.-J. *et al.* Critical slowing down near a magnetic quantum phase transition with fermionic breakdown. *Nature Physics* **19,** 1605–1610 (2023).

58. Schraknepper, H. *et al.* Pulsed laser deposition of $SrRuO_3$ thin-films: The role of the pulse repetition rate. *APL Materials* **4,** 126109 (2016).

59. Arshad, A. *et al.* Terahertz Harmonic Generation from Graphite Pencil Drawings. *Advanced Photonics Research* **4,** 2300088 (2023).

3 Harmonic Generation in the BCS Superconductor MgB_2

3.1 Introduction

The main content of this chapter is the publication "Reinhoffer et al. High-Order Nonlinear Terahertz Probing of the Two-Band Superconductor MgB_2: Third- and Fifth-Order Harmonic Generation. *Physical Review B* **106**, 214514 (2022)" [1], investigating the nonlinear response of the Bardeen - Cooper - Schrieffer (BCS) superconductor MgB_2 in an applied magnetic field. To better understand the wider context of this publication, it is helpful to introduce the physical principles and sample investigated in these measurements. For this purpose, this section will first introduce the Higgs mode, an amplitude oscillation in the superconducting ground state, as it is the main driving mechanism behind the nonlinear response investigated in this study [1]. After which, MgB_2 is going to be introduced which is known to be the BCS superconductor with the highest critical temperature at ambient pressures, and the work that has been done to understand its properties.

3.1.1 Higgs Mode

The existence of a Higgs mode in superconductors has been a topic ever since the microscopic description of the superconducting ground state existed [2]. The well-known Higgs mode in particle physics, although experimentally confirmed first [3, 4], was theoretically predicted after the Higgs mode in superconductors [2]. While the discovery of the Higgs mode in particle physics in 2012 is widely celebrated and accepted [5], the experimental confirmation of the Higgs mode in superconductors is still a actively debated topic [6, 7]. One of the problems in observing the Higgs mode is that it does not have an electric charge, magnetic moment, and other quantum numbers, resulting in nonlinear coupling being the only possibility to access the Higgs mode [8].

The mathematical description of the Higgs mode, can and been done in multiple ways [8]. Here a phenomenological description is chosen, therefore the Ginzburg-Landau theory is a reasonable starting point. The order parameter for the superconducting ground state is chosen to be $\psi(\mathbf{r})$ as a complex function. It can be interpreted as the cooper pair density, i.e., $n_c(\mathbf{r}) = |\psi(\mathbf{r})|^2$ [9]. Accordingly the free-energy density of a superconductor can be expressed as a power expansion:

$$f(\psi) = f_0 + a|\psi(\mathbf{r})|^2 + \frac{b}{2}|\psi(\mathbf{r})|^4, \tag{3.1}$$

with $a = a_0(T - T_c)$ and $b > 0$ [9]. This free energy potential in the case of $T < T_c$ is shown in Fig.3.1 (a) denoted as t_0 projected on the real part of $\psi(\mathbf{r})$. To ensure that $\psi(\mathbf{r})$ is a slowly varying an additional term is added taking into account that the order parameter is a function of the whole superconductor [9]:

$$f(\psi) = f_0 + a|\psi(\mathbf{r})|^2 + \frac{b}{2}|\psi(\mathbf{r})|^4 + \frac{\hbar}{2m^*}|\nabla\psi(\mathbf{r})|^2, \tag{3.2}$$

with m^* the effective mass of the cooper pair. Lastly, in an applied electric- or magnetic field, $f(\psi)$ should be independent of the vector potential chosen. This requirement leads to the time-dependent Ginzburg-Landau equation of

the free-energy density [9]:

$$f(\psi) = f_0 + a|\psi(\mathbf{r})|^2 + \frac{b}{2}|\psi(\mathbf{r})|^4 + \frac{1}{2m^*}|(-i\nabla - e^*\mathbf{A})\psi(\mathbf{r})|^2, \qquad (3.3)$$

with e^* the effective charge of the cooper pairs and $\mathbf{A}$ is a vector potential connected to the external field $\mathbf{E}(t) = -\partial\mathbf{A}(t)/\partial t$ [8, 9].

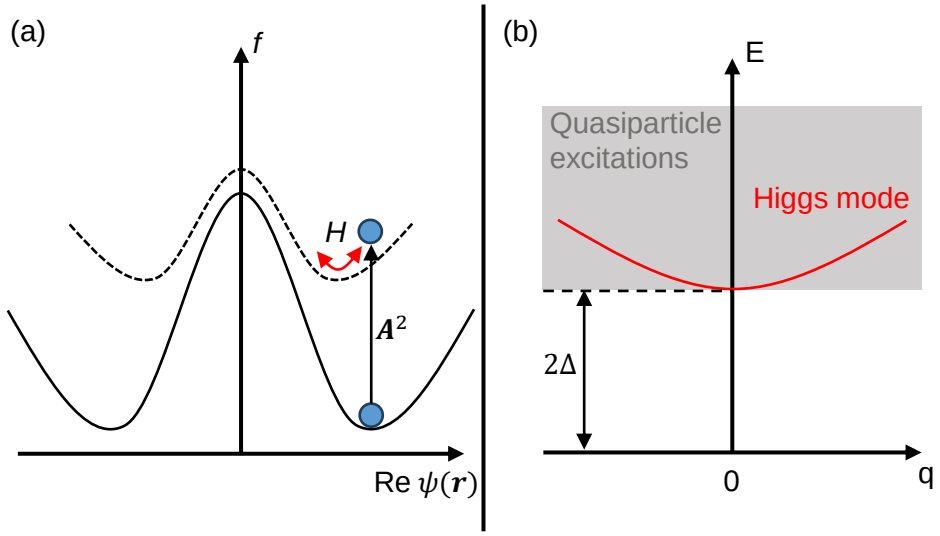

Figure 3.1: Higgs mode. (a) Free energy potential of the superconducting ground state ψ before a THz quench (solid) and after THz quench (dashed). The quench leads to the collective oscillation of the superconducting condensate (Higgs mode) [10]. (b) Dispersion of the Higgs mode, with the energy gap at the Γ-point 2Δ [8].

Equation 3.3 as a description of the superconducting ground state is sufficient to capture many of the observed phenomena in superconductors [9]. To investigate possible excitations, the wave function can be expanded in a perturbative way with $\psi(\mathbf{r}) = (\psi_0 + H(\mathbf{r}))e^{i\theta(\mathbf{r})}$ [8]. Here $H(\mathbf{r})$, and $\theta(\mathbf{r})$ represent an amplitude, and a phase component of fluctuation of the order-parameter, respectively. These two fluctuations are called Higgs mode (amplitude) and Nambu-Goldstone mode (phase) [8]. Using this perturbation and applying a unitary gauge $\mathbf{A}' = \mathbf{A} - \nabla\theta/e^*$, the GL potential up to the second order

fluctuation becomes [8]:

$$f = -2aH^2 + \frac{1}{2m^*}(\nabla H)^2 + \frac{e^{*2}\psi_0^2}{2m^*}\mathbf{A}^2 + \frac{e^{*2}\psi_0}{m^*}\mathbf{A}^2 H + ... \tag{3.4}$$

Here two interesting observations can be made: First, the term $-2aH^2$ shows that there is an energy gap for the amplitude (Higgs) mode that has to be overcome. Second, the first term where the electromagnetic field $\mathbf{A}$ interacts with the Higgs mode H is $\frac{e^{*2}\psi_0}{m^*}\mathbf{A}^2 H$ showing the coupling to be nonlinear [8]. Figure 3.1 (a) shows the excitation mechanism as a process similar to two photon absorption. Two photons combine and quench the superconducting order, changing the free energy landscape. The oscillation of the amplitude (Higgs mode) is a result of this new excited state. Figure 3.1 (b) shows a schematic of the dispersion of the Higgs mode. At its lowest point the Higgs mode has the energy of the superconducting gap [8]. However, the Cooper pairs condense with the same energy of 2Δ resulting in quasiparticle excitations playing a role in the excited state [8].

Even though the Higgs mode is accessible by nonlinear coupling between it and electromagnetic waves there needs to be an observable to detect this process. One possible observable is the generated superconducting current $\mathbf{j}$ defined as [8]:

$$\mathbf{j} = -\frac{\partial F}{\partial \mathbf{A}} = -\frac{ie^*}{2m^*}(\psi^\dagger \nabla\psi - \nabla\psi^\dagger\psi) - \frac{e^{*2}}{m^*}\mathbf{A}\psi^\dagger\psi, \tag{3.5}$$

with $\psi^\dagger$ being the complex conjugate of ψ. Here again it is possible to take a perturbative approach $\psi(\mathbf{r}) = (\psi_0 + H(\mathbf{r}))e^{i\theta(\mathbf{r})}$ and collect terms including the Higgs mode H,

$$\mathbf{j} = -\frac{2e^{*2}\psi_0}{m^*}\mathbf{A}H. \tag{3.6}$$

Having two oscillatory functions present results in frequency mixing terms similar to section 1.1.2. Assuming the driving field to be oscillating with the

frequency ω, it is known from the $\mathbf{A}^2H$-term that the Higgs mode is oscillating with 2ω. Therefore, the term $\mathbf{A}H$ results in a current oscillating at 3ω emitting electromagnetic radiation at the same frequency, resulting in the third harmonic generation [7, 8]. The energy gap of superconductors 2Δ is in the order of few meVs making THz harmonic generation a good method to investigate the Higgs mode [7].

Beside the Higgs mode, there can be other contributions to the nonlinear response of a superconductor, with the most obvious one being the breaking of Cooper pairs [8]. In recent years, there has been an ongoing debate within the scientific community about which process has the largest contribution to the third-harmonic generation (THG) in superconductors [8, 11]. While there is agreement that the Higgs mode is a subdominant contribution in the clean limit of superconductivity, no consensus has been reached for the dirty limit [11]. This ongoing investigation highlights the complexity of understanding nonlinear phenomena in superconductors and underscores the need for further experimental and theoretical studies to clarify these mechanisms.

3.1.2 MgB_2

The superconductivity of MgB_2 was discovered in 2001 [13], which is relatively late considering that, as a metallic compound, it is readily available and easy to fabricate [14]. Electron-phonon coupling was found to be the driving mechanism behind the superconducting transition, making MgB_2 the BCS superconductor with the highest critical temperature at ambient pressures up to $T_c \approx 40$ K [14]. Another intriguing property of MgB_2 is that the superconductivity needs to be described by a two band superconductivity model [15], arising from the crystal structure influencing the electronic properties [14, 16]. Figure 3.2 (a) shows the crystal structure of MgB_2, consisting of layers of magnesium on a hexagonal lattice separated by layers of boron forming a honeycomb lattice [16]. The bands forming the superconducting bands are the p-orbitals from the boron. In the plane the p_x and p_y orbitals hybridize and form the p_{xy}-orbital responsible for forming two σ metallic bands and

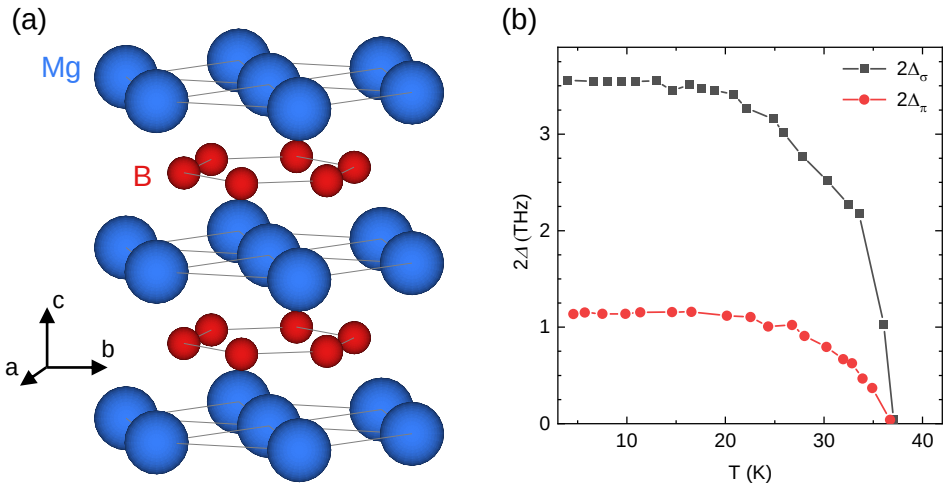

Figure 3.2: Properties of MgB_2. (a) Crystal structure of MgB_2 consisting out of honeycomb boron layers (red) separated by magnesium (blue) layers created using VESTA [12]. (b) Temperature dependence of the two superconducting gaps measured with STM adapted from data in [7].

the p_z-orbitals form the two metallic π-bands [14, 16]. The charges in the σ-bands couple to the in-plane phonons of the boron lattice, mediating the superconducting transition [14]. The π-bands are coupled to the σ-band resulting in the superconductivity appearing at the same critical temperature for both bands [14]. Figure 3.2 (b) shows the energy of the superconducting gap for both bands as a function of temperature adapted from data in [7]. The superconducting gap is larger for the σ-band than for the π-band which is in line with what would be expected for a band that mediates the superconductivity in the other band [7, 14].

This data has been published as part of a letter in Physical Review B [7]. The plot is a reformatted version of the original data as published. Reprinted with permission from Sergey Kovalev, Tao Dog, Li-Yu Shi, Chris Reinhoffer, Tie-Quan Xu, Hong-Zhang Wang, Yue Wang, Zi-Zhao Gan, Semyon Germanskiy, Jan-Christoph Deinert, Igor Ilyakov, Paul H. M. van Loosdrecht, Dong Wu, Nan-Lin Wang, Jure Demsar, and Zhe Wang *Physical Review B* **104**, L140505 (2021). Copyright 2021 by the American Physical Society.

The first measurement of the THz optical conductivity of MgB_2 was conducted by Kaindl et al. at the end of 2001, only a few months after the discovery of its superconducting properties [17]. Figure 3.3 (a) shows THz transmission spectroscopy data for select temperatures normalized to the transmission at 36 K. After crossing the superconducting transition (in the sample measured at 36 K) the transmission characteristics of the sample change. For frequencies below the superconducting gap the transmission decreases, in line with the expectation that electromagnetic radiation decreases exponentially within a superconductor [4, 18], while the transmission above the superconducting gap increases. This can be understood looking at the the extracted optical conductivity data in Figure 3.3 (b). The real part of the optical conductivity σ_1, representing the absorption inside the sample, is smaller for all frequencies in the superconducting state compared to the normal conducting state. This can be explained by the fact that the pair braking excitation above the bandgap energy has a smaller cross-section than the quasiparticle scattering in the normal conducting state. Furthermore inside the bandgap there are no excitations possible at low temperature leading to a strong suppression of σ_1 below the bandgap. However, the superconducting state screens radiation and the penetration depth of radiation (scaling inversely with the imaginary conductivity σ_2) leads to the decrease in transmission below the superconducting gap [4, 17, 18].

The fact that MgB_2 has a band which can be in the dirty limit of superconductivity and that the superconducting gap is in the order of 1 THz [14] made it a perfect candidate material to investigate the Higgs mode [7]. As discussed in section 3.1.1, the coupling between light and the Higgs mode should exhibit a resonance when $2\omega = 2\Delta$ and could more efficient in the dirty limit of superconductivity [8]. Therefore, using third harmonic generation as a probe would result in a maximum of the generated intensity when the resonance condition is fulfilled [7, 8]. Figure 3.3 (c) shows the results of this experiment performed by Kovalev et al. in 2021 [7]. By changing the THz driving frequencies and tuning the temperature of the sample, they were able to tune the system in and out of the resonance condition. This enabled them

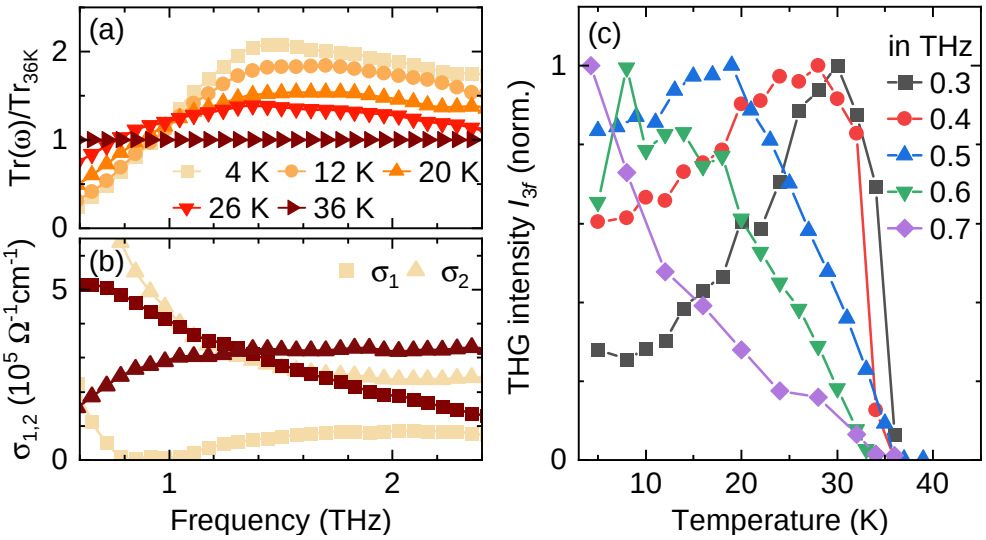

Figure 3.3: Linear and nonlinear THz response of MgB_2, data adapted from [7]. (a) THz transmission of MgB_2 at different temperatures normalized to the transmission at 36 K. (b) Real and imaginary part of the optical conductivity of MgB_2 for 4 K and 36 K. (c) THz third harmonic generation as a function of temperature for different THz driving frequencies.

to show that the THG emission does, in fact, exhibit a maximum when the resonance condition $2\omega = 2\Delta$ is met [7]. Furthermore, they observed no resonance with the superconducting band in the clean limit and demonstrated that the THG is polarization independent, which further supports their claim that the observed THG results from the nonlinear coupling of light to the Higgs mode [7].

This data has been published as part of a letter in Physical Review B [7]. The plot is a reformatted version of the original data as published. Reprinted with permission from Sergey Kovalev, Tao Dog, Li-Yu Shi, Chris Reinhoffer, Tie-Quan Xu, Hong-Zhang Wang, Yue Wang, Zi-Zhao Gan, Semyon Germanskiy, Jan-Christoph Deinert, Igor Ilyakov, Paul H. M. van Loosdrecht, Dong Wu, Nan-Lin Wang, Jure Demsar, and Zhe Wang *Physical Review B* **104**, L140505 (2021). Copyright 2021 by the American Physical Society.

Based on these experimental findings the aim is to advance the understanding of the nonlinear coupling of light to the Higgs mode. For that purpose, an experiment was designed which not only allowed the previous findings to be reproduced by being able to tune the frequency of the light via filters and the superconducting gap via temperature; the setup was able to measure up to the fifth harmonic generation and could tune the superconducting gap by applying a strong external magnetic field up to 10 T.

3.2 High-Order Nonlinear Terahertz Probing of the Two-Band Superconductor MgB_2: Third- and Fifth-Order Harmonic Generation

3.2.1 Introduction

High-harmonic spectroscopy has been demonstrated to be very powerful in revealing novel properties of matter, especially by providing time-resolved dynamical characteristics for states far from thermodynamic equilibrium [19–50]. From these high-order nonlinear characteristics one can realize dynamical Bloch oscillations [21–23, 27], reconstruct electronic band structures [24, 25, 37], and identify topological and relativistic effects [26, 29–33, 51]. For a more complex system with strong electron-electron interactions, high-harmonic generation opens up new opportunities to disclose fingerprints for exotic states of matter, such as amplitude (Higgs) modes [8, 52], stripe phases in cuprates [46], light- or current-driven symmetry breaking phases [47, 53, 54], and light-induced phase transitions in strongly correlated systems [38, 44]. Moreover, ellipticity dependence of high-harmonic generation allows to probe magnetic dichroism [55, 56] and molecular chirality on a sub-picosecond time scale [57].

Recent developments on accelerator-based intense and high-repetition-rate terahertz source have enabled high-harmonic spectroscopic studies in the few terahertz-frequency range (1 THz $\sim$ 4.1 meV) with femtosecond time resolution [28, 29, 48, 58]. In this work we use the terahertz (THz) high-harmonic spectroscopy to investigate characteristic nonlinear response of the representative two-band superconductor MgB_2.

This section has been published as a article in Physical Review B [1]. The following is a reformatted version of the original paper as published. Reprinted with permission from C. Reinhoffer, P. Pilch, A. Reinold, P. Derendorf, S. Kovalev, J.-C. Deinert, I. Ilyakov, A. Ponomaryov, Min Chen, Tie-Quan Xu, Yue Wang, Zi-Zhao Gan, De-Sheng Wu, Jian-Lin Luo, S. Germanskiy, E. A. Mashkovich, P. H. M. van Loosdrecht, I. M. Eremin, and Zhe Wang *Physical Review B* **106**, 214514 (2022).

With a layered crystalline structure, MgB_2 consists of boron atoms forming a primitive honeycomb lattice and magnesium atoms located above the center of the boron hexagons in-between the boron planes [13]. The Fermi surface in MgB_2 is characterized by a two-dimensional σ-band (bonding $p_{x,y}$ bands) and a three-dimensional π-band (bonding and antibonding p_z bands) [59]. Below a superconducting transition at about 40 K, two superconducting energy gaps open simultaneously in the σ- and π-bands with $2\Delta_\sigma = 13 - 14$ and $2\Delta_\pi = 3 - 5$ meV, respectively, at the lowest temperatures [60–62]. With a stronger intraband scattering the π band is in the dirty limit [63–65], whereas the σ band with a smaller scattering than $2\Delta_\sigma$ is intermediately clean (see e.g. [7, 65]). As a type-II superconductor MgB_2 maintains a Meissner phase up to a lower critical field $H_{c1} \sim 0.1$ T (see e.g. [66]), while the upper critical field H_{c2} exhibits evident anisotropy with respect to magnetic field orientation (see e.g. [67, 68]). Moreover, the resistive superconducting transitions are not sharp in applied magnetic fields, which may reflect metastability of the vortex system around H_{c2} [67, 68]. In resistivity measurements for $H \parallel c$ the onset of superconductivity determines $H_{c2}^{\text{onset}} = 7.0 - 7.5$ T, while the zero resistivity occurs at $H_{c2}^{\text{zero}} = 3.0 - 3.5$ T for the lowest temperatures (see e.g. [67, 68] and Appendix Fig. 3.8). Ordered vortex-lattice phases were resolved well below H_{c2}^{zero} [69]. For $H \parallel ab$ the upper critical field extends up to above 20 T [67, 68].

With a relatively high T_c and a representative two-band nature, MgB_2 as a model system has been vividly investigated by various pump-probe spectroscopic techniques (see e.g. [6, 7, 70–73]). For example, nonequilibrium dynamics of optically excited carriers was studied by optical reflection probe [70] or THz probe [71] with sub-ps time resolution, in which the important role of electron-phonon couplings has been revealed. A white-light probe of the optically excited transient states disclosed fingerprint for interband scattering between the σ- and π-bands [72], and found a particular E_{2g} phonon mode which interacts strongly with the σ-bands [72, 73]. More recently, THz field driven nonequilibrium states of MgB_2 was investigated by

THz probe [6] or by harmonic generation [7], which provided possible evidence for Leggett mode or Higgs mode, respectively. Since these experiments were performed for different frequencies and waveforms of pump pulses, a more systematic study remains necessary to clarify the involved nonequilibrium dynamics [74].

Following our previous work on temperature dependence of THz third-harmonic generation in MgB_2 in zero magnetic field [7], here we carry out studies of THz third-harmonic generation in applied external magnetic fields and also observe fifth-order harmonic generation as a function of temperature. These investigations provide a more systematic characterization of the THz nonlinear response of the superconducting state in MgB_2.

3.2.2 Experimental Details

High-quality single-crystalline MgB_2 thin films with the *c*-axis epitaxy and a thickness of 10 nm were grown on 5×5 mm MgO (111) substrate by using a hybrid physical-chemical vapor deposition method, and characterized by x-ray diffraction and charge transport measurements [75]. Magnetic field dependence of *dc* resistivity was measured with a current of 100 μA at various temperatures for applied fields parallel to the *c*-axis, using a physical properties measurement system (PPMS-9T, Quantum Design).

The THz harmonic generation measurements were performed at the TELBE user facility in the Hemholtz Zentrum Dresden-Rossendorf. Intense narrow-band THz pulses were generated based on a linear electron accelerator which was operated at 50 kHz and synchronized with an external femtosecond laser system [58]. The THz radiation was detected by electro-optic sampling in a ZnTe crystal using the synchronized laser system. Bandpass filters with central frequencies of a bandwidth of 20 % were applied to produce narrow-band THz radiation of desired frequencies. The bandwidth here is defined as a full-width at the half-maximum of transmission, which corresponds to +-10 % of the central frequency. Well beyond the central frequency the transmission is suppressed by about 30 dB. The experiment was aligned

in a transmission geometry. The emitted harmonic radiation was detected after the sample in the direction of the normally incident THz beam. For the excitation and detection of high-harmonic generation, f-, $3f$- and $5f$-bandpass filters with central frequencies of $f = 0.3$, $3f = 1$, $f = 0.4$ and $5f = 2.1$ THz were used. Magnetic field dependent measurements were carried out in a cryomagnet (Oxford Instruments) with the magnetic field applied along the *c*-axis of the MgB_2 thin films, the same orientation as for the *dc* resistance measurements.

Since the MgB_2 samples degrade in air, we sealed a fresh piece of sample under vacuum before the user experiment. During the experiment the sample was installed in an evacuated cryostat. The spectroscopic data presented here was acquired for a continuous 84 hours experiment. The transport data were obtained on a different piece of sample.

3.2.3 Experimental Results and Discussion

Experimental Results

We start with reproducing the previously reported third-harmonic generation [7], since we are now using a different THz source i.e. based on an electron accelerator and measuring a different piece of sample. Under the drive of a 0.3 THz excitation pulse with peak electric field of 13 kV/cm, the electric field of emitted radiation from MgB_2 was recorded in time-domain, which for 28 K below T_c is presented in Fig. 3.4(a). In addition to the major peaks (as marked by the circles) that correspond to the driving pulse, one can clearly see two additional peaks [see arrows in Fig. 3.4(a)] between every two neighbouring major peaks. This is a direct observation of third-harmonic radiation from the superconducting state of MgB_2 on sub-picosecond time scale. By performing Fourier transformation of the time-domain signal, the obtained spectrum exhibits two sharp peaks at $f = 0.3$ THz and $3f = 0.9$ THz, respectively [Fig. 3.4(b)]. We note that the time-domain signal is measured through a $3f$-bandpass filter, which suppresses the f components substantially, leading to the apparent larger amplitude at $3f$ in Fig. 3.4(b).

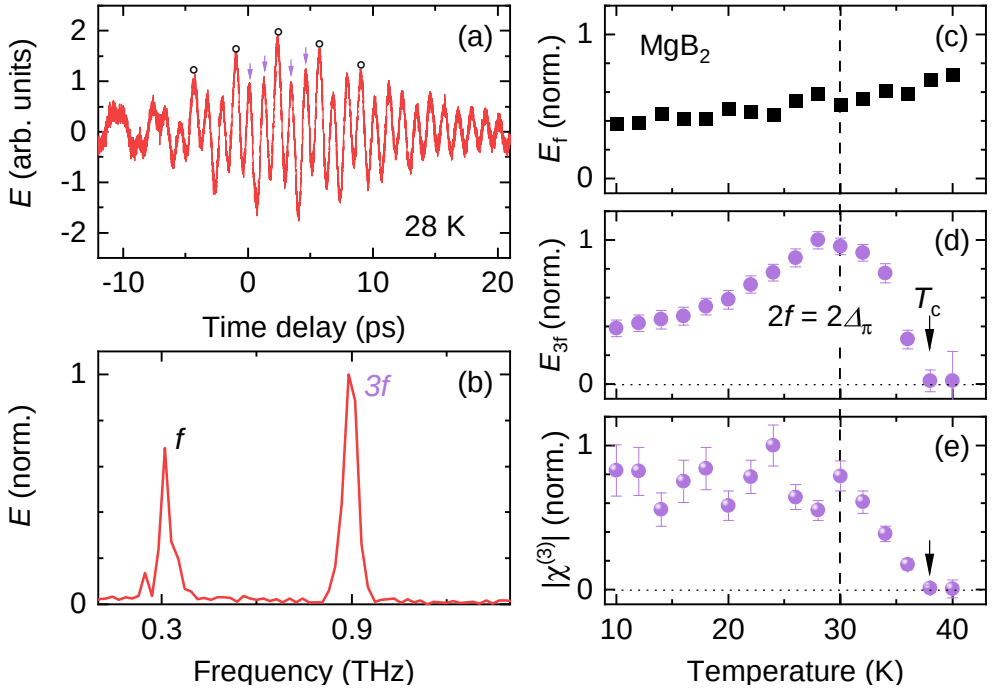

Figure 3.4: (a) Emitted THz electric field from MgB_2 driven by a $f = 0.3$ THz pulse at 28 K and in zero magnetic field. The data is recorded through a $3f$-bandpass filter with a central frequency of 1 THz. The arrows indicate the $3f$ signal. (b) Fourier spectrum of the time-domain signal in (a) exhibits third-harmonic radiation at $3f = 0.9$ THz. (c) f- and (d) $3f$-components of the emitted electric field as a function of temperature. (e) $|\chi^{(3)}| \equiv E_{3f}/E_f^3$ versus temperature. The dashed line indicates the temperature with the resonance condition $2f = 2\Delta_\pi$ fulfilled.

The amplitude of the f and $3f$ components (E_f and E_{3f}) as derived from Fig. 3.4(b) is presented in Fig. 3.4(c) and Fig. 3.4(d), respectively, as a function of temperature. While the monotonic decrease of E_f with reduced temperature reflects increased screening in the superconducting phase [7, 17, 65, 76–79], the third-harmonic radiation E_{3f} exhibits a broad maximum around 30 K. Above T_c the third-harmonic yield is essentially zero, whereas dramatically enhanced below the superconducting transition. Below 30 K, E_{3f} starts to drop again with decreasing temperature. Such a decrease might have simply resulted from the enhanced reflection of the driving field well below T_c,

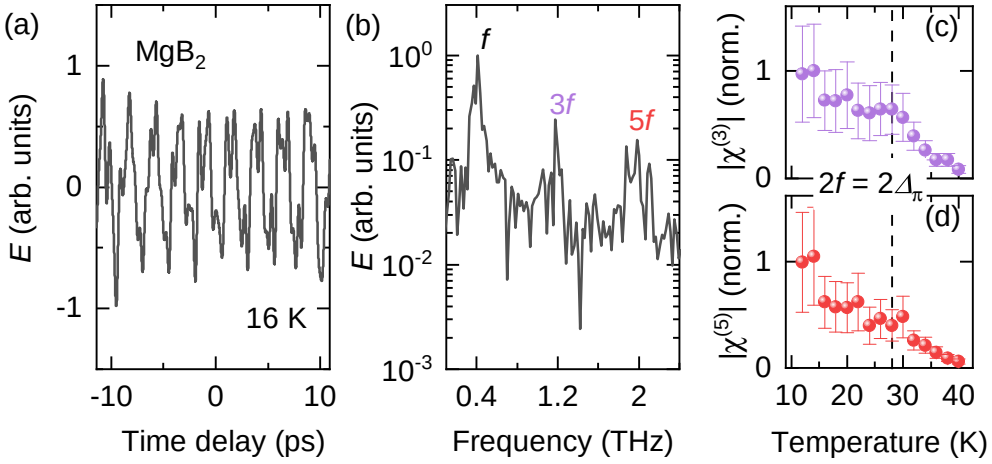

Figure 3.5: (a) Terahertz electric field emitted from MgB_2 driven by a $f = 0.4$ THz pulse at 16 K in zero field. (b) The corresponding spectrum exhibits fundamental f, third $3f$, and fifth $5f$ harmonic generation. A $5f$-bandpass filter with a central frequency of 2.1 THz was applied for the detection. Temperature dependence of (c) third- and (d) fifth-order nonlinear susceptibility, $|\chi^{(3)}| \equiv E_{3f}/E_f^3$ and $|\chi^{(5)}| \equiv E_{5f}/E_f^5$, respectively. Dashed line indicates the temperature corresponding to the resonance condition $2f = 2\Delta_\pi$.

since the third-order response should be more sensitive to the screening of the driving field. However, this cannot fully explain the observed maximum in the temperature dependence curve. We evaluate temperature dependence of a third-order susceptibility $|\chi^{(3)}|$ via normalized E_{3f}/E_f^3, as presented in Fig. 3.4(e). With decreasing temperature from T_c, $|\chi^{(3)}|$ increases monotonically until 30 K, while at lower temperatures $|\chi^{(3)}|$ levels off. At 30 K, the resonance condition $2f = 2\Delta_\pi$ is fulfilled [61], i.e. twice the pump frequency equals the superconducting energy gap in the π band. Hence, the observed temperature dependence of the third-harmonic generation reflects the nonlinear response of the superconductivity, rather than just being a consequence of the enhanced screening of the driving field.

High-harmonic radiation even up to the fifth order is observed from the superconducting state of MgB_2 under a drive of 0.4 THz pulse with a peak electric field of 60 kV/cm, which can be seen directly from the time-resolved

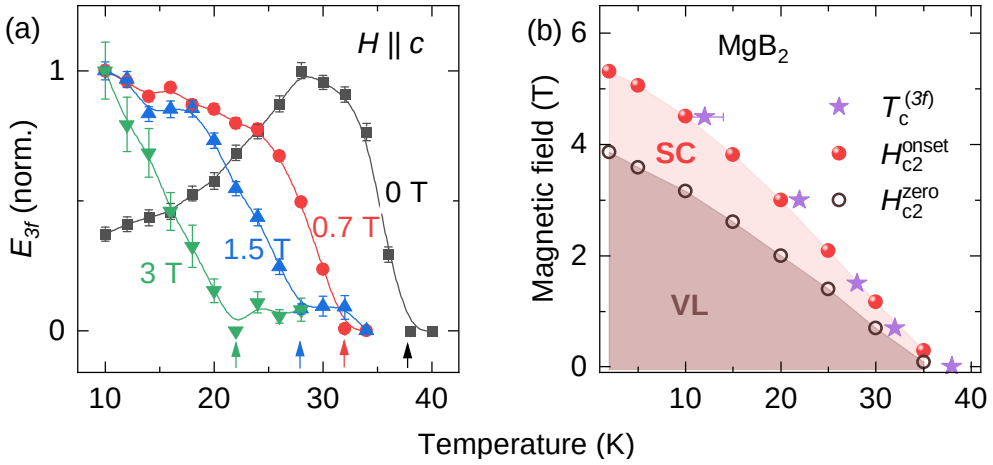

Figure 3.6: (a) THG amplitude E_{3f} as a function of temperature in various applied magnetic fields $H \parallel c$. The arrows indicate the THG onset temperature $T_c^{(3f)}$. (b) Magnetic field-temperature phase diagram of MgB_2. H_{c2}^{zero} corresponds to zero resistance (see Appendix Fig. 3.8), below which ordered vortex-lattice (VL) phase is formed [69]. H_{c2}^{onset} are the fields where the resistance starts to drop (see Appendix Fig. 3.8). The field-dependent $T_c^{(3f)}(H)$, in agreement with $H_{c2}^{\text{onset}}(T)$, determines the superconducting (SC) phase boundary.

electric field of the radiation [Fig. 3.5(a)]. This is more evident in its Fourier spectrum [Fig. 3.5(b)], which displays clearly the fundamental, third-, and fifth-harmonic components. The absence of even-order harmonics is dictated by the existence of an inversion symmetry in the crystal structure of MgB_2 with a space group of *P6/mmm* [13, 80]. Here we have employed a $5f$-bandpass filter to enable a simultaneous detection of the different components, from which we can estimate the temperature dependence of the nonlinear susceptibilities, as presented in Fig. 3.5(c) and Fig. 3.5(d) for normalized $|\chi^{(3)}| \equiv E_{3f}/E_f^3$ and $|\chi^{(5)}| \equiv E_{5f}/E_f^5$, respectively. Finite values of the nonlinear susceptibilities appear below T_c, characterizing nonlinear response of the superconducting state. With decreasing temperature an initial rapid increase of $|\chi^{(3)}|$ and $|\chi^{(5)}|$ is followed by a gentle one below about 28 K or rather level-off behaviour towards the lowest temperature. As indicated by

the dashed line in Fig. 3.5(c)(d), this temperature corresponds to the same resonance condition, $2f = 2\Delta_\pi$, for $f = 0.4$ THz and the π-band gap $2\Delta_\pi$ [61]. We note that neither the $3f$ nor the $5f$ signals observed here are just leakage of the pump pulse through the bandpass filters, otherwise they should appear also well above the superconducting transition with even higher intensity because of reduced screening of the pump pulse.

As presented above, the high-order nonlinear probe is very sensitive to the superconductivity of MgB_2. Hence we can utilize the third-harmonic generation to study the nonlinear response of the superconducting state in an applied magnetic field. Figure 3.6(a) displays the electric-field amplitude of emitted third-harmonic radiation versus temperature for $f = 0.3$ THz in various magnetic fields along the c-axis ($H \parallel c$). With increasing field from 0 T, the onset of the third-harmonic generation shifts continuously towards lower temperature [see arrows in Fig. 3.6(a)]. Moreover, the resonance-peak feature observed in zero field is replaced in finite fields by a monotonic increase of the third-harmonic generation with decreasing temperature. Since the high-harmonic radiation reflects time-dependent spatial average of the nonlinear current over a mm beam spot size, the absence of a resonance feature may result from spatial inhomogeneity and metastability of the vortex system, besides the suppression of superconductivity in fields.

The onset temperature of the third-harmonic generation as a function of the applied magnetic field $T_c^{(3f)}(H)$ is shown in Fig. 3.6(b), and compared with the temperature dependence of characteristic fields $H_{c2}^{\mathrm{zero}}(T)$ and $H_{c2}^{\mathrm{onset}}(T)$, which corresponds to the occurrence of zero resistance and the field where the resistance starts to drop, respectively (see Appendix Fig. 3.8). One can see that $T_c^{(3f)}(H)$ matches very well with $H_{c2}^{\mathrm{onset}}(T)$ rather than $H_{c2}^{\mathrm{zero}}(T)$. Thus, the THz nonlinear response provides a sensitive probe of the superconducting stiffness in the applied magnetic fields. While below H_{c2}^{zero} ordered vortex lattice is formed [64], the finite resistance between H_{c2}^{zero} and H_{c2}^{onset} probably results from vortex motion under excitation of electric current [67, 68].

Discussion

Third-order harmonic generation in MgB_2 thin films has been reported previously for the GHz frequencies (see e.g. [81–85]). These low-energy responses are not only sensitive to intrinsic properties of the superconductor which can be ascribed to backflow of thermally excited unpaired quasiparticles in the presence of the superflow [86, 87], but also to extrinsic properties e.g. weak links or vortex motion [81–85, 88]. In particular, the backflow of the unpaired quasiparticle is responsible for the observed GHz harmonic response mainly around T_c. In contrast to these previous studies, our present work focuses on the nonlinear response in the THz frequencies, whose photon energy is comparable to the superconducting gaps of this system at low temperatures and about three orders of magnitude higher than the microwaves. Moreover, the THz pulses with intense electric field drive the system out of equilibrium, thus the observed nonlinearity reflects the high-energy nonequilibrium properties of the superconductor.

On the origin of the THz high-harmonic generation in conventional superconductors there is an ongoing discussion at present. In fact in a BCS-type single-band superconductor it was found that the activation of the Higgs mode is not the only process which can be probe through the high-harmonic generation. In particular, the Bogoliubov quasiparticles give further contribution to the high-harmonic generation at 2Δ, as it coincides with the onset of the particle-hole continuum corresponding to the energy needed to break the Cooper pairs. It was shown in Ref. [35] that in the clean BCS single-band superconductor the charge-density-fluctuation contribution, associated with Bogoliubov quasipartciles, to the third-harmonic generation current is three orders of magnitude larger than that from the Higgs mode. Subsequent studies analyzed how impurities affect this ratio, and the current consensus is that amplitude (Higgs) fluctuations contribution may dominate the THG signal at sufficient disorder [41, 42, 89–91].

Very recently the analysis for the third-order harmonic generation has been expanded to a two-band model [74]. The main conclusion of this study

was that the third-order harmonic signal at a lower gap will be still dominated by the contribution of charge density fluctuations even if one accounts for the disorder, included in a semi-phenomenological way. To see whether this is really the case one would be required to use a quasiclassical Green's functions formalism, which goes well beyond the present mostly experimental work. Instead, in what follows we outline the framework of calculating the fifth-harmonic generation current in a clean case using a pseudospin formalism.

The Heisenberg equations of motion for the pseudospins $\vec{\sigma}_k$ are given by

$$\partial_t \vec{\sigma}_k(t) = i[\hat{H}, \vec{\sigma}_k] = \vec{b}_k \times \vec{\sigma}_k(t) \tag{3.7}$$

where the Hamiltonian $\hat{H} = \sum_k \vec{b}_k \vec{\sigma}_k$ with the pseudomagnetic field $\vec{b}_k$. We calculate the time evolution of the pseudospins up to the fourth order in the vector potential $A(t)$ by expanding the z component of $\vec{b}_k$ in the nonlinear response regime

$$\epsilon_{k-eA(t)} + \epsilon_{k+eA(t)} = 2\epsilon_k + \epsilon_k^{A^2} + \frac{1}{12}\epsilon_k^{A^4} + O(A^6) \tag{3.8}$$

with ϵ_k representing the dispersion relation,

$$\epsilon_k^{A^2} = \sum_{i,j=\{x,y\}} e^2 A_i(t) A_j(t) \partial_{k_i} \partial_{k_j} \epsilon_k,$$

and

$$\epsilon_k^{A^4} = \sum_{i,j,l,m=\{x,y\}} e^4 A_i(t) A_j(t) A_l(t) A_m(t) \partial_{k_i} \partial_{k_j} \partial_{k_l} \partial_{k_m} \epsilon_k.$$

Restricting the analysis to a BCS-type single-band superconductor in the clean limit (see Appendix), we find that either due to Higgs amplitude fluctuations or Cooper-pair breaking (charge density fluctuations), third-order harmonic yield exhibits a resonance enhancement for a resonance condition $2f = 2\Delta$, whereas enhanced fifth-order harmonic generation occurs at two resonance conditions $4f = 2\Delta$ and $2f = 2\Delta$ (see Appendix Fig. 3.7). In the clean limit, the fifth-harmonic generation is primarily due to the Cooper-pair

breaking, similar to previous theoretical analysis for third-harmonic generation (see e.g. [6, 35, 40]). In contrast, in the dirty limit the third-harmonic generation could be dominated by Higgs amplitude fluctuations (see e.g. [41, 42]). As for the amplitude fluctuations, the resonance condition $2f = 2\Delta$ indicates a resonant excitation of a Higgs mode through two photons, which is coupled to another one or three photons, leading to the third- or fifth-harmonic generation, respectively. Corresponding to the resonance condition $4f = 2\Delta$, a Higgs mode can also be resonantly excited through four photons, resulting in the fifth-harmonic generation.

An important experimental finding here is that a resonance feature in the third- and fifth-harmonic generation [Fig. 3.5(c)(d)] is observed only for $2f = 2\Delta_\pi$ corresponding to the π-band gap in the dirty limit, although for the clean-limit σ-band gap the resonance conditions $2f = 2\Delta_\sigma$ and $4f = 2\Delta_\sigma$ should be experimentally accessible. These results do not support an interpretation of the observed high-harmonic generation in MgB_2 as being predominantly due to pair-breaking of the clean-limit band, but rather suggests that Higgs amplitude fluctuations in the dirty-limit band mainly lead to the high-harmonic signals. Nonetheless, this argument assumes negligible interband couplings, and is essentially based on an independent band picture. A rigorous analysis of a two-band model by taking into account interband couplings and sufficient disorder is still required to elucidate the different contributions, not only for the third-order harmonic generation, but also for high-order harmonic generation as observed here.

3.2.4 Conclusion

By performing terahertz high-order harmonic spectroscopy of the superconducting state in the two-band superconductor MgB_2, we revealed characteristic nonlinear response of the superconductivity. As a function of temperature and applied magnetic field, we investigated third- and fifth-order harmonic generation in MgB_2 driven by intense terahertz field, and established its superconducting phase diagram. Resonance enhancement of the third- and the

fifth-harmonic signals in zero field was observed only for the dirty-limit π-band, i.e. $2f = 2\Delta_\pi$, below the superconducting transition temperature, but not for $2f = 2\Delta_\sigma$ or $4f = 2\Delta_\sigma$ of the clean-limit σ-band. While in a single-band picture this suggests a dominant contribution of the Higgs amplitude fluctuations to the high-harmonic generation in the dirty limit, the analysis of a more realistic two-band model for MgB_2 by taking into account the interband couplings and disorder is still necessary for a more reliable interpretation of our experimental results.

Acknowledgments We thank L. Benfatto, T. Dahm, M. Eskildsen, J. Fiore, and J. Kierfeld for very helpful discussions. The work in Cologne was partially supported by the DFG via Project No. 277146847 — Collaborative Research Center 1238: Control and Dynamics of Quantum Materials (Subproject No. B05). Parts of this research were carried out at ELBE at the Helmholtz-Zentrum Dresden - Rossendorf e.V., a member of the Helmholtz Association. We acknowledge partial support by MERCUR (Mercator Research Center Ruhr) via Project No. Ko-2021-0027.

3.2.5 Appendix

Pseudospin Analysis

To understand the signatures of the superconducting state and its collective modes in the fifth-harmonic generation (FHG) we follow the standard approach of using the Anderson pseudospin outlined in [92], which is defined as:

$$\vec{\sigma}_k = \frac{1}{2}\Psi_k^\dagger \vec{\tau} \Psi_k \tag{3.9}$$

Here, $\vec{\tau}$ denotes the Pauli-matrices vector and $\Psi_k = \begin{pmatrix} \hat{c}_{k\uparrow} & \hat{c}_{-k\downarrow} \end{pmatrix}^T$ is the Nambu-Gorkov spinor. The BCS Hamiltonian can be written in the compact form

$$\hat{H}_{BCS} = \sum_k \vec{b}_k \vec{\sigma}_k \tag{3.10}$$

with the pseudomagnetic-field $\vec{b}_k = 2\begin{pmatrix} -\Delta' & \Delta'' & \epsilon_k \end{pmatrix}^T$, where $\Delta = \Delta' + i\Delta''$. The gap equation can also be expressed via pseudospins

$$\Delta = V \sum_k \left(\langle \hat{\sigma}_k^x \rangle + i \langle \hat{\sigma}_k^y \rangle \right)$$

where $\hat{\sigma}_k^{x,y}$ denote the component of the pseudospin vector. In the following we restrict our analysis here to a single gap in the clean limit.

To calculate the third- and fifth-order nonlinear currents, we first compute the gap-oscillation under irradiation whose vector potential is given by $A(t) = A_0 \sin(\Omega t)$ with $\Omega = 2\pi f$ the angular frequency. We include the coupling of the electronic system to the electromagnetic field via a Peierls-substitution, which affects the z-component of the pseudomagnetic-field

$$\vec{b}_k = \begin{pmatrix} -2\Delta' & 2\Delta'' & \epsilon_{k+eA} + \epsilon_{k-eA} \end{pmatrix}^T. \tag{3.11}$$

The time-evolution of the pseudospins obeys the Heisenberg equations of motion

$$\partial_t \vec{\sigma}_k(t) = i \left[\hat{H}, \vec{\sigma}_k \right] = \vec{b}_k \times \vec{\sigma}_k(t) \tag{3.12}$$

Following the standard procedure we linearize the equations by expressing $\vec{\sigma}_k(t) = \langle \vec{\sigma}_k(0) \rangle + \delta\vec{\sigma}_k(t)$ and $\Delta(t) = \Delta + \delta\Delta(t)$ and decouple the resulting system of differential equation by transforming Eq. (3.12) to Laplace-space. We further set Δ to be real at $t = 0$ which allows to express the equilibrium's values for the pseudospin components

$$\begin{aligned} \langle \hat{\sigma}_k^x(0) \rangle &= \frac{\Delta}{2E_k} \tanh\left(\frac{E_k}{2k_B T} \right) \\ \langle \hat{\sigma}_k^y(0) \rangle &= 0 \\ \langle \hat{\sigma}_k^z(0) \rangle &= \frac{-\epsilon_k}{2E_k} \tanh\left(\frac{E_k}{2k_B T} \right), \end{aligned} \tag{3.13}$$

where $E_k = \sqrt{\epsilon_k^2 + \Delta^2}$ is the Bogoliubov energy dispersion. To compute

$\delta\Delta^{'}(s)$ and $\delta\Delta^{''}(s)$ we expand $\epsilon_{k+eA}+\epsilon_{k-eA}$ up to the fourth-order in A. Evaluating the obtained expression we obtain both $\delta\Delta^{'}$ and $\delta\Delta^{''}$:

$$\begin{aligned}\delta\Delta^{'}(s) &= \frac{1}{2}\left(\alpha_1\Delta e^2A^2(s)+\frac{1}{12}\tilde{\alpha}_1\Delta e^4A^4(s)\right)\left(1-\frac{1}{\lambda(4\Delta^2+s^2)F(s,T)}\right)\\ \delta\Delta^{''}(s) &= \underbrace{-\frac{\alpha_0}{s}\Delta e^2A^2(s)}_{=\delta\Delta^{''}_{A^2}(s)}\underbrace{-\frac{\tilde{\alpha}_0}{12s}\Delta e^4A^4(s)}_{=\delta\Delta^{''}_{A^4}(s)}\end{aligned} \tag{3.14}$$

where we separate $\delta\Delta^{'}(s)=\delta\Delta^{'}_{A^2}(s)+\delta\Delta^{'}_{A^4}(s)$ into two parts. The factors $\alpha_0=\frac{-\epsilon_F a^2}{2}$, $\tilde{\alpha}_0=\frac{\epsilon_F a^4}{2}$, $\alpha_1=\frac{-a^2}{2}$, $\tilde{\alpha}_1=\frac{a^4}{2}$ originate from the nearest-neighbour hopping term on a square lattice with a lattice constant denoted by a. For simplicity we set $a=1$. The function $F(s,T)$ is given by:

$$F(s,T)=\int \mathrm{d}\epsilon\frac{\tanh\left(\frac{E}{2k_BT}\right)}{2E(4E^2+s^2)} \tag{3.15}$$

For simplicity we have assumed that $\vec{A}(t)$ is parallel to the lattice vector.

Finally the current can be expressed via the z-component of the pseudospin as $\vec{j}(t)=\vec{v}_{k-eA}\left(\langle\hat{\sigma}^z_k(t)\rangle+\frac{1}{2}\right)$. We expand $\vec{v}_{k-eA}$ up to the third-order in A, transform $\vec{j}$ into Fourier space, and by plugging the expression for the gap oscillation we arrive at the following six terms, contributing to the FHG.

The Higgs contribution $\propto\delta\Delta^{'}(s)$ towards the fifth-order nonlinear current is given by

$$\begin{aligned}\vec{j}^{(5)H}_{\parallel}(5\Omega) = &-ie^2A_0\sum_k\frac{\Delta_0(\alpha_0+\alpha_1\xi_k)\tanh\left(\frac{E}{2k_BT}\right)}{E_k(4E_k^2-16\Omega^2)}2\xi_k\delta\Delta'_{A^4}(s=4i\Omega)\\ &+\frac{ie^4A_0^3}{24}\sum_k\frac{\Delta_0(\tilde{\alpha}_0+\tilde{\alpha}_1\xi_k)\tanh\left(\frac{E}{2k_BT}\right)}{E_k(4E_k^2-4\Omega^2)}2\xi_k\delta\Delta'_{A^2}(s=2i\Omega).\end{aligned} \tag{3.16}$$

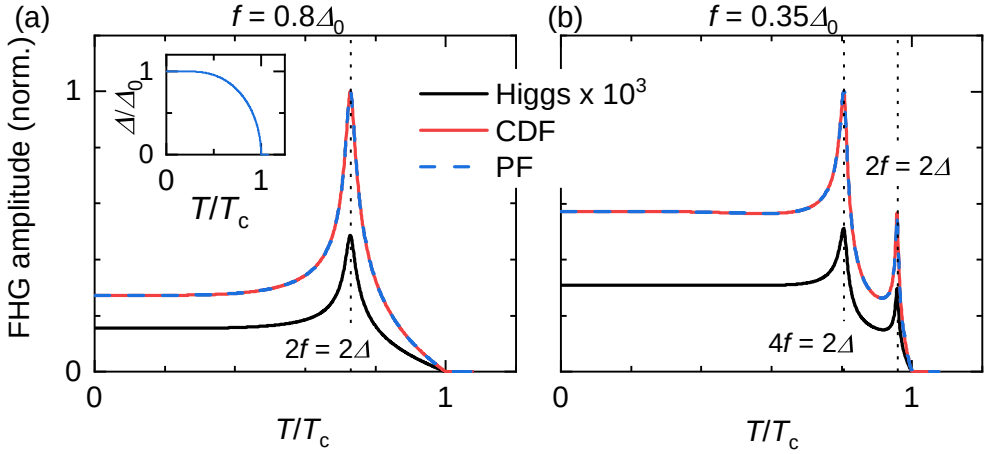

Figure 3.7: Amplitude of fifth-harmonic generation due to Higgs mode, charge-density fluctuations (CDF), and phase fluctuations (PF) for (a) $f = 0.8\Delta_0$ and (b) $f = 0.35\Delta_0$ in the clean limit. Inset: BCS-type temperature dependence of the superconducting gap.

where $\xi_k = \epsilon_k - \epsilon_F$ with ϵ_F the Fermi energy. Thus we obtain two components to the order of A^2 or A^4, respectively,

$$\begin{aligned} j^H_{A^2}(5\Omega) &= i\frac{\alpha_1\tilde{\alpha}_1\Delta^2 e^6 A_0^3 A^2(2i\Omega)}{24}\left(1-\frac{H(2i\Omega,T)}{2}-\frac{1}{2H(2i\Omega,T)}\right), \\ j^H_{A^4}(5\Omega) &= -i\frac{\alpha_1\tilde{\alpha}_1\Delta^2 e^6 A_0 A^4(4i\Omega)}{12}\left(1-\frac{H(4i\Omega,T)}{2}-\frac{1}{2H(4i\Omega,T)}\right), \end{aligned} \tag{3.17}$$

where we define $H(s,T) = \lambda(4\Delta^2 + s^2)F(s,T)$.

The contribution to FHG due to the phase fluctuations originates from the sum containing $\propto \delta\Delta''(s)$, i.e.

$$\begin{aligned} \vec{j}^{(5)P}_{\parallel}(5\Omega) = ie^2 A_0 \sum_k &\frac{\Delta_0(\alpha_0+\alpha_1\xi_k)\tanh\left(\frac{E}{2k_BT}\right)}{E_k(4E_k^2-16\Omega^2)} 4i\Omega\delta\Delta''_{A^4}(s=4i\Omega) \\ -\frac{ie^4A_0^3}{24}\sum_k &\frac{\Delta_0(\tilde{\alpha}_0+\tilde{\alpha}_1\xi_k)\tanh\left(\frac{E}{2k_BT}\right)}{E_k(4E_k^2-4\Omega^2)} 2i\Omega\delta\Delta''_{A^2}(s=2i\Omega) \end{aligned} \tag{3.18}$$

Hence

$$\begin{aligned} j^P_{A^2}(5\Omega) &= -i\frac{1}{12}\alpha_0\tilde{\alpha}_0\Delta^2 e^6 A_0^3 A^2(2i\Omega)\lambda F(2i\Omega,T), \\ j^P_{A^4}(5\Omega) &= i\frac{1}{6}\alpha_0\tilde{\alpha}_0\Delta^2 e^6 A_0 A^4(4i\Omega)\lambda F(4i\Omega,T). \end{aligned} \tag{3.19}$$

Finally, the BCS contribution due to Cooper-pair breaking (often dubbed charge density fluctuations) is

$$\begin{aligned} \vec{j}^{(5)\mathrm{CDF}}_{\parallel}(5\Omega) = ie^2 A_0 \sum_k & \frac{\Delta_0^2(\alpha_0+\alpha_1\xi_k)\tanh\left(\frac{E}{2k_BT}\right)}{E_k(4E_k^2-16\Omega^2)}\frac{1}{12}\xi_k^{A^4}(s=4i\Omega) \\ - \frac{ie^4A_0^3}{24}\sum_k & \frac{\Delta_0^2(\tilde{\alpha}_0+\tilde{\alpha}_1\xi_k)\tanh\left(\frac{E}{2k_BT}\right)}{E_k(4E_k^2-4\Omega^2)}\xi_k^{A^2}(s=2i\Omega) \end{aligned} \tag{3.20}$$

Two separate components are given by

$$\begin{aligned} j^{\mathrm{CDF}}_{A^2}(5\Omega) &= -i\frac{1}{12}\Delta^2 e^6 A_0^3 A^2(2i\Omega)\alpha_0\tilde{\alpha}_0\lambda F(2i\Omega,T) \\ &\quad - i\frac{1}{48}\Delta^2 e^6 A_0^3 A^2(2i\Omega)\alpha_1\tilde{\alpha}_1(1-H(2i\Omega,T)) \\ j^{\mathrm{CDF}}_{A^4}(5\Omega) &= i\frac{1}{6}\Delta^2 e^6 A_0 A^4(4i\Omega)\alpha_0\tilde{\alpha}_0\lambda F(4i\Omega,T) \\ &\quad + i\frac{1}{24}\Delta^2 e^6 A_0 A^4(4i\Omega)\alpha_1\tilde{\alpha}_1(1-H(4i\Omega,T)) \end{aligned} \tag{3.21}$$

One observes that some of the terms are almost identical to that appearing in the third-harmonic generation (THG) [40]. The new terms are those proportional to $A^4(4i\Omega)$.

Since the experimentally measured THz electric field is proportional to the time derivative of the current density, we compute the Fourier amplitude $\mathcal{F}(\partial j(t)/\partial t)$, which are just the expressions above with a leading factor of 5Ω. For the numerical computation we use $\lambda = 0.25$, $T_D = 500\,\mathrm{K}$, $t = 10\cdot\Delta_0$, $\epsilon_F = -200\,\mathrm{meV}$ and a broadening factor $\gamma = 0.025\Delta_0$ where $2\Delta_0 = 3.2$ meV denotes the superconducting gap at zero temperature, and assume a BCS-type temperature dependence of superconducting gap (see the

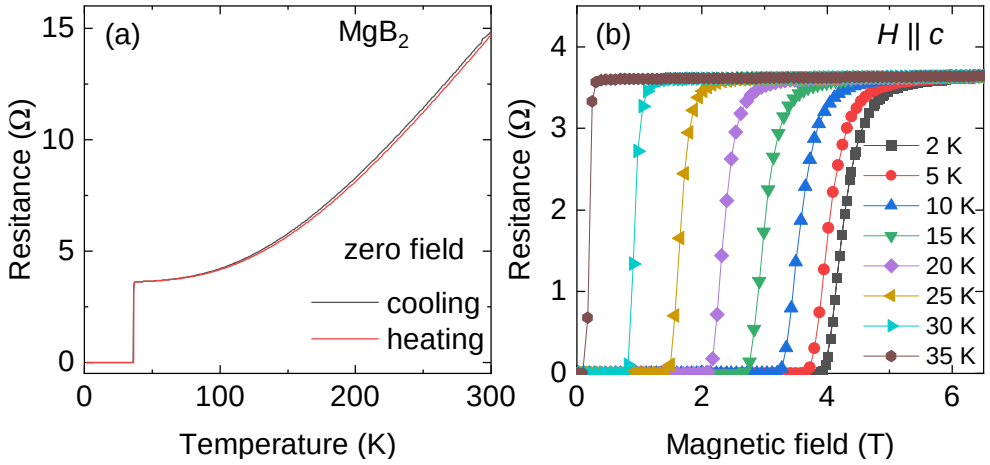

Figure 3.8: (a) temperature-dependent *dc*-resistance of a MgB_2 sample in zero field and (b) *dc* resistance measured upon field sweeping at different temperatures.

inset of Fig. 3.7).

The computed FHG amplitude of various contributions (Higgs amplitude mode, charge density fluctuations, and phase fluctuations) is presented in Fig. 3.7(a)(b) for pump-pulse frequencies $f = 0.8\Delta_0$ and $0.35\Delta_0$, respectively. The charge density fluctuations and phase fluctuations provide the same contribution to the FHG. For $f = 0.8\Delta_0$ which is greater than $\Delta_0/2$, we observe only one resonant peak in the FHG located at the temperature where $2\Delta(T) = 2f$. This is similar to the resonance condition for THG, meaning that this is the THG process carrying over into the FHG. In contrast, for frequencies below $\Delta_0/2$ such as $f = 0.35\Delta_0$, we find two distinct peaks at the temperatures T_1 and T_2, where $2\Delta(T_1) = 2f$ and $2\Delta(T_2) = 4f$. The additional peak at T_2 arises as the resonant excitation of a Higgs mode through four photons. In addition, we see that the BCS contribution dominates the FHG in the clean limit, as expected also for THG (see e.g. [35, 40]).

DC Resistance in Applied Magnetic Field

Figure 3.8 presents (a) temperature-dependent *dc*-resistance of a MgB_2 sample in zero field and (b) field-dependent *dc*-resistance measurements for various temperatures with the magnetic field applied along the crystallographic *c*-axis, which is the same orientation as applied in the high-harmonic generation experiment.

3.2.6 Contributions

Chris Reinhoffer, Zhe Wang and Paul van Loosdrecht conceived the project. The high-order harmonic measurements were performed at the TELBE facility in the Helmholtz center Dresden-Rossendorf. As beamline users Chris Reinhoffer, Patrick Pilch, Annecke Reinold and Zhe Wang were present. As beam line scientists, Sergey Kovalev, Jan-Christoph Deinert, Ivan Ilyakov, Alexey Ponomaryov and Min Chen were present. The pseudospin analysis were done by Paul Derendorf and I. M. Eremin. The MgB_2 thin films were grown and characterized by Tie-Quan Xu, Yue Wang, Zi-Zhao Gan, De-Sheng Wu, and Jian-Lin Luo. Chris Reinhofffer, Semyon Germanskiy, Evgeny Mashkovich, Paul van Loosdrecht and Zhe Wang did the main analysis and discussion of the experimental results. Chris Reinhoffer wrote the main part of the manuscript in close collaboration with Zhe Wang. All mentioned authors helped with refining the final written manuscript.

References

1. Reinhoffer, C. & et al. High-order nonlinear terahertz probing of the two-band superconductor MgB_2: Third- and fifth-order harmonic generation. *Physical Review B* **106,** 214514 (2022).
2. Anderson, P. W. Higgs, Anderson and all that. *Nature Physics* **11,** 93–93 (2015).
3. Chatrchyan, S. *et al.* Observation of a new boson at a mass of 125 GeV with the CMS experiment at the LHC. *Physics Letters B* **716,** 30–61 (2012).
4. Aad, G. *et al.* Observation of a new particle in the search for the Standard Model Higgs boson with the ATLAS detector at the LHC. *Physics Letters B* **716,** 1–29 (2012).
5. Francois Englert & Peter W. Higgs. *The Nobel Prize in Physics 2013* NobelPrize.org.
6. Giorgianni, F. *et al.* Leggett mode controlled by light pulses. *Nature Physics* **15,** 341–346 (2019).
7. Kovalev, S. *et al.* Band-selective third-harmonic generation in superconducting MgB_2 : Possible evidence for the Higgs amplitude mode in the dirty limit. *Physical Review B* **104,** L140505 (2021).
8. Shimano, R. & Tsuji, N. Higgs Mode in Superconductors. *Annual Review of Condensed Matter Physics* **11,** 103–124 (2020).
9. Cyrot, M. Ginzburg-Landau theory for superconductors. *Reports on Progress in Physics* **36,** 103 (1973).

10. Schwarz, L. *et al.* Classification and characterization of nonequilibrium Higgs modes in unconventional superconductors. *Nature Communications* **11,** 287 (Jan. 15, 2020).

11. Dong, T., Zhang, S.-J. & Wang, N.-L. Recent Development of Ultrafast Optical Characterizations for Quantum Materials. *Advanced Materials* **35,** 2110068 (2023).

12. Momma, K. & Izumi, F. VESTA 3 for three-dimensional visualization of crystal, volumetric and morphology data. *Journal of Applied Crystallography* **44,** 1272–1276 (2011).

13. Nagamatsu, J. *et al.* Superconductivity at 39 K in magnesium diboride. *Nature* **410,** 63–64 (2001).

14. Eisterer, M. Magnetic properties and critical currents of MgB_2. *Superconductor Science and Technology* **20,** R47 (2007).

15. Askerzade, I. N. Temperature dependence of some superconducting state parameters of a bulk MgB_2 in two-band Ginzburg–Landau theory. *Physica C: Superconductivity* **390,** 281–285 (2003).

16. Ravindran, P. *et al.* Detailed electronic structure studies on superconducting MgB_2 and related compounds. *Physical Review B* **64,** 224509 (2001).

17. Kaindl, R. A. *et al.* Far-Infrared Optical Conductivity Gap in Superconducting MgB_2 Films. *Physical Review Letters* **88,** 027003 (2001).

18. London, F., London, H. & Lindemann, F. A. The electromagnetic equations of the supraconductor. *Proceedings of the Royal Society of London. Series A - Mathematical and Physical Sciences* **149,** 71–88 (1997).

19. Corkum, P. B. & Krausz, F. Attosecond science. *Nature Physics* **3,** 381–387 (2007).

20. Ghimire, S. & Reis, D. A. High-harmonic generation from solids. *Nature Physics* **15,** 10–16 (2019).

21. Ghimire, S. *et al.* Observation of high-order harmonic generation in a bulk crystal. *Nature Physics* **7,** 138–141 (2011).

22. Schubert, O. *et al.* Sub-cycle control of terahertz high-harmonic generation by dynamical Bloch oscillations. *Nature Photonics* **8,** 119–123 (2014).

23. Luu, T. T. *et al.* Extreme ultraviolet high-harmonic spectroscopy of solids. *Nature* **521,** 498–502 (2015).

24. Vampa, G. *et al.* All-Optical Reconstruction of Crystal Band Structure. *Physical Review Letters* **115,** 193603 (2015).

25. You, Y. S., Reis, D. A. & Ghimire, S. Anisotropic high-harmonic generation in bulk crystals. *Nature Physics* **13,** 345–349 (2017).

26. Liu, H. *et al.* High-harmonic generation from an atomically thin semiconductor. *Nature Physics* **13,** 262–265 (2017).

27. Soavi, G. *et al.* Broadband, electrically tunable third-harmonic generation in graphene. *Nature Nanotechnology* **13,** 583–588 (2018).

28. Hafez, H. A. *et al.* Extremely efficient terahertz high-harmonic generation in graphene by hot Dirac fermions. *Nature* **561,** 507–511 (2018).

29. Kovalev, S. *et al.* Non-perturbative terahertz high-harmonic generation in the three-dimensional Dirac semimetal Cd_3As_2. *Nature Communications* **11,** 2451 (2020).

30. Cheng, B. *et al.* Efficient Terahertz Harmonic Generation with Coherent Acceleration of Electrons in the Dirac Semimetal Cd_3As_2. *Physical Review Letters* **124,** 117402 (2020).

31. Bai, Y. *et al.* High-harmonic generation from topological surface states. *Nature Physics* **17,** 311–315 (2021).

32. Lv, Y.-Y. *et al.* High-harmonic generation in Weyl semimetal β-WP_2 crystals. *Nature Communications* **12,** 6437 (2021).

33. Dantas, R. M. A. *et al.* Nonperturbative topological current in Weyl and Dirac semimetals in laser fields. *Physical Review B* **103,** L201105 (2021).

34. Kemper, A. F. *et al.* Theoretical description of high-order harmonic generation in solids. *New Journal of Physics* **15,** 023003 (2013).

35. Cea, T., Castellani, C. & Benfatto, L. Nonlinear optical effects and third-harmonic generation in superconductors: Cooper pairs versus Higgs mode contribution. *Physical Review B* **93,** 180507 (2016).

36. Tsuji, N., Murakami, Y. & Aoki, H. Nonlinear light–Higgs coupling in superconductors beyond BCS: Effects of the retarded phonon-mediated interaction. *Physical Review B* **94,** 224519 (2016).

37. Tancogne-Dejean, N. *et al.* Impact of the Electronic Band Structure in High-Harmonic Generation Spectra of Solids. *Physical Review Letters* **118,** 087403 (2017).

38. Silva, R. E. F. *et al.* High-harmonic spectroscopy of ultrafast many-body dynamics in strongly correlated systems. *Nature Photonics* **12,** 266–270 (2018).

39. Takayoshi, S., Murakami, Y. & Werner, P. High-harmonic generation in quantum spin systems. *Physical Review B* **99,** 184303 (2019).

40. Schwarz, L. & Manske, D. Theory of driven Higgs oscillations and third-harmonic generation in unconventional superconductors. *Physical Review B* **101,** 184519 (2020).

41. Murotani, Y. & Shimano, R. Nonlinear optical response of collective modes in multiband superconductors assisted by nonmagnetic impurities. *Physical Review B* **99,** 224510 (2019).

42. Haenel, R. *et al.* Time-resolved optical conductivity and Higgs oscillations in two-band dirty superconductors. *Physical Review B* **104,** 134504 (2021).

43. Müller, M. A. & Eremin, I. M. Signatures of Bardasis-Schrieffer mode excitation in third-harmonic generated currents. *Physical Review B* **104,** 144508 (2021).

44. Shao, C. *et al.* High-Harmonic Generation Approaching the Quantum Critical Point of Strongly Correlated Systems. *Physical Review Letters* **128,** 047401 (2022).

45. Matsunaga, R. *et al.* Light-induced collective pseudospin precession resonating with Higgs mode in a superconductor. *Science* **345,** 1145–1149 (2014).

46. Rajasekaran, S. *et al.* Probing optically silent superfluid stripes in cuprates. *Science* **359,** 575–579 (2018).

47. Yang, X. *et al.* Lightwave-driven gapless superconductivity and forbidden quantum beats by terahertz symmetry breaking. *Nature Photonics* **13,** 707–713 (2019).

48. Chu, H. *et al.* Phase-resolved Higgs response in superconducting cuprates. *Nature Communications* **11,** 1793 (2020).

49. Uchida, K. *et al.* High-Order Harmonic Generation and Its Unconventional Scaling Law in the Mott-Insulating Ca_2RuO_4. *Physical Review Letters* **128,** 127401 (2022).

50. Wang, Z.-X. *et al.* Transient Higgs oscillations and high-order nonlinear light-Higgs coupling in a terahertz wave driven NbN superconductor. *Physical Review B* **105,** L100508 (2022).

51. Germanskiy, S. *et al.* Ellipticity control of terahertz high-harmonic generation in a Dirac semimetal. *Physical Review B* **106,** L081127 (2022).

52. Pekker, D. & Varma, C. Amplitude / Higgs Modes in Condensed Matter Physics. *Annual Review of Condensed Matter Physics* **6,** 269–297 (2015).

53. Vaswani, C. *et al.* Terahertz Second-Harmonic Generation from Lightwave Acceleration of Symmetry-Breaking Nonlinear Supercurrents. *Physical Review Letters* **124,** 207003 (2020).

54. Nakamura, S. *et al.* Nonreciprocal Terahertz Second-Harmonic Generation in Superconducting NbN under Supercurrent Injection. *Physical Review Letters* **125,** 097004 (2020).

55. Kfir, O. *et al.* Generation of bright phase-matched circularly-polarized extreme ultraviolet high harmonics. *Nature Photonics* **9,** 99–105 (2015).

56. Fan, T. *et al.* Bright circularly polarized soft X-ray high harmonics for X-ray magnetic circular dichroism. *Proceedings of the National Academy of Sciences* **112,** 14206–14211 (2015).

57. Cireasa, R. *et al.* Probing molecular chirality on a sub-femtosecond timescale. *Nature Physics* **11,** 654–658 (2015).

58. Kovalev, S. *et al.* Probing ultra-fast processes with high dynamic range at 4th-generation light sources: Arrival time and intensity binning at unprecedented repetition rates. *Structural Dynamics* **4,** 024301 (2017).

59. Kortus, J. *et al.* Superconductivity of Metallic Boron in MgB_2. *Physical Review Letters* **86,** 4656–4659 (2001).

60. Szabó, P. *et al.* Evidence for Two Superconducting Energy Gaps in MgB_2 by Point-Contact Spectroscopy. *Physical Review Letters* **87,** 137005 (2001).

61. Iavarone, M. *et al.* Two-Band Superconductivity in MgB_2. *Physical Review Letters* **89,** 187002 (2002).

62. Souma, S. *et al.* The origin of multiple superconducting gaps in MgB_2. *Nature* **423,** 65–67 (2003).

63. Koshelev, A. E. & Golubov, A. A. Mixed State of a Dirty Two-Band Superconductor: Application to MgB_2. *Physical Review Letters* **90,** 177002 (2003).

64. Eskildsen, M. R. *et al.* Vortex Imaging in the π Band of Magnesium Diboride. *Physical Review Letters* **89,** 187003 (2002).

65. Guritanu, V. *et al.* Anisotropic optical conductivity and two colors of MgB_2. *Physical Review B* **73,** 104509 (2006).

66. Tan, T. *et al.* Enhancement of lower critical field by reducing the thickness of epitaxial and polycrystalline MgB_2 thin films. *APL Materials* **3,** 041101 (2015).

67. Eltsev, Y. *et al.* Anisotropic superconducting properties of MgB_2 single crystals probed by in-plane electrical transport measurements. *Physical Review B* **65,** 140501 (2002).

68. Welp, U. *et al.* Superconducting phase diagram of single-crystal MgB_2. *Physica C: Superconductivity* **385,** 154–161 (2003).

69. Das, P. *et al.* Observation of Well-Ordered Metastable Vortex Lattice Phases in Superconducting MgB_2 Using Small-Angle Neutron Scattering. *Physical Review Letters* **108,** 167001 (2012).

70. Xu, Y. *et al.* Time-Resolved Photoexcitation of the Superconducting Two-Gap State in MgB_2 Thin Films. *Physical Review Letters* **91,** 197004 (2003).

71. Demsar, J. *et al.* Pair-Breaking and Superconducting State Recovery Dynamics in MgB_2. *Physical Review Letters* **91,** 267002 (2003).

72. Baldini, E. *et al.* Real-Time Observation of Phonon-Mediated σ-π Interband Scattering in MgB_2. *Physical Review Letters* **119,** 097002 (2017).

73. Novko, D. *et al.* Ultrafast Hot Phonon Dynamics in MgB_2 Driven by Anisotropic Electron-Phonon Coupling. *Physical Review Letters* **124,** 077001 (2020).

74. Fiore, J. *et al.* Contribution of collective excitations to third harmonic generation in two-band superconductors: The case of MgB_2. *Physical Review B* **106,** 094515 (2022).

75. Zhang, C. *et al.* Hybrid Physical - Chemical Vapor Deposition of Ultrathin MgB_2 Films on MgO Substrate With High TC and JC. *IEEE Transactions on Applied Superconductivity* **23,** 7500204–7500204 (2013).

76. Tu, J. J. *et al.* Optical Properties of c-Axis Oriented Superconducting MgB_2 Films. *Physical Review Letters* **87,** 277001 (2001).

77. Pronin, A. V. *et al.* Optical Conductivity and Penetration Depth in MgB_2. *Physical Review Letters* **87,** 097003 (2001).

78. Jin, B. B. *et al.* Terahertz surface impedance of epitaxial MgB_2 thin film. *Applied Physics Letters* **87,** 092503 (2005).

79. Ortolani, M. *et al.* Two-band parallel conductivity at terahertz frequencies in the superconducting state of MgB_2. *Physical Review B* **77,** 100507 (2008).

80. Boyd, R. W. *Nonlinear Optics* 4th ed. ISBN: 978-0-12-811003-4 (Elsevier Science & Techn., 2020).

81. Andreone, A *et al.* Study of the microwave electrodynamic response of MgB_2 thin films. *Physica C: Superconductivity* **372-376,** 1287–1290 (2002).

82. Booth, J. C. *et al.* Nonlinear microwave response of MgB_2 thin films. *Superconductor Science and Technology* **16,** 1518 (2003).

83. Gallitto, A. A., Bonsignore, G. & Li Vigni, M. THIRD-HARMONIC EMISSION IN MgB_2 SUPERCONDUCTOR AT MICROWAVE FREQUENCIES. *International Journal of Modern Physics B* **17,** 535–541 (2003).

84. Oates, D. E., Agassi, D. & Moeckly, B. H. Intermodulation and power handling in MgB_2 thin films. *Journal of Physics: Conference Series* **97,** 012204 (2008).

85. Tai, T. *et al.* MgB_2 nonlinear properties investigated under localized high rf magnetic field excitation. *Physical Review Special Topics - Accelerators and Beams* **15,** 122002 (2012).

86. Dahm, T. & Scalapino, D. J. Nonlinear microwave response of MgB_2. *Applied Physics Letters* **85,** 4436–4438 (2004).

87. Xu, D., Yip, S. K. & Sauls, J. A. Nonlinear Meissner effect in unconventional superconductors. *Physical Review B* **51,** 16233–16253 (1995).

88. Samoilova, T. B. Non-linear microwave effects in thin superconducting films. *Superconductor Science and Technology* **8,** 259 (1995).

89. Jujo, T. Quasiclassical Theory on Third-Harmonic Generation in Conventional Superconductors with Paramagnetic Impurities. *Journal of the Physical Society of Japan* **87,** 024704 (2018).

90. Silaev, M. Nonlinear electromagnetic response and Higgs-mode excitation in BCS superconductors with impurities. *Physical Review B* **99,** 224511 (2019).

91. Seibold, G. *et al.* Third harmonic generation from collective modes in disordered superconductors. *Physical Review B* **103,** 014512 (2021).

92. Derendorf, P., Müller, M. A. & Eremin, I. M. Signatures of collective modes in fifth harmonic generation of BCS superconductor. *Faraday Discussions* **237,** 186–197 (2022).

4 Terahertz Magnonics in $(Gd,Bi)_3Fe_5O_{12}$

4.1 Introduction

The main content of this chapter is the manuscript prepared for publication in Physical Review B "Reinhoffer et al. THz Control of Exchange Mode in a Ferrimagnetic Cavity (2024)" investigating the terahertz (THz) induced magnetization dynamics in the rare earth iron garnet $(Gd,Bi)_3Fe_5O_{12}$ within a cavity created by the sample interfaces. By changing the temperature of the sample a periodic modulation of the exchange mode amplitude is observed with maxima appearing when the exchange mode frequency matches the frequency of a cavity mode. This phenomenon is described by a simulation of the magnetization dynamics using Landau-Lifshitz-Gilbert (LLG) equations under a pulsed periodic drive. To understand the physical principles involved, this section will first introduce the magnetization dynamics of a ferrimagnet with linear exchange coupling between the sublattices. Furthermore, the assumptions for the simulations with the LLG equations will be discussed. After which the physical properties of $(Gd,Bi)_3Fe_5O_{12}$ are introduced to better understand the origin of the highly tunable nature of the exchange mode.

4.1.1 Landau-Lifshitz-Gilbert Equations and Magnetization Dynamics in Ferrimagnets

One of the most well-known phenomena in physics is precession of a top when the gravitational and rotational forces are misaligned [1]. This process is a result of conservation of angular momentum and is applicable to magnetic moments in magnetic fields [1–3]. When a magnetic dipole moment m is in an applied magnetic field H with an angle between the moment and field axis, the magnetic dipole starts to precess around the magnetic field vector (shown in Fig. 4.1 (a)) with the Larmor frequency

$$f_{\text{Lamor}} = \frac{\gamma}{2\pi} B, \tag{4.1}$$

with γ the gyromagnetic ratio, and B the magnetic flux density, in a vacuum $B = \mu_0 H$ [2, 3]. This precessional motion can be described by the Landau-Lifshitz-Gilbert equation

$$\frac{d\vec{m}}{dt} = -\gamma \vec{m} \times \vec{B} - \beta \vec{m} \times \left(\vec{m} \times \vec{B} \right), \tag{4.2}$$

with β a phenomenological damping parameter [3, 4]. The term $\gamma \vec{m} \times \vec{B}$ describes the torque applied leading to the rotational motion with $\beta \vec{m} \times \left(\vec{m} \times \vec{B} \right)$ describing the damping of the amplitude of the oscillation [3, 4]. However, equation 4.2 is a description of a single magnetic moment within a field. Extending this description to the material case is done by including a macroscopic magnetization $\vec{M}$

$$\frac{d\vec{M}}{dt} = -\gamma \vec{M} \times \mu_0 \vec{H}_{\text{eff.}} - \gamma \frac{\alpha}{|\vec{M}|} \vec{M} \times \left(\vec{M} \times \mu_0 \vec{H}_{\text{eff.}} \right), \tag{4.3}$$

with α the Gilbert damping parameter, $|\vec{M}|$ representing the saturation magnetization, and $\vec{H}_{\text{eff.}}$ the effective applied magnetic field influenced by magnetization and interactions [3, 4].

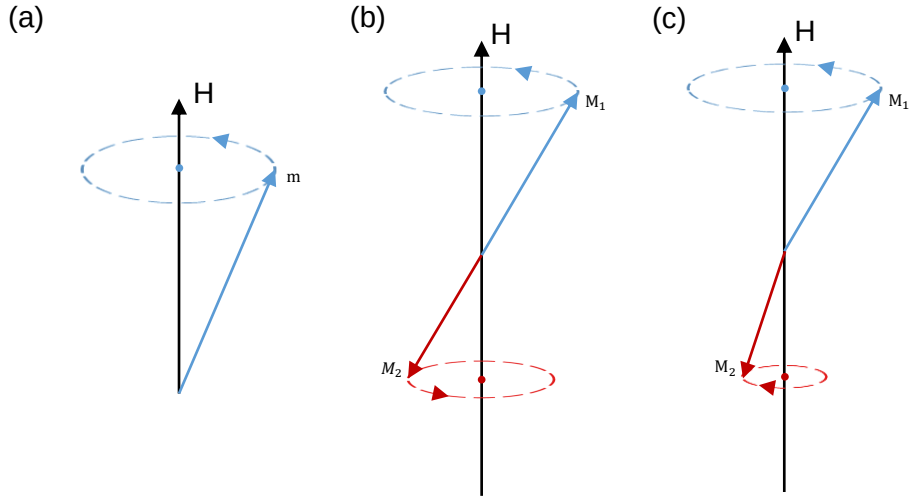

Figure 4.1: Precession of magnetic moments in an external magnetic field. (a) Larmor precession of a simple magnetic moment. (b) Quasi-ferromagnetic mode and (c) quasi-antiferromagnetic mode of a ferrimagnet.

A ferrimagnet consists of magnetic moments with different magnitudes aligned anti-parallel to each other [3]. Because they have different magnetic moments, a ferrimagnet has a nonzero macroscopic magnetization [3]. This results in them showing modes that scale with applied field as a ferromagnetic mode, therefore called quasi-ferromagnetic [3]. However, an additional mode appears that is not explainable by a single equation of motion [4–6]. This can be remedied by imagining the ferrimagnet as a system of two magnetizations that are coupled to each other, leading to a system of coupled equations:

$$\frac{d\vec{M}_1}{dt} = -\gamma \vec{M}_1 \times \vec{H}_{\text{eff.}} - \gamma \frac{\alpha}{|\vec{M}|} \vec{M}_1 \times \left(\vec{M}_1 \times \vec{H}_{\text{eff.}} \right), \tag{4.4}$$

$$\frac{d\vec{M}_2}{dt} = -\gamma \vec{M}_2 \times \vec{H}_{\text{eff.}} - \gamma \frac{\alpha}{|\vec{M}|} \vec{M}_2 \times \left(\vec{M}_2 \times \vec{H}_{\text{eff.}} \right), \tag{4.5}$$

with M_1 and M_2 describing the magnetizations of the different subsystems [4,

5]. In the case of no damping and a linear coupling between the magnetizations through an exchange field $H = N_{12}(M_2 - M_1)$ with N_{12} the exchange parameter, this set of coupled equations gives rise to the Kaplan-Kittel exchange resonance with frequency

$$\omega = \gamma N_{12} \left(|\vec{M}_2| - |\vec{M}_1| \right), \tag{4.6}$$

in addition to the quasi-ferromagnetic mode [4–6]. Both modes of a ferrimagnet are sketched in Fig 4.1 (b) and (c), while in the quasi-ferromagnetic mode both magnetizations precess in unison, in the quasi-antiferromagnetic mode the magnetizations cant with respect to each other while they precess counter to each other.

The system of coupled differential equations is the basis for the description of the magnetization dynamics in $(Gd,Bi)_3Fe_5O_{12}$ (GdBIG) observed in section 4.2. The properties of GdBIG will be discussed in the next section. In the rest of this section, the focus will be on some detail of the numerical simulation. In contrast to section 2.2, the interest is in directional components of the magnetization requiring a full three-dimensional treatment. For that purpose, equations 4.4 and 4.5 are written in terms of the Euler method:

$$\vec{M}_1(t+\Delta t) = \vec{M}_1(t) - \Delta t\gamma \left[\vec{M}_1(t) \times \vec{H}_{\text{eff.}}(t) - \frac{\alpha}{|\vec{M}|} \vec{M}_1(t) \times \left(\vec{M}_1(t) \times \vec{H}_{\text{eff.}}(t) \right) \right] \tag{4.7}$$

$$\vec{M}_2(t+\Delta t) = \vec{M}_2(t) - \Delta t\gamma \left[\vec{M}_2(t) \times \vec{H}_{\text{eff.}}(t) - \frac{\alpha}{|\vec{M}|} \vec{M}_2(t) \times \left(\vec{M}_2(t) \times \vec{H}_{\text{eff.}}(t) \right) \right]. \tag{4.8}$$

This set of equations can be iteratively solved using the effective magnetic field and the values for γ, α, and N_{12} found in the section 4.2. To extract the frequency of the exchange mode, the system is brought out of equilibrium with a single light pulse. By changing the magnetizations $\vec{M}_1$ and $\vec{M}_2$ the system is simulated at different temperatures. Extracting the frequency of the oscillation therefore results in a temperature dependence of the exchange mode. This is used for extracting the amplitude of the exchange mode when

the excitation becomes more complicated then a single pulse.

4.1.2 Properties $(Gd,Bi)_3Fe_5O_{12}$

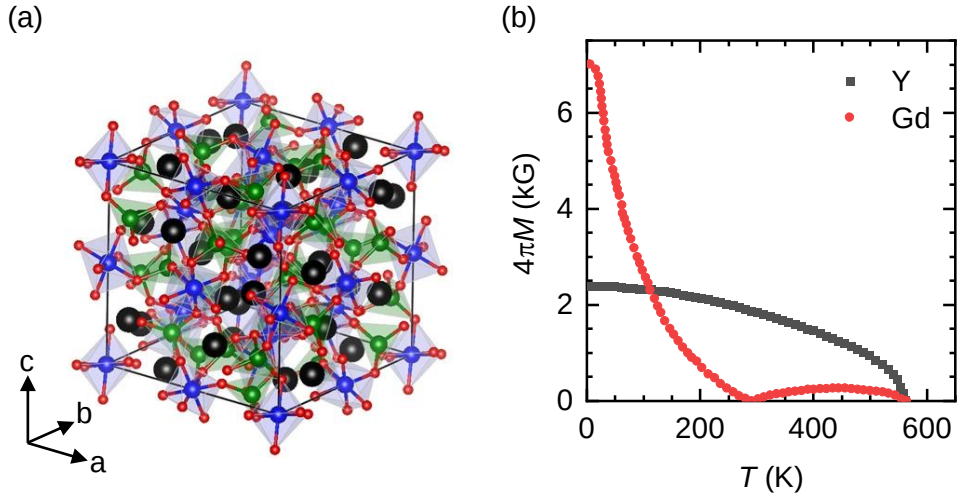

Figure 4.2: Structural and magnetic properties of garnets. (a) Garnet unit cell with the tetrahedral, octahedral, and vacancy sites shown in blue, green, and black, respectively. Figure adapted from Andrew J. Princep et al. The full magnon spectrum of yttrium iron garnet. *npj Quantum materials* **2**, 63 (2017) [7] under CC 4.0 license. (b) Magnetization of the rare earth iron garnets YIG and GdIG, data adapted from [8].

The crystallographic family of the garnets has found use in a wide range of applications thanks to their highly tunable nature [4]. One of the most prominent examples is the use in high powered lasers where rare earth doped yttrium aluminum garnets (YAG), i.e., Nd:YAG and Yb:YAG, are used as gain medium [9, 10]. The reason for this versatility is the garnet structure shown in Fig. 4.2 (a) [11, 12]. The structure consists of three sites: the oxygen tetrahedral sites shown in green, the oxygen octahedral sites shown in blue, and the vacancy sites shown in black [4, 7, 13]. In the case of YAG, the tetrahedral and octahedral sites are occupied by aluminum and the vacancy sites by yttrium.

For magnetic tunability, the aluminum can be replaced by magnetic ions like iron, resulting in the well-studied yttrium iron garnet (YIG) [7, 13]. Figure 4.2 (b) shows the magnetization of YIG (gray squares) as a function of temperature [4, 13]. YIG shows a magnetization below the Curie temperature $T_c = 550$ K which increases with decreasing temperature saturating at $5\mu_B$/formula unit [4, 13]. However, with the magnetic moment per iron in 3+ oxidation being $5\mu_B$ and 5 iron ions per formula unit, the expected magnetization summing over the magnetic moments would be $25\mu_B$/formula unit for a ferromagnetically ordered crystal. This shows that the two iron sites (octahedral and tetrahedral) couple antiferromagnetically with each other with the ratio being 2:3 resulting in ferrimagnetic order with residual magnetization of $5\mu_B$/formula unit [4, 13]. The exchange between these two iron sublattices is mediated via the super exchange mechanism [4, 13].

Replacing the yttrium with gadolinium changes the temperature dependence of the magnetization drastically [13]. Figure 4.2 (b) shows the magnetization as a function of temperature for GdIG (red dots). The Curie temperature is still at 550 K, being a result of the iron lattices ordering [13]. However, after a short increase in magnetization with decreasing temperature, there is a temperature point of zero magnetization [4, 13–15]. The explanation for this phenomenon is that the magnetic moments of the Gd ions align antiferromagnetically to the net magnetization generated by the combined iron sublattices without being strongly coupled with each other [13–15]. However, the magnetic moment carried by Gd^{3+} is larger than Fe^{3+}, therefore leading to a point where the Gd moment can compensate the magnetization of the iron sublattices, resulting in a net zero magnetization. The temperature where this occurs is called compensation temperature T_{comp} [13–15]. In a ferrimagnet, the net magnetization aligns itself with externally applied magnetic fields [3]. Therefore, when $M_{Gd} < M_{Fe}$ above T_{comp} the magnetization of the iron sublattice is aligned along the external field while when $M_{Gd} > M_{Fe}$ below T_{comp} the Gd moments are aligned along the field [4, 13–15]. This switch of magnetization direction is not visible in the magnetization but can be made visible by measuring magneto-optic Kerr effect (MOKE) with 800 nm as a probe

wavelength [4]. The Kerr coefficient for 800 nm is dominated by the response of one of the iron sublattices, due to crystal field excitations of the iron ions in the octahedral sites at 700 nm and 900 nm, making it sensitive to the direction of the magnetization [4, 16]. This effect can be enhanced by substituting Gd with Bi which shifts the crystal field transitions, increasing the observed magneto-optic effect with 800 nm [16]. The sensitivity to the magnetization direction is combined with a THz excitation and LLG analysis in the next section to study the temporal magnetization dynamics of $(Gd,Bi)_3Fe_5O_{12}$.

4.2 THz Control of Exchange Mode in a Ferrimagnetic Cavity

4.2.1 Introduction

In an era where large language models are becoming increasingly dominant in society, the need for faster computational power is more pronounced than ever before [17]. However, the predominant form of data storage technology today is still ferromagnetic-based, which limits operational frequencies to a few GHz [18]. To achieve significantly higher frequencies, i.e. in the THz range, antiferromagnetic magnetic recording and control is the subject of intense investigation nowadays [19–30]. Among media with antiferromagnetic ordering, ferrimagnets are especially appealing as they combine the feasibility of magnetic control with high THz-scale eigenfrequencies. One material class at the center of these investigations has been the rare earth iron garnets [6, 27–29]. Iron garnets crystallize in the lā3d structure where the iron ions form two sublattices sitting in oxygen octahedral $\vec{M}_\mathrm{a}$ and tetrahedral sites $\vec{M}_\mathrm{d}$ with a ratio of 10 μ_B:15 μ_B, while the rare earth ions occupy the interstitial sites. By substituting the main rare earth element [8], and by doping with non-magnetic ions [31], the magnetic properties of these materials become highly tunable. Due to the strong Fe-Fe exchange interaction, iron garnets typically are treated as ferrimagnets characterized by two sublattices: Gadolinium $\vec{M}_\mathrm{Gd} = \vec{M}_\mathrm{c}$ and joint iron $\vec{M}_\mathrm{Fe} = \vec{M}_\mathrm{d} + \vec{M}_\mathrm{a}$, respectively. The strength of the exchange interaction between these sublattices can be directly probed by measuring the corresponding magnetic exchange mode [5]. The frequency of this resonance is highly sensitive to temperature, especially in the vicinity of the magnetic compensation point, where $|\vec{M}_\mathrm{Fe}| = |\vec{M}_\mathrm{Gd}|$. Furthermore, substitution of Gd with Bi enhances the magneto-optical response, enabling ultrafast magneto-optical spectroscopy [16, 32]. The exchange mode can be excited either resonatly [33] or via opto-magnetic effects [27].

There are several approaches to increase the coupling strength between photons and magnons: some are based on energy concentration using cavities [34–36], while others exploit multiple terahertz pulses as a stimulus to

coherently control the magnon response [37, 38]. In this paper, we combine the concepts of cavity engineering with multiple THz pulse excitation to demonstrate the vast tuning possibilities of the coupling strength between light and magnetization at THz frequencies. Specifically, we analyze the practically important case where the cavity is created by the two interfaces of a plane-parallel micron-scale plate made of the ferrimagnet itself. The tunability of the exchange mode frequency through temperature control allows us to couple it with multiple cavity modes in a controllable way. By performing THz-pump optical-probe experiments, we monitor the amplitude and the frequency of the exchange mode to reveal the corresponding magnon-photon coupling strength at various temperatures. The enhancement of the mode amplitude is readily observable when the frequency of the magnon mode is resonant with an eigenmode of the cavity, while a reduction of the effective damping is observed across the full temperature range between 80 and 130 K. Numerical simulation based on Landau-Lifschitz-Gilbert equations in a two-sublattice system in a cavity show good agreement with the experimental findings. Overall, this work touches on a previously unexplored realm of THz cavity spin dynamics and provides a systematic understanding of the dynamical magnetic response of a ferrimagnetic cavity.

4.2.2 Material and Methods

A 200 μm thick single crystal of $(Gd,Bi)_3Fe_5O_{12}$ (GdBIG) oriented along the (111) direction was grown using liquid phase epitaxy and polished to the prescribed thickness [27]. The sample was mounted in a continuous flow cryostat and cooled using liquid nitrogen with a dc magnetic field applied in the sample plane. Broadband THz pulses were generated using the tilted-pulse-front optical rectification technique in a $LiNbO_3$ crystal [39]. For that optical pulses from a Ti:sapphire amplifier with 6 mJ per pulse, 1 kHz repetition rate and a center wavelength of 800 nm were used. Part off this beam was split of to be used as a low intensity probe pulse. Two types of THz spectroscopy experiments were conducted: THz time-domain (TDS) spectroscopy

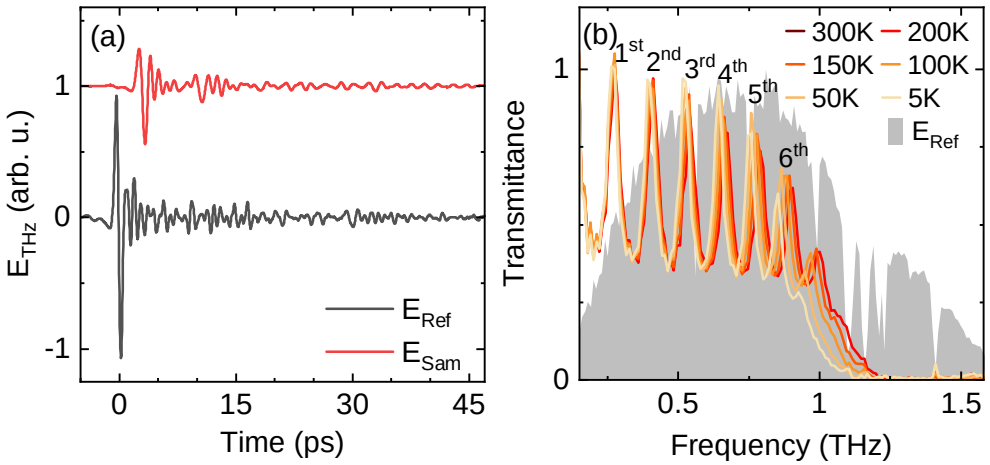

Figure 4.3: Static characterization of GdBIG. (a) THz electric field transmitted through the sample E_{Sam} and an empty sample holder E_{Ref} at room temperature, offset for better visibility. (b) Transmission spectrum of GdBIG at different temperatures. The reference spectrum is shown as a gray background, where the sharp absorption lines result from the water vapor absorption. The cavity modes are numbered according to their order.

and THz-pump optical-probe (TPOP). In TDS, the THz beam was transmitted through the GdBIG sample, after which the THz pulse field strength was detected via electro-optic sampling in a 1 mm thick ZnTe crystal [40]. TPOP was performed by overlapping the 800 nm probe beam with the THz beam within the sample. The THz-induced changes of the probe polarization were detected using the balanced photodiode technique [40]. Both the THz and optical radiation were at normal incidence. For both experimental configurations, the polarization state and fluence of the THz radiation was controlled using two wire grid polarizers. In TDS the THz electric field strength was reduced below 10 $\frac{kV}{cm}$, whereas for TPOP, THz field strengths up to 700 $\frac{kV}{cm}$ were used.

4.2.3 Results

As a first step, the transmission properties of GdBIG were studied by THz TDS spectroscopy at different temperatures. Figure 4.3(a) shows the THz

electric field transmitted through the sample E_{Sam} and the reference THz electric field E_{Ref} at room temperature. The main peak of E_{Sam} is delayed by $\sim$3.1 ps compared to the reference signal. Furthermore, a second peak at $\sim$10.7 ps is visible, originating in the back reflection of the THz pulse from the rear interface of GdBIG. For a sample thickness of 200 μm and the time delay observed in E_{Ref} the effective refractive index n, in the $\sim$ 1 THz frequency range, is estimated to be $\sim$5.6. The amplitude transmission spectra plotted in Fig. 4.3(b) are calculated as the ratio of the absolute values of the E_{Sam} and E_{Sam} FFT spectra. A strong periodic modulation of the transmission is observed, which is caused by formation of a THz pulse train due to multiple reflections from both crystal interfaces [16]. The peaks shift to lower frequencies with decreasing temperature indicating an increase in the refractive index. Moreover, the sample becomes non-transparent above 1.3 THz at 300 K and above 1.1 THz at 5 K, indicating the presence of an absorption line outside of the spectral window which is softening with decreasing temperature. This absorption line is absent in pure $Gd_3Fe_5O_{12}$ [41], which suggests that this could be a phonon mode involving Bi in the interstitial sites. This notion is reinforced by the appearance of a Raman-active optical phonon at 1.8 THz when substituting Gd with Tb in $Gd_{2.34}Tb_{0.66}Fe_5O_{12}$ [42]. Without changing the coupling strength, the mass ratio between the Tb and Bi ions would lower this phonon frequency to $\approx$1.6 THz. Furthermore, room temperature Raman measurements (Fig. 4.6) shows the presence of a peak at 1.28 THz. According to the mutual exclusion principle [43], the appearance of this mode in both Raman and IR spectra can be explained by the lowering of the crystal symmetry due to the random distribution of Bi dopants in GdBIG [44].

Next, TPOP spectroscopy was performed. Figure 4.4(a) shows THz induced polarization rotation at three distinct temperatures of 130 K, 100 K, and 80 K. The time traces indicate a rich frequency spectrum which is strongly temperature-dependent. Corresponding Fourier spectra are plotted in Fig. 4.4(b) showing multiple peaks composing the induced polarization rotation in Fig. 4.4(a). Two of the most pronounced features, centered at 0.13 THz and 0.26 THz, do not move with temperature, while the frequency of the 0.4 THz

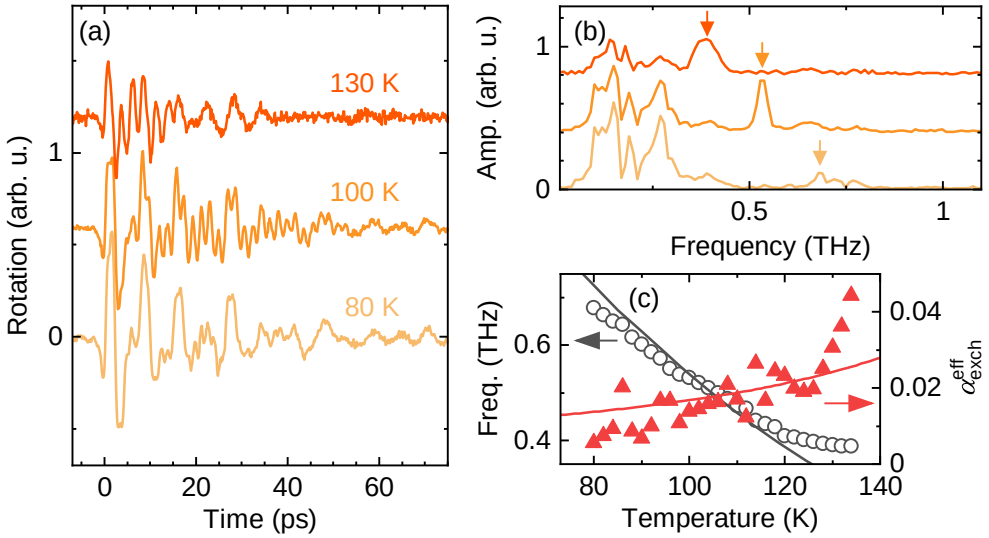

Figure 4.4: Temperature dependence of the Gd-Fe exchange mode. (a) THz-induced polarization rotation for 80 K, 100 K, and 130 K, offset for better visibility. (b) Fourier spectra of the time traces from panel (a), the arrows indicate the exchange mode, offset for better visibility. (c) The frequency (black circles) and the effective damping (red triangles) of the exchange mode as a function of temperature. Both values are extracted with a Lorentzian function fit to the exchange mode peak. The black line shows a fit based on the Kaplan-Kittel exchange resonance formula (see Eq. S5) [5] with the molecular field parameter $N_{\text{Gd-Fe}} = -0.80 \frac{\text{mol}}{\text{cm}^3}$. The red line is a fit with $\alpha^{\text{eff}}_{\text{exch}} = \alpha^{\text{eff}} \left(|\vec{M}_{\text{Gd}}| + |\vec{M}_{\text{Fe}}|\right) / \left(|\vec{M}_{\text{Gd}}| - |\vec{M}_{\text{Fe}}|\right)$ [45] with the constant effective Gilbert damping factor of the sublattices $\alpha^{\text{eff}} = 0.0046$.

peak at 130 K increases to 0.7 THz upon lowering the temperature down to 80 K. The extracted peak position with a temperature step of 2 K is shown in Fig. 4.4(c), in an excellent agreement with the temperature dependence observed for the exchange resonance between the Gd and Fe sublattices [46]. The positions of the other visible peaks in Fig. 4.4(b) that do not change with temperature within our measurement accuracy, are consistent with the 1st and the 2nd cavity modes in Fig. 4.3(b). Therefore, they can convincingly be attributed to the forced response of the spin system to the THz pulse, shaped by multiple reflections at GdBIG surfaces. Moreover, the cavity modes modify the observable line-width of the magnetic resonance, thereby enabling

control of the apparent effective damping of the exchange mode, $\alpha_{\text{exch}}^{\text{eff}}$. The apparent change in damping results from the recurrent parametric excitation of the spin system by a phase-matched sequence of the THz pulses within the cavity. The extracted line-width of the exchange mode at every temperature is shown in Fig. 4.4(c). The value of $\alpha_{\text{exch}}^{\text{eff}}$ varies from 0.007 to 0.04 in the observed temperature range. This is almost one order of magnitude lower than previously reported measurements on similar compounds. With a non-resonant excitation the intrinsic damping of the exchange mode was shown to be from 0.05 to 0.1 [47]. Rigorous estimation of the enhancement is challenging due to limitations in frequency resolution and the low finesse of the cavity. However, we observed that the enhancement is consistent with the finesse, measuring 5-6 in our experiment.

Controlling the exchange mode necessitates understanding the underlying excitation mechanism. To this end, the THz field strength dependence of the induced magnetization dynamics was analyzed. As illustrated in Fig. 4.5 (a), the amplitude scales linearly with the strength of the THz field. Moreover, the change of exchange mode amplitude with changing THz field polarization β, where $\beta = \angle(\vec{M}, \vec{H}_{\text{THz}})$, shown in Fig. 4.5(b), reveals a sine-like dependence. The two observed maxima at $\beta = 90^\circ$ and $\beta = -90^\circ$ are in agreement with the linear Zeeman torque excitation mechanism [37].

Taking advantage of the high tunability of the exchange mode with temperature, we analyzed its coupling with the cavity modes and their influence on the resulting spin dynamics. Figure 4.5(c) shows the amplitude of the exchange mode as a function of its frequency, where each data point corresponding to a distinct temperature. Although the net magnetic moment of GdBIG significantly decreases as the temperature approaches the compensation point $T_{\text{comp}} = 223$ K [27], this monotonic trend does not account for the observed periodic behavior. However, consistent with the Zeeman torque excitation mechanism, the amplitude of the exchange mode linearly depends on the THz field strength. To illustrate this, we present the spectrum of the magnetic field of the transmitted THz pulse, $H_{\text{THz}} \propto E_{\text{Sam}}$, measured with

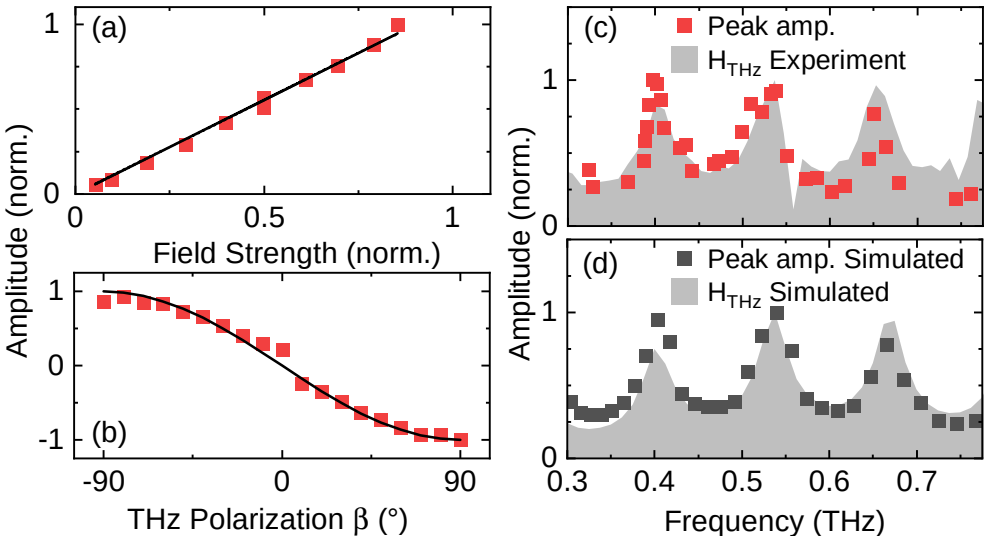

Figure 4.5: THz light - exchange mode coupling mechanism. The exchange mode amplitude as a function of THz pulse field strength (a) and THz field polarization (b). These measurements were performed at a temperature of 100 K. The solid lines are the expected dependencies for a Zeeman excitation mechanism. (c) Amplitude of the exchange mode as function of its frequency. The spectrum of the transmitted pulse train corresponding to the magnetic field of the THz pulse H_{THz} is shown as a gray background. (d) Amplitude of the exchange mode as function of its frequency derived from the simulations (see Sec. 4.2.4). The simulated excitation spectrum of H_{THz} is shown as a gray background.

EOS at 100 K, shown as a gray background in Fig. 4.5(c). Indeed, the exchange mode amplitude increases twofold when its frequency matches one of the cavity resonances.

4.2.4 Theoretical Analysis and Discussion

To understand the THz-induced magnetization dynamics in the presence of cavity modes, we employ the modified Landau–Lifshitz–Gilbert equation formalism. Taking into account the dominant role of the iron-iron exchange, the magnetization dynamics can be described by coupled equations for a

two-sublattice ferrimagnet [48]:

$$\frac{d\vec{M}_{\mathrm{i}}}{dt} = -(\mu_0\gamma_{\mathrm{i}})\left[\vec{M}_{\mathrm{i}} \times \vec{H}_{\mathrm{i}}^{\mathrm{eff}}\right] - (\mu_0\gamma_{\mathrm{i}})\frac{\alpha_{\mathrm{i}}}{|\vec{M}_{\mathrm{i}}|}\vec{M}_{\mathrm{i}} \times \left[\vec{M}_{\mathrm{i}} \times \vec{H}_{\mathrm{i}}^{\mathrm{eff}}\right] \tag{4.9}$$

with μ_0 the vacuum magnetic permeability, M_{i} the net magnetizations, γ_{i} the gyromagnetic ratios, and α_{i} the Gilbert damping factors of the Gd and Fe sublattice dynamics. $\vec{H}_{\mathrm{i}}^{\mathrm{eff}}$ is the effective magnetic field defined as

$$\vec{H}_{\mathrm{Gd,Fe}}^{\mathrm{eff}} = \vec{H}_{\mathrm{app}} + \vec{H}_{\mathrm{THz}} - N_{\text{Gd-Fe}}\vec{M}_{\mathrm{Fe,Gd}}. \tag{4.10}$$

Here, the first term with $\mu_0\vec{H}_{\mathrm{app}} = 150$ mT represents the applied external magnetic field, $\vec{H}_{\mathrm{THz}}$ denotes the THz pulse magnetic field, and $N_{\text{Gd-Fe}}$ the effective Gd-Fe exchange parameter. To model the impact of the cavity, we introduce multiple delayed THz pulses so that the temporal profile of the THz stimulus closely follows the experimentally observed transmitted field E_{Sam} in Fig. 4.3(b) at 100 K. A comparison of the simulated and measured THz waveforms and spectra is presented in Fig. 4.7(a,b) of the Appendix B.

The exchange field which is responsible for the coupling of the two sublattices, is represented by the last term in Eq. 4.10. It is worth noting that the two-sublattice model fails to account for the temperature dependence of the effective Gd-Fe coupling. Instead, a three-sublattice model should be considered where the two Fe magnetizations are treated separately (see Appendix C). Moreover, by applying the three-sublattice model, the connection between $N_{\text{Gd-Fe}}$ and parent molecular field coefficients can be derived. From fitting the temperature dependence of the exchange mode frequency with the Kaplan-Kittel model [5], we obtain $N_{\text{Gd-Fe}}$ = -0.89 $\frac{\mathrm{mol}}{\mathrm{cm}^3}$, which is in a good agreement with the value derived from the SQUID data [46]. Away from the compensation point $T_{\mathrm{comp}} = 223$ K it is safe to assume that the Gilbert damping factors $\alpha_{\mathrm{Fe}} = \alpha_{\mathrm{Gd}} = \alpha$ [45] and almost temperature independent [47], while their values were set to 0.03 based on the previous measurements on this sample [27] and $\gamma_{\mathrm{Fe}} \approx \gamma_{\mathrm{Gd}} = \gamma = 28\frac{\mathrm{GHz}}{\mathrm{T}}$ [48].

By numerically solving Eqs. (1) using the Euler method, the magnetization dynamics of the sublattices was extracted. To compare the simulation results with the experiment it is important to note that the Faraday rotation at 800 nm, in our experimental geometry, is mostly sensitive to the magnetization of the iron sublattice in GdBIG [27]. Figure 4.7(c) shows the simulated and experimentally observed THz-induced magnetization dynamics at 100 K. Both time scans show a fast oscillation attributed to the exchange mode dynamics. The experimental scan has an additional low frequency component that is not captured by our simulations. However, the simulation does not take into account propagation effects and dispersion of the sample, therefore an exact match is not expected. Simulating temperature changes by varying the sublattice magnetizations allows us to extract the amplitude and the frequency of the exchange mode shown in Fig. 4.5(d). The gray background illustrates the spectrum of the applied THz magnetic field H_{THz}. Similar to the experiment, the amplitude of the exchange mode is enhanced when its frequency coincides with the cavity modes created by the sample interfaces.

We believe that the concept of driving high-frequency spin dynamics with a THz pulse train in a cavity formed by the crystal interfaces can be further explored. For example, we suggest a sandwich structure consisting of a THz generation crystal and a ferrimagnet capped by optically transparent and highly THz reflective interfaces. The progress in THz coating makes it possible to achieve very high reflection coefficients, which accentuate the action of the THz pulse train on the medium. For example, indium–tin–oxide-coated glass has THz amplitude reflection coefficient r as high as 0.9 [49], while using THz Bragg mirrors this value potentially can reach 0.99 [50]. This is substantially higher than that obtained in a bare GdBIG crystal with Fresnel reflection at interfaces, where we estimate $r = 0.7$. To study the impact of interface reflection, we simulate THz-induced magnetization dynamics with $r = 0.95$ and plot the amplitude as a function of the frequency of the exchange mode in Fig. 4.8(a). A much higher dynamical range of the mode amplitude variations is observed, while $\alpha^{\mathrm{eff}}_{\mathrm{exch}}$ can be further reduced by fourfold. This is illustrated in Fig. 4.8(b) by comparing magnetization dynamics waveforms

at a temperature of 128 K. Moreover, in conjunction with using ferrimagnets with much lower intrinsic damping, e.g., yttrium iron garnet [51], exchange mode coupling with THz light might even enter the strongly coupled regime [52, 53].

4.2.5 Conclusion

In conclusion, we investigated the coupling between light at THz frequencies and the Gd-Fe spin exchange mode in GdBIG using THz-pump optical-probe measurements. We show that tuning the exchange mode into a resonance with the cavity modes strongly enhances the efficiency of the THz excitation of high-frequency spin dynamics. The excitation mechanism is attributed to the Zeeman torque. Moreover, the cavity reduces the effective damping of the exchange mode 5-fould. The results are analyzed by means of numerical simulations based on a system of coupled Landau-Lifshitz-Gilbert equations which show a good agreement with the experimental observations. A three-subsystem approach developed here for the first time allowed to conclude that the effective Gd-Fe molecular field strength exhibits no variations in the 70-130 K temperature range. This work improves the understanding of efficient control of the exchange modes at THz frequencies. Furthermore, it opens an intuitively clear and uncomplicated path to achieve strong coupling between light and sub-THz exchange modes by means of designing the effictive interfaces of a magnetic material.

The supporting data and codes for this article are available from Zenodo [54].

Acknowledgments

We thank T. Satoh for providing the samples and fruitful discussions. The work in Cologne was partially supported by the DFG via Project No. 277146847

— Collaborative research Center 1238: Control and Dynamics of Quantum Materials (Subproject No. B05).

4.2.6 Appendix

Raman Measurement

The Raman spectrum was recorded by a triple-grating spectrometer using a 532 nm continuous wave laser in backscattering geometry at a power of 1 mW on the sample. The direction of polarisation of the analysed light was parallel to that of the incoming beam. The Raman spectrum in the relevant spectral range is shown in Fig. 4.6.

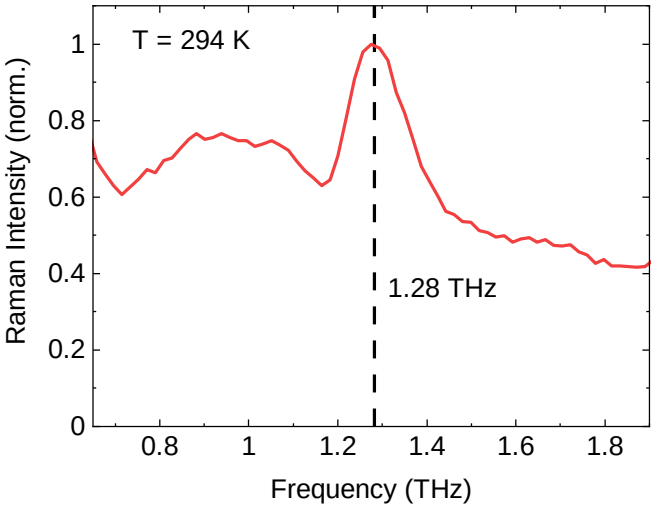

Figure 4.6: Raman intensity measured on GdBIG in parallel polarization configuration at room temperature.

Modeling of THz Magnetic Field

To model the THz pulse magnetic field H_{THz}, we used sequences of pulses defined as

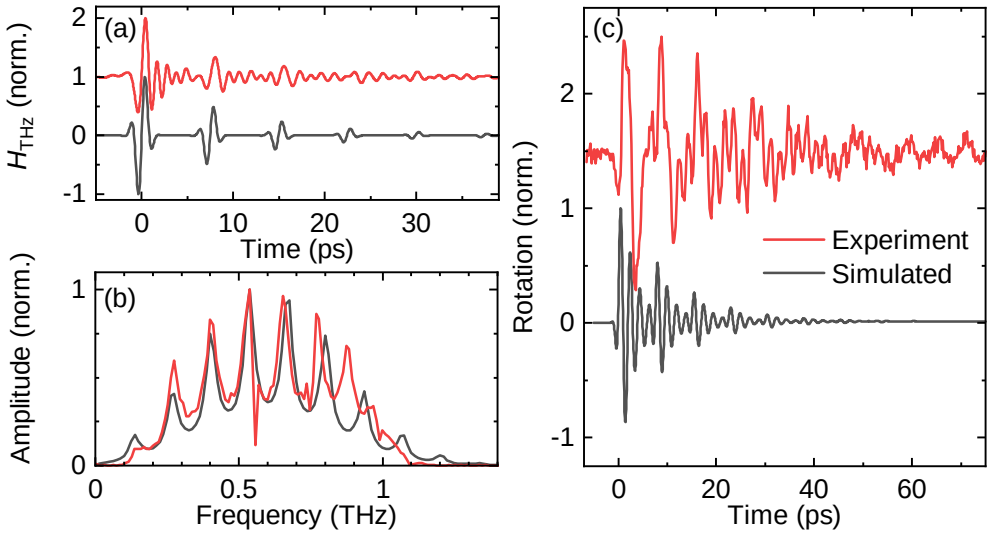

Figure 4.7: (a) Magnetic THz field applied in the simulation compared to the experimentally measured THz field transmitted through the sample at 100 K. (b) Corresponding Fourier spectra. (c) Comparison of the THz-induced magnetization dynamics in the sample between experiment and simulation at 100 K.

$$H_{\mathrm{THz}}(t) = \sum_{k=0}^{N} H_0 \cdot r^{2k} \sin(\omega_0 t - k \cdot \omega_0 \tau) \cdot e^{-(t-k\cdot\tau)^2/2\sigma^2}, \tag{4.11}$$

with H_0 the magnetic field amplitude, ω_0 the center frequency, σ the pulse duration, N the number of reflections, r amplitude reflection coefficient at the crystal interface, and τ the time delay introduced by propagation in the medium. To follow the shape of the THz pulse used in the experiment we choose $\mu_0 H_0 = 0.266$ T, $\omega_0/2\pi = 0.6$ THz, and $\sigma = 0.63$ ps. The coefficients r and τ are calculated using a constant refractive index of $n = 5.6$ extracted from the THz-TDS measurements in Fig. 4.3. $N = 10$ is selected to ensure that all reflections within the chosen time window are accounted for. Figure 4.7(a) shows the resulting sequences of THz pulses compared to the THz electric field measured with EOS after transmitting through the sample at 100 K. A very good agreement of the corresponding spectra is also evident,

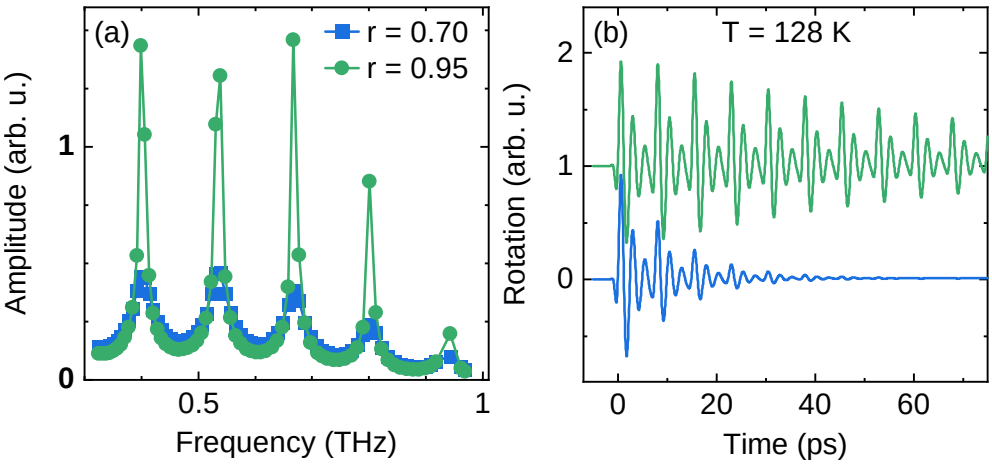

Figure 4.8: (a) Numerical simulation of the behavior of the exchange mode amplitude as a function of its frequency with two different reflection coefficients at the interface. (b) THz-induced magnetization dynamics modeled with the reflection coefficient $r = 0.7$ (bottom curve) and $r = 0.95$ (top curve).

see Fig. 4.7(b). To compare the THz-induced magnetization dynamics with that observed in the experiment we plot the out-of-plane component of $\vec{M}_{\mathrm{Fe}}$ in Fig. 4.7(c).

This approach allows for the testing of different paths to optimize the excitation efficiency of the exchange mode. Figure 4.8 shows the simulation results of THz-induced spin dynamics with the reflection coefficients at the interfaces of $r = 0.95$. The other parameters are kept the same. It is seen that improving the cavity finesse up to 60 results in a threefold enhancement of the dynamic range of the spin exchange mode peak amplitude (green circles).

Effective Exchange Constant

Rare earth iron garnets are typically considered two-sublattice magnets. This assumption is based on the fact that the molecular field coefficient $\mathrm{N_{ad}}$, which accounts for the interaction between iron at the octahedral and tetrahedral sites, is much larger than the iron-rare earth (rare earth is indexed by "c") molecular field coefficients $\mathrm{N_{cd}}$ and $\mathrm{N_{ca}}$ [55]. For that reason, the majority of

recent papers do not address the connection between the effective coupling constant $N_{\text{Gd-Fe}}$ and the three-sublattice molecular field coefficients. However, this assumption potentially overlooks the temperature dependence of the effective coupling constant [56]. Considering a three-sublattice model instead provides an additional way to estimate $N_{\text{Gd-Fe}}$ by analysing SQUID data in combination with molecular field theory. The main steps for deriving $N_{\text{Gd-Fe}}$ are provided below.

To address the dynamics of a three-sublattice magnet, we write three Landau–Lifshitz equations assuming no damping for simplicity:

$$\begin{aligned}
\frac{d\vec{M}_{\text{a}}}{dt} &= -(\mu_0\gamma_{\text{Fe}})\left[\vec{M}_{\text{a}} \times \left(\vec{H}_{\text{THz}} - N_{\text{ad}}\vec{M}_{\text{d}} - N_{\text{ac}}\vec{M}_{\text{c}}\right)\right] \\
\frac{d\vec{M}_{\text{d}}}{dt} &= -(\mu_0\gamma_{\text{Fe}})\left[\vec{M}_{\text{d}} \times \left(\vec{H}_{\text{THz}} - N_{\text{da}}\vec{M}_{\text{a}} - N_{\text{dc}}\vec{M}_{\text{c}}\right)\right] \\
\frac{d\vec{M}_{\text{c}}}{dt} &= -(\mu_0\gamma_{\text{Gd}})\left[\vec{M}_{\text{c}} \times \left(\vec{H}_{\text{THz}} - N_{\text{ca}}\vec{M}_{\text{a}} - N_{\text{cd}}\vec{M}_{\text{d}}\right)\right]
\end{aligned} \tag{4.12}$$

Then, we look for a solution in the form $\vec{M}_i = \vec{M}_i^{\text{init}} + \vec{m}_i e^{i2\pi ft}$, where $\vec{M}_i^{\text{init}}$ are the ground state magnetizations, $\vec{m}_i$ are the corresponding perturbations, and i corresponds to the indices a, d and c. We assume that all magnetizations are collinearly aligned in a ground state, note that $N_{\text{ad}} = N_{\text{da}}$, $N_{\text{ca}} = N_{\text{ac}}$, and $N_{\text{cd}} = N_{\text{dc}}$, take into account terms only linear on $\vec{m}_i$ and exclude terms of the second order on N_{ac} and N_{dc}. Then, the Gd-Fe exchange frequency can be found:

$$\begin{aligned}
f_{\text{Gd-Fe}} = &\frac{\mu_0\gamma}{2}\left[N_{\text{ad}}\left(M_d - M_a\right) - N_{\text{ac}}\left(M_a + M_c\right) + N_{\text{dc}}\left(M_d - M_c\right)\right] \\
&- \frac{\mu_0\gamma}{2}\left[N_{\text{ad}}^2\left(M_a^2 + M_d^2 - 2M_aM_d\right)\right. \\
&-2N_{\text{ac}}N_{\text{ad}}\left(M_a^2 + M_aM_c - M_aM_d + M_cM_d\right) \\
&\left.-2N_{\text{ad}}N_{\text{dc}}\left(M_d^2 - M_aM_d - M_aM_c - M_cM_d\right)\right]^{1/2}
\end{aligned} \tag{4.13}$$

$$f_{\text{Gd-Fe}} = \frac{\mu_0\gamma}{2}\left[N_{\text{ad}}\left(M_d - M_a\right) - N_{\text{ac}}\left(M_a + M_c\right) + N_{\text{dc}}\left(M_d - M_c\right)\right] - \frac{\mu_0\gamma}{2}N_{\text{ad}}\left(M_d - M_a\right)\left[1 - 2\left(\frac{N_{\text{ac}}}{N_{\text{ad}}}\right)\frac{M_a^2 + M_aM_c - M_aM_d + M_cM_d}{M_a^2 + M_d^2 - 2M_aM_d} - 2\left(\frac{N_{\text{dc}}}{N_{\text{ad}}}\right)\frac{M_d^2 - M_aM_d - M_aM_c - M_cM_d}{M_a^2 + M_d^2 - 2M_aM_d}\right]^{1/2} \tag{4.14}$$

Given that the iron-iron exchange interaction considerably exceeds the rare earth-iron exchange interaction, N_{ac}, $N_{\text{dc}} << N_{\text{ad}}$, the last two terms inside the square root in Eq. 4.14 represent a small parameter to which a Taylor expansion can be applied. This results in

$$f_{\text{Gd-Fe}} = -(\mu_0\gamma)N_{\text{Gd-Fe}}\left|M_{\text{d}} - M_{\text{a}} - M_{\text{Gd}}\right|; \tag{4.15}$$

$$N_{\text{Gd-Fe}} = -\frac{N_{\text{cd}}M_{\text{d}} + N_{\text{ca}}M_{\text{a}}}{M_{\text{d}} - M_{\text{a}}}. \tag{4.16}$$

Equation 4.16 clearly shows that since the magnetizations $\vec{M}_{\text{d}}$ and $\vec{M}_{\text{a}}$ are temperature-dependent, the effective Gd-Fe exchange coupling also exhibits temperature dependence when the three-sublattice model is considered. Substituting molecular field coefficients N_{cd} = 6 $\frac{\text{mol}}{\text{cm}^3}$ and N_{ca} = -3.44 $\frac{\text{mol}}{\text{cm}^3}$ from [4] gives estimation of $N_{\text{Gd-Fe}}$ changing in the range from -0.89 to -0.90 $\frac{\text{mol}}{\text{cm}^3}$ in the studied temperature range from 80 to 130 K.

Contributions

Evgeny Mashkovich conceived the project. The THz-TDS, TPOP measurements and LLG simulations were performed by Chris Reinhoffer. Evgeny Mashkovich calculated the results for the three sublattices solution. Philipp Stein performed the Raman measurements. Chris Reinhofffer, Semyon Germansky, Evgeny Mashkovich, Andrzej Stupakiewicz, Ilya Razdolskiy, and Paul van Loosdrecht helped with the discussion and analysis of the experimental results. Chris Reinhoffer wrote the main part of the manuscript in

collaboration with Evgeny Mashkovich. All mentioned authors helped with refining the final written manuscript.

References

1. Wolfgang Demtröder. *Experimentalphysik 1* 7th ed. XVI, 472. ISBN: 978-3-662-46415-1 (Springer Spektrum Berlin, Heidelberg, 2015).
2. Larmor, J. LXIII. On the theory of the magnetic influence on spectra; and on the radiation from moving ions. *The London, Edinburgh, and Dublin Philosophical Magazine and Journal of Science* **44,** 503–512 (1897).
3. Gross, R. & Marx, A. in *Festkörperphysik* (De Gruyter Oldenbourg, 2022). ISBN: 978-3-11-078239-4.
4. Parchenko, S. *Laser-induced spin dynamics in multisublattice ferrimagnetic dielectrics* PhD thesis (2016).
5. Kaplan, J. & Kittel, C. Exchange Frequency Electron Spin Resonance in Ferrites. *The Journal of Chemical Physics* **21,** 760–761 (1953).
6. Hsu, W.-H. *et al.* Observation of terahertz magnon of Kaplan-Kittel exchange resonance in yttrium-iron garnet by Raman spectroscopy. *Physical Review B* **102,** 174432 (2020).
7. Princep, A. J. *et al.* The full magnon spectrum of yttrium iron garnet. *npj Quantum Materials* **2,** 1–5 (2017).
8. E. P. Wohlfarth. *Ferromagnetic materials. 2* 3. impr. 592 pp. ISBN: 978-0-444-85312-7 (North-Holland, Amsterdam, 1999).
9. *Femtosecond Laser Pulses* (ed Claude Rullière) 2nd ed. (Springer New York, New York, 2004). XVI, 426. ISBN: 978-0-387-01769-3.
10. *Springer Handbook of Lasers and Optics* (ed Frank Träger) 1st ed. (Springer New York, New York, 2007). XXVI, 1332. ISBN: 978-0-387-95579-7.

11. Aparnadevi, N. *et al.* Structural properties, optical, electrical and magnetic behavior of bismuth doped $Gd_3Fe_5O_{12}$ prototype garnet. *Journal of Materials Science: Materials in Electronics* **31,** 2081–2088 (2020).

12. Nakamoto, R. *et al.* Properties of rare-earth iron garnets from first principles. *Physical Review B* **95,** 024434 (2017).

13. *Handbook of Ferromagnetic Materials* (ed E.P Wohlfarth) 1st ed. (North-Holland Publishing Company, 1980). 592 pp. ISBN: 978-0-444-85312-7.

14. Wang, L.-W. *et al.* First-principles study of magnon-phonon interactions in gadolinium iron garnet. *Physical Review B* **101,** 165137 (2020).

15. Ng, I. *et al.* Survey of Temperature Dependence of the Damping Parameter in the Ferrimagnet $Gd_3Fe_5O_{12}$. *IEEE Transactions on Magnetics* **58,** 1–6 (2022).

16. Hansen, P. & Krumme, J. P. Magnetic and magneto-optical properties of garnet films. *Thin Solid Films. Special Issue on Magnetic Garnet Films* **114,** 69–107 (1984).

17. Ajani, S. N. *et al.* Advancements in Computing: Emerging Trends in Computational Science with Next-Generation Computing. *International Journal of Intelligent Systems and Applications in Engineering* **12,** 546–559 (2024).

18. Markov, I. L. Limits on fundamental limits to computation. *Nature* **512,** 147–154 (2014).

19. Wadley, P. *et al.* Electrical switching of an antiferromagnet. *Science* **351,** 587–590 (2016).

20. Pirro, P. *et al.* Advances in coherent magnonics. *Nature Reviews Materials* **6,** 1114–1135 (2021).

21. Li, S. *et al.* Light-Controlled Ultrafast Magnetic State Transition in Antiferromagnetic–Ferromagnetic van der Waals Heterostructures. *The Journal of Physical Chemistry Letters* **13,** 6223–6229 (2022).

22. Grishunin, K. *et al.* Excitation and detection of terahertz coherent spin waves in antiferromagnetic α-Fe_2O_3. *Physical Review B* **104,** 024419 (2021).

23. Qin, H. *et al.* Nanoscale magnonic Fabry-Perot resonator for low-loss spin-wave manipulation. *Nat Commun* **12** (2021).

24. Song, C. *et al.* How to manipulate magnetic states of antiferromagnets. *Nanotechnology* **29,** 112001 (2018).

25. Mak, K. F., Shan, J. & Ralph, D. C. Probing and controlling magnetic states in 2D layered magnetic materials. *Nature Reviews Physics* **1,** 646–661 (2019).

26. Sriram, A. & Claassen, M. Light-induced control of magnetic phases in Kitaev quantum magnets. *Physical Review Research* **4,** L032036 (2022).

27. Parchenko, S. *et al.* Non-thermal optical excitation of terahertz-spin precession in a magneto-optical insulator. *Applied Physics Letters* **108,** 032404 (2016).

28. Parchenko, S. *et al.* Wide frequencies range of spin excitations in a rare-earth Bi-doped iron garnet with a giant Faraday rotation. *Applied Physics Letters* **103,** 172402 (2013).

29. Mashkovich, E. A. *et al.* Terahertz-driven magnetization dynamics of bismuth-substituted yttrium iron-gallium garnet thin film near a compensation point. *Physical Review B* **106,** 184425 (2022).

30. Metzger, T. W. J. *et al. Impulsive Fermi magnon-phonon resonance in antiferromagnetic CoF_2* 2023. arXiv: 2308.01052.

31. Hansen, P., Röschmann, P. & Tolksdorf, W. Saturation magnetization of gallium-substituted yttrium iron garnet. *Journal of Applied Physics* **45,** 2728–2732 (1974).

32. Takeuchi, H. The Faraday Effect of Bismuth Substituted Rare-Earth Iron Garnet. *Japanese Journal of Applied Physics* **14,** 1903 (1975).

33. Blank, T. *et al.* THz-Scale Field-Induced Spin Dynamics in Ferrimagnetic Iron Garnets. *Physical Review Letters* **127,** 037203 (2021).

34. Zhang, X. *et al.* Strongly Coupled Magnons and Cavity Microwave Photons. *Physical Review Letters* **113,** 156401 (2014).

35. Jarc, G. *et al.* Tunable cryogenic terahertz cavity for strong light–matter coupling in complex materials. *Review of Scientific Instruments* **93,** 033102 (2022).

36. Blank, T. G. H., Grishunin, K. A. & Kimel, A. V. Magneto-optical detection of terahertz cavity magnon-polaritons in antiferromagnetic $HoFeO_3$. *Applied Physics Letters* **122,** 072402 (2023).

37. Kampfrath, T. *et al.* Coherent terahertz control of antiferromagnetic spin waves. *Nature Photonics* **5,** 31–34 (2011).

38. Deb, M. *et al.* Controlling High-Frequency Spin-Wave Dynamics Using Double-Pulse Laser Excitation. *Phys. Rev. Appl.* **18,** 044001 (4 2022).

39. Hirori, H. *et al.* Single-cycle terahertz pulses with amplitudes exceeding 1 MV/cm generated by optical rectification in $LiNbO_3$. *Applied Physics Letters* **98,** 091106 (2011).

40. Wu, Q. & Zhang, X. Free-space electro-optic sampling of terahertz beams. *Applied Physics Letters* **67,** 3523–3525 (1995).

41. Sievers, A. J. & Tinkham, M. Far Infrared Spectra of Rare-Earth Iron Garnets. *Physical Review* **129,** 1995–2004 (1963).

42. Grunberg, P., Koningstein, J. A. & Uitert, L. G. V. Optical Phonons in Iron Garnets. *JOSA* **61,** 1613–1617 (1971).

43. J. Michael Hollas. *Modern Spectroscopy* 4th ed. ISBN: 978-0-470-84416-8 (John Wiley & Sons, 2003).

44. Kumar, P. *et al.* Second harmonic generation study of internally-generated strain in bismuth-substituted iron garnet films. *Optics Express* **18,** 1076–1084 (Jan. 18, 2010).

45. Schlickeiser, F. *et al.* Temperature dependence of the frequencies and effective damping parameters of ferrimagnetic resonance. *Phys. Rev. B* **86,** 214416 (21 2012).

46. Stupakiewicz, A. & Satoh, T. Ultrafast Optomagnonics in Ferrimagnetic Multi-Sublattice Garnets. *Journal of the Physical Society of Japan* **90,** 081008 (2021).

47. Deb, M., Molho, P. & Barbara, B. Magnetic damping of ferromagnetic and exchange resonance modes in a ferrimagnetic insulator. *Phys. Rev. B* **105,** 014432 (1 2022).

48. Geschwind, S. & Walker, L. R. Exchange Resonances in Gadolinium Iron Garnet near the Magnetic Compensation Temperature. *Journal of Applied Physics* **30,** S163–S170 (Apr. 1959).

49. Bauer, T. *et al.* Indium–tin–oxide-coated glass as dichroic mirror for far-infrared electromagnetic radiation. *Journal of Applied Physics* **92,** 2210–2212 (Aug. 2002).

50. Yu, Y. *et al.* Fabrication and characterization of a wide-bandgap and high-Q terahertz distributed-Bragg-reflector micro cavities. *Optics Communications* **426,** 84–88 (2018).

51. Cherepanov, V., Kolokolov, I. & L'vov, V. The saga of YIG: Spectra, thermodynamics, interaction and relaxation of magnons in a complex magnet. *Physics Reports* **229,** 81–144 (1993).

52. Białek, M. *et al.* Strong Coupling of Antiferromagnetic Resonance with Subterahertz Cavity Fields. *Phys. Rev. Appl.* **15,** 044018 (4 2021).

53. Huebl, H. *et al.* High Cooperativity in Coupled Microwave Resonator Ferrimagnetic Insulator Hybrids. *Phys. Rev. Lett.* **111,** 127003 (12 2013).

54. Reinhoffer, C. *et al. Data and code for "THz Control of Exchange Mode in a Ferrimagnetic Cavity"* 2024.

55. Dionne, G. F. Molecular Field and Exchange Constants of Gd3+- Substituted Ferrimagnetic Garnets. *Journal of Applied Physics* **42,** 2142–2143 (Apr. 1971).

56. Clark, A. E. & Callen, E. Néel Ferrimagnets in Large Magnetic Fields. *Journal of Applied Physics* **39,** 5972–5982 (Dec. 1968).

Summary

The main objective of this thesis is using high intensity terahertz (THz) pulses to excite, discover, and understand previously unknown physical phenomena in different classes of materials. In the process of this thesis the strongly correlated transition metal oxide (Sr,Ca)RuO_3, the two band superconductor MgB_2 and the ferrimagnetic garnet $(Gd,Bi)_3Fe_5O_{12}$ are investigated. For that purpose, the relatively new field of THz harmonic-generation (HG) spectroscopy and the more established THz-pump optical-probe (TPOP) experiments are used. Furthermore, THz time-domain spectroscopy (THz-TDS) as a method for material characterization is utilized.

In the case of (Sr,Ca)RuO_3 it is predicted that an itinerant-electron system close to a magnetic quantum critical point should show a universal nonlinear conductivity. Such a nonlinearity would give rise to harmonic generation when applying an ac field. First, THz HG is measured in $CaRuO_3$, as it is a prime candidate material for the proposed phenomenon. A remarkably strong third harmonic generation (THG) is observable at low temperatures. The frequency dependence suggests that this phenomenon is influenced by electron transport, and the temperature dependence corresponds to the formation of coherent heavy quasiparticles observed in ARPES measurements on $CaRuO_3$. These two observations in combination enable a numerical description of the THz HG in $CaRuO_3$ using a Boltzmann transport model capturing the key observations. Next, different chemical compositions of (Sr,Ca)RuO_3 are studied using THz HG and THz-TDS. The THz-TDS measurements show no unexpected behavior in their temperature dependence speaking for the comparability of the samples with other samples measured in literature. All investigated samples show THG making a process based

purely on the quantum critical nature of $CaRuO_3$ unlikely. Furthermore, the temperature dependence in the four investigated samples is identical suggesting a common origin of the nonlinearity with $CaRuO_3$. However, the fluence dependence shows non-perturbative character with a power law of 2.5 similar to the one observed for materials with linear dispersion. Linear dispersion is known to strongly influence the low temperature conduction properties of $SrRuO_3$ and is predicted for $CaRuO_3$ as well. Whether coherent heavy quasiparticles or linear dispersion, our measurements point to a common origin in the ground state transport properties of (Sr,Ca)RuO_3.

The two band superconductor MgB_2, as currently the BCS superconductor with the highest T_c at ambient pressures, lends itself to investigate phenomena based on the superconducting ground state. One such phenomenon is the Higgs mode, an oscillation of the collective superconducting amplitude, predicted to exist as a consequence of the BCS ground state. THG has been shown to be a valid probe of the Higgs mode in MgB_2, enabling the investigation of the BCS state contactless and on ultrafast time scales. This is used as a basis to extend the knowledge to higher harmonic generation and behavior in an applied magnetic field. MgB_2 shows fifth harmonic generation in the superconducting state matching the resonance condition observed for the THG and connecting it to the lower energy band in MgB_2. Furthermore, a pseudospin analysis shows the validity of this interpretation. The measurements of the THG in an applied magnetic field reinforce the connection to the superconducting ground state. For an increasing applied field the onset of THG is observed at lower temperatures matching the measured phase diagram for MgB_2. Additionally, THG is observed at the onset of the superconducting state forming, before the zero resistance state is established, demonstrating the versatility of this approach in probing the superconductors.

As a ferrimagnet, $(Gd,Bi)_3Fe_5O_{12}$ (GdBIG) is host to a high frequency exchange mode in the THz range combined with a net nonzero magnetization, simplifying the investigation of magnetization dynamics. Furthermore, as a single crystalline sample with thicknesses in the hundreds of micrometers,

the same length scale as THz wavelengths, physical effects seen in cavities can strongly influence the response to a THz pump pulse. TPOP measurements with the optical probe measuring the THz induced polarization rotation reveal two phenomena. First, the magnetization dynamics show multiple modes that are not eigenmodes of the spin system but are eigenmodes of the cavity created by the sample interfaces. These modes forces the magnetization of GdBIG to follow, allowing for the detection with an external probe. Second, the exchange mode is observed to be of highly tunable nature with its amplitude oscillating with temperature. The excitation mechanism is found to be Zeeman torque using polarization and fluence dependent measurements. The excitation is linearly dependent on the magnetic field strength and is maximized with the magnetic field applied orthogonal to the sample magnetization. Furthermore, a numeric simulation of the exchange mode temperature dependence using coupled Landau–Lifshitz–Gilbert equations reveals the temperature oscillation of the exchange mode to be a product of its overlap with cavity eigenmodes of the system. These measurements show that by carefully choosing the properties of a system, these properties can be combined to enhance the resulting response.

Zusammenfassung

Das Hauptziel dieser Doktorarbeit ist die Verwendung hochintensiver Terahertz (THz) - Pulse zur Anregung, Entdeckung und zum Verständis bisher unbekannter physikalischer Phänomene in verschiedenen Materialklassen. Zu diesem Zweck werden das relativ neue Gebiet der THz harmonischen Generation (HG) und das etabliertere mit THz-Pulsen anregen und mit optischen Pulsen abfragen (TPOP) genutzt. Darüber hinaus wird die THz - Zeitbereichsspektroskopie (THz-TDS) als Methode zur Materialcharakterisierung genutzt. Im Rahmen dieser Arbeit werden das Übergangsmetalloxid (Sr,Ca)RuO_3 mit starker Wechselwirkung zwischen den Elektronen, der Zweibandsupraleiter MgB_2 und das isolierende und ferrimagnetische Granat $(Gd,Bi)_3Fe_5O_{12}$ untersucht.

Im Fall von (Sr,Ca)RuO_3 wird vorhergesagt, dass ein itinerantes Elektronensystem in der Nähe eines magnetischen quantenkritischen Punktes eine universelle nichtlineare Leitfähigkeit aufweisen sollte. Eine solche Nichtlinearität würde beim Anlegen eines Wechselstromfeldes zur Erzeugung von Harmonischen führen. Zunächst wird THz HG in $CaRuO_3$ gemessen, da dieses Material ein ausgezeichneter Kandidat für diese Phänomene ist. Eine bemerkenswert starke Erzeugung der dritten Harmonischen (THG) ist bei nie- drigen Temperaturen zu beobachten. Die Frequenzabhängigkeit deutet darauf hin, dass dieses Phänomen durch den Transport beeinflusst wird, und die Temperaturabhängigkeit stimmt mit der Bildung kohärenter schwerer Quasiteilchen überein, die bei ARPES-Messungen an $CaRuO_3$ beobachtet wur- de. Diese Kombination ermöglicht eine numerische Beschreibung der THz HG in $CaRuO_3$ unter Verwendung eines Boltzmann-Transportmodells,

das die wichtigsten Beobachtungen erfasst. Als nächstes werden verschiedene chemische Zusammensetzungen von (Sr,Ca)RuO_3 mit THz HG und THz-TDS untersucht. Die THz-TDS-Messungen zeigen kein unerwartetes Verhalten in ihrer Temperaturabhängigkeit, was für die Vergleichbarkeit der Proben mit anderen in der Literatur gemessenen Proben spricht. Alle untersuchten Proben zeigen THG, was einen rein auf der quantenkritischen Natur von $CaRuO_3$ basierenden Prozess unwahrscheinlich macht. Darüber hinaus stimmt die Temperaturabhängigkeit in den vier untersuchten Proben mit derjenigen überein, die zuvor für $CaRuO_3$ beobachtet wurde, was zur kohärenten Bildung schwerer Quasiteilchen passt. Die Fluenzabhängigkeit verordnet jedoch die THG in allen Proben in einem nicht-perturbativen Bereich. Diese Fluenzeabhängigkeit entspricht derselben, die für Materialien mit linearer Dispersion beobachtet werden. Es ist bekannt, dass lineare Dispersion die Tieftemperatur-Leitungseigenschaften von $SrRuO_3$ stark beeinflusst, und es wird vorhergesagt, dass dies auch für $CaRuO_3$ gilt. Ob kohärente schwere Quasiteilchen oder lineare Dispersion, unsere Messungen deuten auf einen gemeinsamen Ursprung hin, der auf den Transporteigenschaften von (Sr,Ca)RuO_3 im Grundzustand beruht.

Der Zweibandsupraleiter MgB_2, der BCS-Supraleiter mit dem höchsten T_c bei Umgebungsdruck, eignet sich gut als Material zur Untersuchung von Phänomenen, die aus dem supraleitenden Grundzustand entstehen. Eines dieser Phänomene ist die Higgs-Mode, eine Oszillation der Amplitude der kollektiven supraleitenden Wellenfunktion, deren Existenz als Folge des BCS-Grundzustands vorhergesagt wird. THG hat sich als gute Messmethode für die Higgs-Mode in MgB_2 erwiesen und ermöglicht die Untersuchung des BCS-Zustands ohne Kontakt und auf ultraschnellen Zeitskalen. Dies dient als Grundlage in dieser Arbeit, um das Wissen über die Erzeugung höherer Harmonischer und das Verhalten in einem angelegten Magnetfeld zu erweitern. MgB_2 zeigt eine Erzeugung der fünften Harmonischen im supraleitenden Zustand, die mit der für die THG beobachteten Resonanzbedingung übereinstimmt und mit dem energetisch niedrigeren Energieband in MgB_2 verbunden ist. Darüber hinaus bestärkt eine Pseudospin-Analyse die

Gültigkeit dieser Interpretation. Die Messungen der THG in einem angelegten Magnetfeld verdeutlichen die Verbindung zum supraleitenden Grundzustand. Bei einem zunehmenden angelegten Feld wird das Einsetzen der THG bei niedrigeren Temperaturen beobachtet, die mit dem gemessenen Phasendiagramm für MgB_2 übereinstimmen. Darüber hinaus wird THG zu Beginn der Bildung des supraleitenden Zustands beobachtet, bevor der Zustand der Null-Leitfähigkeit erreicht ist, was die Vielseitigkeit dieses Ansatzes zur Untersuchung von Supraleitern zeigt.

Als Ferrimagnet beherbergt $(Gd,Bi)_3Fe_5O_{12}$ (GdBIG) eine hochfrequente Austauschmode im THz-Bereich in Kombination mit einer endlichen Magnetisierung, was die Untersuchung der Magnetisierungsdynamik vereinfacht. Da es sich um eine einkristalline Probe mit einer Dicke von einigen hundert Mikrometern handelt, was der Wellenlänge von THz-Strahlung entspricht, können physikalische Effekte, die in Resonatoren auftreten, die Dynamik nach einer THz-Anregung stark beeinflussen. TPOP-Messungen mit einer optischen Abfrage, die die THz-induzierte Polarisationsrotation misst, zeigen zwei Phänomene. Erstens zeigt die Magnetisierungsdynamik mehrere Moden, die keine Eigenmoden des Spinsystems sind, sondern Eigenmoden des durch die Probengrenzflächen geschaffenen Resonators. Die diese Moden zwingen die Magnetisierung von GdBIG, ihr zu folgen, was den Nachweis mit einer externen Abfrage ermöglicht. Zweitens wird beobachtet, dass die Austauschmode von hochgradig veränderbarer Natur ist und ihre Amplitude mit der Temperatur oszilliert. Der Anregungsmechanismus wird anhand von polarisations- und fluenzabhängigen Messungen auf das Zeeman-Drehmoment zurückgeführt, wobei sich die Anregung als linear und richtungsabhängig vom Magnetfeld des THz-Pulses erweist. Darüber hinaus zeigt eine numerische Simulation der Austauschmode unter Verwendung gekoppelter Landau - Lifshitz - Gilbert - Gleichungen, dass die Temperaturoszillation der Austauschmode ein Produkt der Überlappung mit den Eigenmoden des Resonators ist. Diese Messungen zeigen, dass durch eine sorgfältige Auswahl der Eigenschaften einer Probe diese Eigenschaften kombiniert werden können, um die resultierende Reaktion zu verstärken.

Acknowledgements

As the famous song from Gerry & the Pacemakers goes: "When you walk through a storm, hold your head up high, and don't be afraid of the dark. At the end of a storm, there's a golden sky, and a sweet silver song of a lark. [...] Walk on! With hope in your heart, and you'll never walk alone...". I would not be at the point of handing in my thesis without the help of the many people I met and walked with on this path.

First of all, I would like to thank Prof. Dr. Ir. Paul van Loosdrecht for giving me the opportunity to do a PhD. I still remember the morning after the defense of my bachelor thesis, we met by chance in a park and you asked me if I was considering doing a PhD. Now, seven years later, I am handing in my thesis because you believed that I am capable of achieving this goal. You pushed me to continuously improve myself, and I can say I will never forget the time I had in Cologne.

I would like to thank Prof. Dr. Steven Johnson for agreeing to be part of the examination committee and for taking the time to be the second examiner of my thesis. Furthermore, I would like to thank Prof. Dr. Simon Trebst for agreeing to be the head of the examination committee. The last exam I had with you was an oral one in "Klassische theoretische Physik II" at the end of my bachelor. After I passed, you asked me: "You have already been here for some time, you probably should be done soon"? I can finally say: "I am done now"!

During my PhD, I had the privilege of working with two direct supervisors: Prof. Dr. Zhe Wang and Dr. Evgeny Mashkovich. Zhe, you already joined our group in the middle of my master thesis and took me to my first beamtime. You helped to lay the foundation of the scientist I am today, thank

you. Evgeny, after Zhe left, you joined and took over as my supervisor. You brought new topics, ideas, and collaborations that helped me to finish my thesis. Even though we sometimes have quite different ways of approaching a topic, these paths corroborated well and we were a good team for the last few years. Thank you for reading my thesis and thank you for everything that you taught me.

I would like to thank my PhD laboratory colleague Semyon Germanskiy. Your drive to continuously improve our experimental setup and knowledge about optics was extremely helpful on the path towards my PhD. Furthermore, I would like to thank our technician Jens Koch for helping with all the little (or big) problems that occurred in the laboratory and during the move.

I would like to thank the senior scientific and administrative staff of the van Loosdrecht group that helped with the multitude of tasks that have to be done on a week-by-week basis. Just to name a few current and former members: Dr. Thomas Koethe, Dr. Ionela Lindfors-Vrejoiu, Dr. Tianyi Wang, Claudia Hazel, Caroline Jentsch, and Britta Schulz, thank you all.

I would like to thank the other PhD students I had the pleasure to work with during my PhD: Jörg, Philipp, Anuja, and Lena, thanks. Robin and Lukas, you two have become quite good friends over the last years and made the last year of my PhD more fun than a last year should be. Thanks to you, I will never be able to move furniture without hearing Frenchcore in the back of my mind.

Lastly, I would like to thank my friends and family. Mama, Papa, Simone und Tobias, als Familie waren wir füreinander da, in guten wie in schlechten Zeiten. Nicht jeder hat das Glück, eine Familie zu haben, die einen unterstützt, und dafür bin ich dankbar.

Sarah, ich werde das Lernen für Mathe 1 in meiner kleinen 12qm-Wohnung nie vergessen, als erste Prüfung, die wir gemeinsam gemeistert haben. Jetzt habe ich auch das letzte Stück des Studiums hinter mir. Auch wenn es manchmal schwierig war, hast du mich die ganze Zeit begleitet.

Tobi, es gibt einen Grund, warum Google denkt, wir wären die gleiche Person. Nicht viele Menschen haben das Glück, über Jahre mit einem ihrer

besten Freunde zusammenzuarbeiten. Das letzte Jahr an der Universität ohne dich war geprägt von einem Mangel an Pizza.

Chris, Lars, Lara, Max und alle anderen, die ich in meiner Zeit in Köln kennengelernt habe, jeder hat auf seine eigene Art und Weise geholfen. Vielen Dank an jeden Einzelnen von euch.

List of Publications

- **C. Reinhoffer**, Y. Mukai, S. Germanskiy, A. Bliesener, G. Lippertz, A. Uday, A. A. Taskin, Y. Ando, Z. Wang, and P. H. M. van Loosdrecht, "Relaxation dynamics of the optically driven nonequilibrium states in the electron- and hole-doped topological-insulator materials $(Bi_{1-x}Sb_x)_2Te_3$", *Physical Review Materials* **4** (12), 124201 (2020)

- S. Kovalev, T. Dong, L.-Y. Shi, **C. Reinhoffer**, T.-Q. Xu, H.-Z. Wang, Y. Wang, Z.-Z. Gan, S. Germanskiy, J.-C. Deinert, I. Ilyakov, P. H. M. van Loosdrecht, D. Wu, N.-L. Wang, J. Demsar, and Z. Wang, "Band-selective third-harmonic generation in superconducting MgB_2: Possible evidence for the Higgs amplitude mode in the dirty limit", *Physical Review B* **104** (14), L140505 (2021)

- S. Germanskiy, R. M. A. Dantas, S. Kovalev, **C. Reinhoffer**, E. A. Mashkovich, P. H. M. van Loosdrecht, Y. Yang, F. Xiu, P. Surówka, R. Moessner, T. Oka, and Z. Wang, "Ellipticity control of terahertz high-harmonic generation in a Dirac semimetal", *Physical Review B* **106** (8) L081127 (2022)

- **C. Reinhoffer**, P. Pilch, A. Reinold, P. Derendorf, S. Kovalev, J.-C. Deinert, I. Ilyakov, A. Ponomaryov, M. Chen, T.-Q. Xu, Y. Wang, Z.-Z. Gan, D.-S. Wu, J.-L. Luo, S. Germanskiy, E. A. Mashkovich, P. H. M. van Loosdrecht, I. M. Eremin, and Z. Wang, "High-order nonlinear terahertz probing of the two-band superconductor MgB_2: Third- and fifth-order harmonic generation", *Physical Review B* **106** (21), 214514 (2022)

- **C. Reinhoffer**, S. Esser, S. Esser, E. A. Mashkovich, S. Germanskiy, P. Gegenwart, F. Anders, P. H. M. van Loosdrecht, and Z. Wang, "Strong terahertz third-harmonic generation by kinetic heavy quasiparticles in $CaRuO_3$", *Physical Review Letters* **132** (19), 196501 (2024)

- T. W. J. Metzger, K. A Grishunin, **C. Reinhoffer**, R. M. Dubrovin, A. Arshad, I. Ilyakov, T. V. A. G. de Oliveira, A. Ponomaryov, J.-C. Deinert, S. Kovalev, R. V. Pisarev, M. I. Katsnelson, B. A. Ivanov, P. H. M. van Loosdrecht, A. V. Kimel, and E. A. Mashkovich, "Impulsive Fermi magnon-phonon resonance in antiferromagnetic CoF_2", *Nature Communications* **15** 5472 (2024)

- **C. Reinhoffer**, I. Razdolski, P. Stein, S. Germanskiy, A. Stupakiewicz, P.H.M. van Loosdrecht, and E. A. Mashkovich, "THz Control of Exchange Mode in a Ferrimagnetic Cavity" unpublished (2024)

Data Availability

The data and the code for simulations are published with Zenodo and can be found under:

- Reinhoffer, C. (2024). Datasets and simulation programs for the thesis 'Terahertz-Induced Dynamics in Strongly Correlated and Magnetic Materials' [Data set]. Zenodo. https://doi.org/10.5281/zenodo.12545652

Erklärung zur Dissertation

Hiermit versichere ich an Eides statt, dass ich die vorliegende Dissertation selbstständig und ohne die Benutzung anderer als der angegebenen Hilfsmittel und Literatur angefertigt habe. Alle Stellen, die wörtlich oder sinngemäß aus veröffentlichten und nicht veröffentlichten Werken dem Wortlaut oder dem Sinn nach entnommen wurden, sind als solche kenntlich gemacht. Ich versichere an Eides statt, dass diese Dissertation noch keiner anderen Fakultät oder Universität zur Prüfung vorgelegen hat; dass sie - abgesehen von unten angegebenen Teilpublikationen und eingebundenen Artikeln und Manuskripten - noch nicht veröffentlicht worden ist sowie, dass ich eine Veröffentlichung der Dissertation vor Abschluss der Promotion nicht ohne Genehmigung des Promotionsausschusses vornehmen werde. Die Bestimmungen dieser Ordnung sind mir bekannt. Darüber hinaus erkläre ich hiermit, dass ich die Ordnung zur Sicherung guter wissenschaftlicher Praxis und zum Umgang mit wissenschaftlichem Fehlverhalten der Universität zu Köln gelesen und sie bei der Durchführung der Dissertation zugrundeliegenden Arbeiten und der schriftlich verfassten Dissertation beachtet habe und verpflichte mich hiermit, die dort genannten Vorgaben bei allen wissenschaftlichen Tätigkeiten zu beachten und umzusetzen. Ich versichere, dass die eingereichte elektronische Fassung der eingereichten Druckfassung vollständig entspricht.

Teilpublikationen:

- **C. Reinhoffer**, P. Pilch, A. Reinold, P. Derendorf, S. Kovalev, J.-C. Deinert, I. Ilyakov, A. Ponomaryov, M. Chen, T.-Q. Xu, Y. Wang, Z.-Z. Gan, D.-S. Wu, J.-L. Luo, S. Germanskiy, E. A. Mashkovich, P. H. M. van Loosdrecht, I. M. Eremin, Z. Wang, "High-order nonlinear terahertz probing of the two-band superconductor MgB_2: Third- and fifth-order harmonic generation", *Physical Review B* **106** (21), 214514 (2022)

- **C. Reinhoffer**, S. Esser, S. Esser, E. A. Mashkovich, S. Germanskiy, P. Gegenwart, F. Anders, P. H. M. van Loosdrecht, Z. Wang, "Strong terahertz third-harmonic generation by kinetic heavy quasiparticles in $CaRuO_3$", *Physical Review Letters* **132** (12), 196501 (2024)

Nicht Peer-Reviewed:

- **C. Reinhoffer**, I. Razdolski, P. Stein, S. Germanskiy, A. Stupakiewicz, P.H.M. van Loosdrecht, and E. A. Mashkovich, "THz Control of Exchange Mode in a Ferrimagnetic Cavity" unpublished (2024)

23.08.2024, Chris Niels Reinhoffer